

Resonant Grating Surfaces for Biosensing

Graham Jack Triggs

Doctor of Philosophy

University of York

Physics

May 2016

Abstract

Optical biosensors make up a valuable toolkit for label-free biosensing. This thesis presents a detailed study on resonant grating surfaces for biosensing. The focus is on silicon nitride gratings, which exhibit a guided-mode resonance that is highly sensitive to refractive index variations in the vicinity of the grating. A sensitivity of 143 nm/RIU (refractive index units) is measured, leading to a detection limit of 2.4×10^{-4} RIU. This performance is shown to be sufficient for the detection of biomolecular binding down to ng/mL concentrations.

With out-of-plane excitation, these gratings can be used as a sensing surface, enabling a spatially-resolved measurement of variations in refractive index; resonance imaging. The minimum detection distance (sensing depth) is measured to be 183 nm away from the grating, while the spatial resolution of resonance imaging is found to be asymmetric: 2 μm parallel to, or 6 μm perpendicular to the gratings. Using a novel approach of fabricating a resolution test pattern on top of the grating, the relationship between resolution and index contrast is studied - an important question in the context of biosensing - where it is found to decrease with index contrast. All experimental results are supplemented with theoretical and computational models.

The resonant gratings are then extensively applied to the study of biofilm development, cellular imaging, and the imaging of cellular secretion. Finally, a miniaturised biosensor is demonstrated, based on a chirped resonant grating. By tuning the resonance wavelength spatially on the chip, the resonance information is directly translated into spatial information. Instrument read-out requires just a monochromatic light source and a simple CCD camera, resulting in a final device that is inexpensive, compact, robust and can be remotely operated. Performance is proven with successful detection of biomolecular binding.

Contents

Abstract	3
Contents	5
List of Figures	9
Acknowledgements	11
Author's Declaration	12
1 Introduction	15
1.1 Background & motivation	15
1.2 State of the art: resonant gratings for biosensing	18
1.3 Scope of this thesis	20
2 Theory of resonant gratings	23
2.1 The nature of light	23
2.2 Light in periodic structures	25
2.3 Guided-mode resonances	28
2.4 Resonance dependence on grating parameters	31
2.5 Angular dependence and band structure	33
2.6 Cavity-based resonance	35
2.7 Summary	36
3 Fabrication details & experimental methods	39
3.1 Introduction	39
3.2 Fabrication details	40
3.2.1 Choice of materials	40
3.2.2 Structure design	41
3.2.2.1 Rigorous coupled-wave analysis	41
3.2.2.2 Particle swarm optimisation	42
3.2.3 Device fabrication	43
3.2.3.1 Substrate preparation (step 1)	43
3.2.3.2 Spin-coating of electron beam resist (step 2)	44
3.2.3.3 Deposition of charge dissipation layer (step 3)	44
3.2.3.4 Electron beam lithography (steps 4 & 5)	44
3.2.3.5 Pattern transfer using reactive ion etching (RIE) (step 6) .	46
3.2.3.6 Final cleaning (step 7)	48
3.2.4 SEM analysis	48

3.3	Experimental methods	48
3.3.1	Measurement setups	49
3.3.2	Tuneable illumination	51
3.3.2.1	Rotating bandpass filter	51
3.3.2.2	Blazed grating filter	52
3.3.3	Microfluidics	53
3.3.3.1	Flow channel	54
3.3.4	Summary	54
4	Sensing	57
4.1	Introduction	57
4.2	Resonance characterisation	57
4.3	Sensitivity measurements	59
4.4	Limit of detection	61
4.5	Sensor functionalisation	63
4.5.1	EDC-NHS protocol	63
4.6	Demonstration of binding of IgG	65
4.7	Summary	67
5	Imaging	69
5.1	Introduction	69
5.2	Penetration depth	71
5.2.1	Measurement idea	72
5.2.2	Results	73
5.2.3	RCWA model of sensing depth	74
5.3	Spatial resolution in X and Y directions	76
5.3.1	Fabricating the resolution test patterns	77
5.3.2	Influence of resist on resonance wavelength	79
5.3.3	Results: spatial resolution in X and Y directions	80
5.3.4	Discussion on spatial resolution	81
5.3.5	Extension to a 2D grating	82
5.4	Dependence of spatial resolution on index contrast	84
5.4.1	Results: simple slab of resist	84
5.4.2	Results: ruler resist pattern	87
5.4.3	FDTD Simulations	88
5.5	Summary and discussion	90
6	Biosensing results	93
6.1	Introduction	93
6.2	Analysis of biofilm formation	93
6.2.1	Motivation	93
6.2.2	Results	94
6.3	Considerations for cell culture	96
6.3.1	Incubation	97
6.3.2	SEM analysis of cells cultured on a resonant grating	98
6.4	<i>In-vitro</i> cellular imaging	98
6.4.1	Extracting spectral information	100
6.4.2	Cell detachment	101

6.5	Imaging cellular secretion	102
6.5.1	Motivation	102
6.5.2	Control experiments	103
6.5.2.1	Control experiment 1	104
6.5.2.2	Control experiment 2	105
6.5.3	Main results: cellular secretion	107
6.5.4	Discussion	107
6.6	Summary	109
7	The chirped grating biosensor	111
7.1	Introduction	111
7.2	Design and fabrication details	112
7.2.1	Comparison and limits of tuning methods	114
7.2.2	The completed sensor	117
7.3	Sensitivity measurement using glucose solutions	118
7.4	Demonstration of IgG binding	119
7.5	Potential for video-rate resonance imaging	120
7.6	Summary	123
8	Conclusions & outlook	125
	Bibliography	129

List of Figures

1.1	Some optical biosensor technologies	16
1.2	Measurement of a resonance map	17
2.1	Illustrations of a 1-dimensional photonic crystal and a grating	26
2.2	Illustration of the grating structure considered in this thesis	27
2.3	RCWA simulation of a typical guided-mode resonance	29
2.4	Reflectance versus wavelength and grating thickness	30
2.5	Reflectance plots showing wavelength versus period, FF, thickness and n_L .	32
2.6	Illustration of the band structure of a 1D photonic crystal	34
2.7	Simulated band diagram of a GMR grating	35
2.8	Demonstration of a cavity-based photonic crystal resonance	36
2.9	Simulation and measurement of a cavity-based resonance	37
3.1	Geometry used in RCWA modelling	42
3.2	Demonstration of the PSO algorithm	43
3.3	Fabrication flow diagram	43
3.4	Diagram and photograph of the RIE system	46
3.5	SEM images of gratings	48
3.6	Diagrams of measurement setups	49
3.7	Diagram of the tuneable monochromator	52
3.8	Monochromator characterisation	53
3.9	Output spectra and measurement of a narrow GMR using different tuneable sources	54
3.10	Table and photograph showing details of the flow channel design	55
4.1	Reflectance spectra of guided-mode resonances	58
4.2	Electric field profiles of TE and TM resonances	59
4.3	Resonance wavelength shift for different glucose solutions	60
4.4	Table of sensitivities found in the literature	61
4.5	Measurement of noise in resonance wavelength	62
4.6	Flow diagram of EDC - sulfo-NHS functionalisation	64
4.7	IgG binding assay	67
5.1	Measurement of a resonance map	70
5.2	Resonance wavelength maps of constant and varied grating surfaces	71
5.3	Concept of the penetration depth measurement	72
5.4	Penetration depth measurement results	73
5.5	RCWA simulations of penetration depth, and corresponding measurements	75
5.6	Fabrication flow-diagram for resolution test patterns	77
5.7	Illustrations of the resolution test pattern	78

5.8	SEM images of the resolution test pattern	78
5.9	AFM images of the resolution test pattern	79
5.10	Spectra and resonance maps of a block of resist	80
5.11	Resonance map of the resolution test pattern	80
5.12	Profiles extracted from resonance maps of the resolution test pattern	81
5.13	Illustration of in-plane mode propagation in 1D and 2D gratings	82
5.14	SEM image and resolution results for a 2D grating	83
5.15	Profiles across a block of resist at different refractive index contrasts	85
5.16	Resonance maps and extracted spectra from the resolution test pattern at different index contrasts	87
5.17	Resonance wavelength, FWHM, and spatial resolution versus n_L and Δn . .	88
5.18	Illustration and results of FDTD simulations of a resist block on a grating .	89
5.19	Results from the FDTD simulations showing spatial resolution	90
6.1	Resonance maps showing biofilm growth	95
6.2	Resonance maps showing biofilm growth	95
6.3	Fluorescence microscope image of a biofilm, and resonance wavelength shift	96
6.4	Illustration of the cell incubation stage	97
6.5	SEM images of neuroblastoma cells cultured on a grating	99
6.6	Resonance map and brightfield image of cells cultured on a grating	100
6.7	Resonance maps and histograms of a cell on a resonant grating	101
6.8	Resonance maps and brightfield images showing cell detachment	102
6.9	Resonance wavelength shift during IgG assay using cell supernatant	105
6.10	Resonance imaging assay of IgG binding	106
6.11	Resonance imaging assay of cellular secretion	108
7.1	Simulation and measurement of resonance wavelength versus grating FF and dose, with illustration of the chirped grating idea	113
7.2	Illustration of the chirped grating operation, and a resonance map	114
7.3	Comparison between different resonance tuning methods	115
7.4	Comparison between tuning capabilities	116
7.5	Illustrations of the chirped grating biosensor	117
7.6	Sensitivity measurements using glucose solutions	118
7.7	IgG binding assay	121
7.8	Arrayed chirped grating for high-speed resonance imaging	121
7.9	Simulations of mirror-bounded grating designs	122

Acknowledgements

I would like to express my deepest gratitude to all those without whom this thesis would have been impossible.

Firstly, I wish to thank my supervisor, Prof. Thomas Krauss, for his unending support, advice and encouragement throughout my research. I am privileged to have had the opportunity to work in his research group and to have had him devote so much time to my progress. I also extend my thanks to my second supervisor, Dr. Gareth Evans, for his continual help and direction on the biological aspects of my research, and to Prof. Nigel Woolsey for his kind support throughout my time at York.

Additionally, I wish to thank my colleagues in the Photonics Group at the University of York for sharing their knowledge and experience during my work, and who have all become close friends. In particular, my appreciation goes to Daan Stellinga, José (Pepe) Juan Colás, Amna Safdar, Donato Conteduca, Giampaolo Pitruzzello, Davide Zecca, Lewis Reeves, Dr. Annett Fischer, Dr. Christian Schuster, Dr. Mark Scullion, Dr Yue Wang, and Dr. Christopher Reardon. Special thanks goes to Dr. Matthias Fischer for his fantastic help with fabrication and when carrying out experiments.

Lastly, I would like to thank my parents, Jack and Brenda, my brother, Malcolm, and Sophie, for their endless support and belief in me.

Author's Declaration

I, Graham J. TRIGGS, declare that this thesis titled, 'Resonant Grating Surfaces for Biosensing' and the work presented in it are my own. I confirm that:

- This work was done wholly or mainly while in candidature for a research degree at this University.
- Where any part of this thesis has previously been submitted for a degree or any other qualification at this University or any other institution, this has been clearly stated.
- Where I have consulted the published work of others, this is always clearly attributed.
- Where I have quoted from the work of others, the source is always given. With the exception of such quotations, this thesis is entirely my own work.
- I have acknowledged all main sources of help.
- Where the thesis is based on work done by myself jointly with others, I have made clear exactly what was done by others and what I have contributed myself.

The following list provides details of publications that have had contributions from the work undertaken for this thesis:

Journal articles

- **Triggs, G. J.**, Fischer, M., Stellinga, D., Scullion, M. G., Evans, G. J. O. & Krauss, T. F. Spatial resolution and refractive index contrast of resonant photonic crystal surfaces for biosensing. *IEEE Photonics Journal*, 7(3), 1–10 (2015).
- Fischer, M., **Triggs, G. J.** & Krauss, T. F. Optical sensors for sensing microbial life on a surface. *Applied and Environmental Microbiology*, doi:10.1128/AEM.03001-15 (2015).
- Aranha dos Santos, V., Schmetterer, L., **Triggs, G. J.**, Leitgeb, R., Gröschl, M., Messner, A., Schmidl, D., Garhofer, G., Aschinger, G., & Werkmeister, R. Super-resolved thickness maps using optical coherence tomography. *Biomedical Optics Express* (accepted 11th May 2016)

- Li, K., Li, J., Reardon, C., Schuster, C. S., Wang, Y., **Triggs, G. J.**, Damnik, N., Muenchenberger, J., Wang, X., Martins, E. R. & Krauss, T. F. Speeding up e-beam lithography for large area photonic nanostructures. *Optics Express* (under review as of 18th May 2016)

Conference attendance

- **Triggs, G. J.**, Fischer, M., Evans, G. J. O., Krauss, T. F. Resonant grating surfaces for biosensing (poster presentation). Photonic and Electromagnetic Crystal Structures (PECS XI), Fudan, China, April 2014.
- **Triggs, G. J.**, Fischer, M., Evans, G. J. O., Krauss, T. F. Resonant photonic crystal surfaces for biosensing (poster presentation). Biophotonics 2015 Summer School, Island of Ven, Sweden, June 2015.

To Sophie

Chapter 1

Introduction

1.1 Background & motivation

Biosensors are devices that enable the detection of biological substances. Usually, the objective is to determine the presence or concentration of a specific molecule that is biologically relevant. A familiar example is the measurement of the concentration of glucose in blood, a procedure carried out daily by millions of people who suffer from diabetes. Blood sugar sensors perform a measurement of electrical resistance to determine the levels of glucose in the blood, but there is a rich variety of other methods by which the presence of a biomolecule may be transduced into a measurable signal. A biochemical sensor, for example, may rely on a chemical reaction between a biomolecule and a suitable substrate molecule that results in a colour change. This is the basis of the ELISA (enzyme-linked immunosorbent assay), a prominent biomedical diagnostic tool used to detect the presence of a specific molecule in a biological or medical sample. Biosensors that employ an optical measurement make up a powerful and diverse range of devices. Some of the most widely used optical detection methods are fluorescence-based. By attaching a fluorophore either directly, or to an antibody that is specific to a biomolecule of interest, its presence can be quantified from the fluorescence emission. This emission can be used for imaging, also allowing specific molecules to be located within living cells. As such, fluorescence microscopy and related techniques, such as multiphoton excitation, fluorescence lifetime imaging, and more, have revolutionised microscopy in the life sciences. In contrast to fluorescence-based methods, label-free optical biosensors rely on a direct interaction between light and the biological material of interest, which typically has a higher refractive index than the surrounding medium. A photonic resonance is often at the heart of these devices, and they are thus commonly referred to as evanescent-field sensors. This resonance gives rise to strong evanescent (decaying) electric fields that penetrate into the sensing region. With appropriate modification of the sensor surface, using antibodies for example, the sensor can be made specific to a target biomolecule. The increased refractive index associated with biological material binding to the device is probed by the evanescent field, resulting in a shift

in resonance wavelength or an intensity change that can be measured with conventional optical equipment. As the evanescent field directly probes the bound biological material, these sensors do not require any form of fluorescent tag or reporter gene. This is highly desirable as it leaves the biomolecules in a natural state without potentially altering their function.

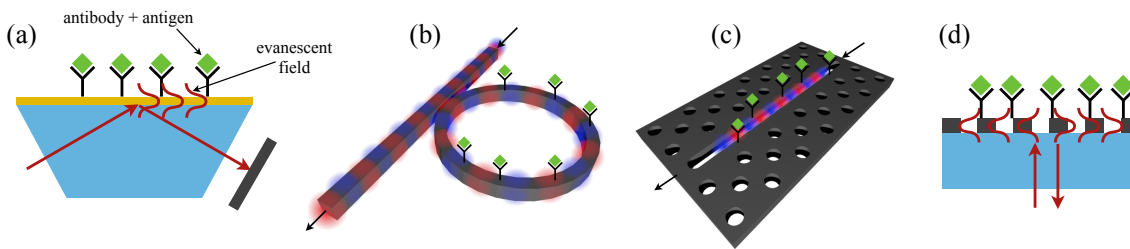


FIGURE 1.1: Some optical biosensor technologies: (a) Surface plasmon resonance; (b) Microring resonator; (c) Slotted photonic crystal cavity; (d) Resonant grating.

An example of an evanescent-field optical biosensor is the surface plasmon resonance (SPR) biosensor, which has seen considerable success, both in research [1], and commercially with the well-known Biacore[™] system [2]. In SPR (figure 1.1(a)), a surface plasmon polariton wave is excited at a dielectric-metal interface for a particular incidence angle. This leads to a sharp dip in reflectance at this angle, and the binding of biomolecules to the interface alters the refractive index experienced by the plasmon, resulting in a measurable change in resonance angle. The surface plasmon resonance is extremely sensitive to refractive index variations at the surface, and consequently, SPR sensing is capable of very high sensitivities, with detection limits down to the range of 10^{-8} refractive index units (RIU) [3].

With the advent of nanofabrication technology over the past three decades, it has become possible to create bespoke structures on the nanometer scale. Built on a similar scale to the wavelength of light, and being made in a material with a high refractive index such as silicon, photonic nanostructures offer exquisite control over light propagation. This control can be exploited to create structures that are resonant at a specific wavelength, producing the strong evanescent fields needed for biosensing. Microring resonators (figure 1.1(b)) exemplify this control of light propagation to generate a resonance, whereby light travels along a waveguide in close proximity to a second, ring-shaped, waveguide. When the ring circumference corresponds to an integer multiple of the wavelength, coupling to the ring becomes very strong and a sharp dip in transmission occurs. The subsequent binding of biomolecules to the ring causes a small refractive index change that red-shifts the resonance wavelength. Microring resonators have also seen much success in both research and commercial applications [4], with an ability to detect index changes down to order 10^{-7} RIU [3]. Recent progress with microring resonators is revealing the possibility of combined electrical and optical biosensing on the same chip, by utilising the electrical properties of

doped silicon [5]. Another pivotal achievement of nanofabrication has been the evolution of photonic crystal sensors (figure 1.1(c)). By periodically varying the refractive index of a structure, i.e. by etching holes into a high-index slab, the propagation of light can be prevented in certain directions, allowing excellent optical confinement around defects in the crystal, for example [6]. Again, this leads to strong evanescent fields at resonance that are particularly sensitive to refractive index changes.

Gratings, the topic of this thesis, have a periodic variation in refractive index much like a photonic crystal, and they too can be engineered to exhibit resonant behaviour (figure 1.1(d)). Like other resonant devices, the strong evanescent field at resonance penetrates into the surrounding material with the result that the resonance wavelength (or angle) is highly sensitive to small refractive index changes. Thus, directly monitoring the resonance wavelength is a way to detect the small changes in refractive index at the grating caused by molecular binding. A distinguishing feature of gratings, however, is that the resonance can be excited with out-of-plane illumination. This is in contrast to microring resonators and waveguide-based photonic crystals, where light must be input and output in the same plane as the sensor structure. Hence, a resonant grating can easily form a sensing "surface", as part of a very simple optical setup, or even a standard laboratory microscope after minimal modification. The most fruitful advantage of out-of-plane operation is the ability to obtain the resonance information by *imaging* the surface at different wavelengths (see figure 1.2). The result is a highly-sensitive measurement of refractive index that is spatially-resolved, and can thus be used as a contrast mechanism to produce an image, or a refractive index map of the surface, indicating local variations in refractive index due to the presence of cells or molecular binding, for example.

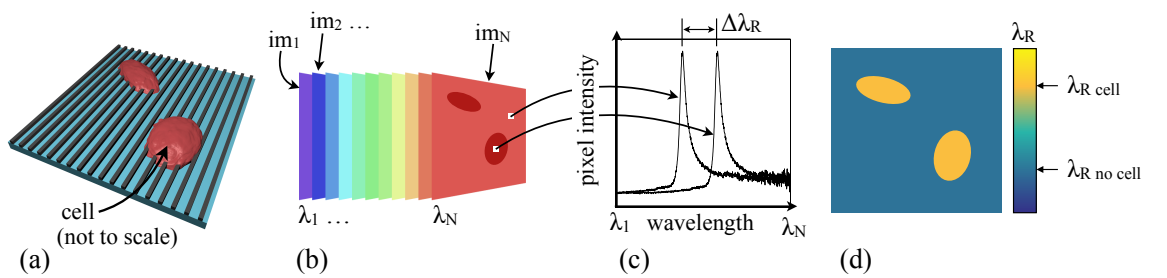


FIGURE 1.2: Measurement of a resonance map. (a) resonant grating with, for example, cells cultured on the surface; (b) brightfield images of the grating are collected as incident wavelength is swept from λ_1 to λ_N ; (c) for each pixel in the field of view, the spectrum may be extracted, and the resonance wavelength at each pixel is used to generate a resonance map (d), where the colour scale indicates the resonance wavelength.

The ability to measure the presence and concentration of a particular biomolecule is of huge importance medically, biologically and environmentally. For example, the glucose sensors mentioned above play a vital role in the health and wellbeing of diabetics, and

many other infections and diseases, such as HIV [7] or cancer [8], can be diagnosed and monitored by measuring relevant biomarkers. The development of drugs can also be aided by monitoring specific biomarkers [9], or by monitoring the response of cells to a particular treatment [10]. This has overlaps with research into tackling antimicrobial resistance (AMR), predicted to be one of the major challenges in 21st century medicine [11], where biosensors may monitor microbe response to antibiotics. Furthermore, on a cellular level, signalling molecules play a role in many fundamental processes in the human body. For example, the levels of neurotransmitter molecules in the brain are associated with stress levels [12], a number of psychiatric disorders such as depression, schizophrenia and ADHD, and they are also related to learning and memory [13]. Measuring such signalling molecules in neuronal cell cultures would further our understanding of the human brain and disorders associated with neurotransmitter deficiencies. In an environmental context, biosensors play a crucial part in the detection of contaminants and pathogens in water sources and food supply infrastructure [14], and in monitoring marine toxins and pollutants [15, 16]. A further application is the detection and monitoring of biofilm growth in aqueous environments [17]. In an industrial setting, biofilms can lead to biofouling and corrosion in many fluidic systems such as heat exchangers or pipelines. Medically, they pose a significant danger, where biofilm growth on implants and catheters can lead to severe bacterial infections [18]. These are just a handful of examples, and over the last ~ 15 years there has been a growing demand to improve and expand biosensor technology, evident from a significant increase in biosensor-related publications; since 2005, the number research articles on the topic of biosensors being published per year has risen from below 2000 to almost 7000 [19]. This research is being driven by motivations depending on the end application of the sensor. For biosensors used in clinical and biological research, the desire is primarily to enhance the sensitivity, resolution and throughput. For the detection of disease in the developing world, for instance, the aim is a low cost, mass-manufacturable sensor that can be used outside a laboratory by non-experts. There has also been a push towards sensor miniaturisation with the "lab-on-a-chip" paradigm [20], and more recently, efforts have been directed towards wearable and smartphone-compatible biosensors [21] that could enable patients to perform their own healthcare diagnostics and monitoring at home. It is estimated that the global market for biosensors will exceed 21 billion US\$ by 2020 [22].

1.2 State of the art: resonant gratings for biosensing

The following section provides a short overview of the main progress within the resonant grating biosensor community. Highly relevant publications are also discussed at depth in specific contexts within each chapter of this thesis.

Resonant gratings were first employed for biosensing in the early 2000s with Lin and Cunningham successfully demonstrating the detection of protein binding with a molecular weight of a few hundred Da [23, 24]. Due to the large sensing areas possible when using a grating, the potential for performing multiple binding assays in parallel was soon identified, with promise in applications such as high-throughput drug screening and proteomics. To this effect, a nanoimprinting process has been employed in order to rapidly fabricate arrays of gratings on an inexpensive plastic substrate that can then be positioned beneath a multi-well plate [25, 26]. Fang et al. have extensively demonstrated in a number of publications the ability of resonant gratings to monitor changes in cell attachment and shape, and relating these to probe cell signalling processes [27]. These reports focus especially on measuring changes in the mass distribution within cells, in real time [28, 29], and this has been related to potential use in drug development [10]. The group of Kristensen have utilised a resonant grating to perform refractometric measurements of the dynamics of sugar dissolution [30], as well as measurements of the absolute refractive index dispersion of liquids [31]. In addition to a direct interrogation of the resonance wavelength (or angle) to monitor biomolecular binding, resonant gratings have also recently been integrated into more complex sensing systems. For example, Ge et al. [32] use a resonant grating as one of the mirrors of an external cavity lasing system, resulting in excellent sensing resolution. The method is further improved by the addition of a reference resonant grating [33], enabling the true signal from biomolecular binding to be better distinguished from thermal fluctuations and noise in the system.

While resonant gratings were originally (and continue to be) employed purely as a sensing tool, where the readout is from the whole sensing area and is not spatially-resolved, they have since seen considerable use as an imaging tool, as illustrated in figure 1.2. This was initially reported in 2004 by Li et al. [34], where resonance maps of the sensor were acquired using an imaging spectrometer and a scanning stage. In 2006, the same group showed that the sensor can be employed to generate a resonance map showing cell attachment across a large area [35]. The idea of monitoring cell attachment has since been at the forefront of grating biosensor development, due to the ability to detect minute changes at the sensor surface. More recently, in the last ~ 5 years, advanced resonance imaging has been demonstrated by the groups of Cunningham, Fang and Gerken with excellent sensitivity and spatial resolution of a few μm , allowing resonance imaging to operate on a single-cell level. These studies have been largely aimed at studying cell attachment [36, 37, 38], as well as cell clustering behaviour [39] and cell topography measurements [40].

Although one of the main advantages of resonant grating sensing is that it is label-free, the concept of combining resonance imaging with fluorescence imaging has also been established [41, 42]. In particular, it is possible to enhance fluorescence excitation by matching

a grating resonance to the fluorophore excitation wavelength, thereby increasing signal-to-noise ratio in fluorescence imaging. Moreover, the grating can be employed to enhance the extraction of fluorescence emission by directing its propagation towards the detection optics [43]. Fluorescence imaging can very practically be carried out simultaneously with resonance imaging, which typically occurs at a longer wavelength than fluorophore excitation and emission. In addition to applications of resonant gratings to biomolecular binding and cell-based assays, there have been efforts to enhance the performance of grating biosensors. Sensitivity increases have been demonstrated by subtly altering the design of the grating [44], or by tailoring the materials used, thereby allowing control over the evanescent field strength. Examples include the use of a porous sublayer below the grating [45], or the formation of nanopillars on the grating surface to increase the surface area to which molecules can bind [46]. I present a brief review of sensitivities reported in the literature in chapter 4 of this thesis. Lastly, the spatial resolution of a grating biosensor in terms of resonance imaging has been investigated by Block et al. [47], and this is built upon extensively in chapter 5. For a in-depth review of recent progress in the field, I refer to Cunningham et al. [48].

1.3 Scope of this thesis

The work presented in this thesis focuses on resonant gratings fabricated in silicon nitride - a highly robust and biocompatible material. The underlying theoretical principles of the resonance mechanism are explored in detail in chapter 2, and a physically intuitive picture will be conveyed through rigorous simulations that show how the resonance depends on various grating parameters such as the period, thickness, and so on. Furthermore, comparisons to photonic crystals are made, including a study of the band structure of the grating, which is rarely seen for these devices in the literature.

A complete description of the fabrication process is then presented in chapter 3, along with details of the experimental setups and bespoke microfluidic channels required for performing the biosensing assays that follow. Prior to applying the sensor to these assays, it is fully characterised in terms of sensing and imaging capabilities in chapters 4 and 5, respectively. In particular, the sensitivity and limit of detection are verified using glucose solutions as refractive index standards. Sensor functionalisation is discussed and followed with an assay to verify the ability to detect molecular binding. The penetration depth, or sensing depth, is also explored in detail with a simple yet accurate experiment that is verified using modelling. A unique measurement in the field, this also leads to a better understanding of the evanescent electric field profiles associated with the grating resonances. Following this, extensive studies on the spatial resolution are presented, where a new approach involves the fabrication of a resolution test pattern on top of the sensor. Not only does this allow the spatial resolution to be determined, but it enables a study into its

dependence on refractive index *contrast*. This is a fundamental question in the context of biosensing, where index contrasts may be very small (for example, between a living cell and the culture medium), yet this had not been addressed before this work. While the exact results presented here are specific to this sensor, the overall findings and trends are generic to most resonant gratings.

Biosensing applications are presented in chapter 6, including detailed examples of cellular imaging *in-vitro*, and a demonstration of the wealth of information that can be extracted from a resonance image, such as changes in cell attachment. The sensor is also employed to investigate biofilm growth over a number of days, revealing information on biofilm density, coverage and growth phases. The biosensing results culminate with experiments to image the cellular secretion and binding of a specific molecule, label-free, *in-vitro*, and in real time. Not yet demonstrated in the field, this exemplifies the full potential of the resonant grating sensor as a combined sensing-imaging tool, and could be of tremendous value to cell biology research.

Lastly, the chirped grating biosensor is presented in chapter 7. For the first time, by applying a grating design inspired by the work of Kunz [49] to a guided-mode resonant grating, the resonance wavelength is varied *spatially* across the chip. In this way, a resonance shift due to biomolecular binding is directly translated into a spatial shift that can be read out using only a monochromatic light source and a simple CCD camera. The resulting sensor can be packaged in a compact, robust format using just two basic optical components, and could be mass-produced for a minimal cost. This novel approach is very promising for medical and environmental sensing at the point-of-care, in the home, or in the field, and it could even be remotely-operated. The performance of the chirped grating sensor is demonstrated with sensitivity measurements and a successful binding assay.

The work presented in this thesis makes several valuable contributions to the field of resonant grating biosensing. In particular, the studies on the dependence of spatial resolution on refractive index contrast are shown for the first time, while the measurement of the sensor penetration depth is a further addition. Resonance imaging is employed for the analysis of biofilm growth, a system that has not yet been studied with this method. Furthermore, to my knowledge, a demonstration of resonance imaging combined with antibody-based detection has not yet been achieved, and this is presented here by the experiments on imaging cellular secretion. This research has also led to the development of a new chirped resonant grating device. With this, the spatial encoding of resonance information has enabled the creation of a very compact, stand-alone sensor that requires only a camera and a monochromatic light source for readout, and it moves resonant gratings closer to becoming a true lab-on-a-chip sensing technology.

Chapter 2

Theory of resonant gratings

This section lays out the theoretical ideas associated with the resonant gratings presented in this thesis. Beginning with a brief overview of Maxwell's equations and a description of light in periodic media, diffraction gratings and guided-mode resonances are then studied in detail. The theoretical concepts are accompanied by graphical plots from simulations where a number of grating parameters are varied, conveying a more intuitive picture of the resonant behaviour. Furthermore, this study is also beneficial in understanding the fabrication tolerance of the resonances. This is followed by a short analysis of the band structure of the resonant grating, giving yet more insight into the grating properties. The chapter is concluded with a brief discussion on a cavity-based resonance mechanism.

2.1 The nature of light

Light is an electromagnetic wave consisting of sinusoidally-varying electric (\mathbf{E}) and magnetic (\mathbf{B}) fields. These fields oscillate perpendicularly to each other, are in phase, and have the same frequency (ν). The direction in which light then propagates through space is perpendicular to both \mathbf{E} and \mathbf{B} , and is described by the orientation of the 'k-vector' (\mathbf{k}), such that \mathbf{E} , \mathbf{B} and \mathbf{k} are all orthogonal for a plane wave. $|\mathbf{k}|$, or the "wavenumber", can be thought of as a spatial angular frequency: $k = 2\pi/\lambda$, where λ is the wavelength, while the temporal angular frequency is $\omega = 2\pi\nu$. The propagation of light in vacuum, where there are no sources or existing electrical charges or currents, is fully described by the four Maxwell equations [50]:

$$\begin{aligned}\nabla \cdot \mathbf{E} &= 0 & \nabla \times \mathbf{E} &= -\frac{\partial \mathbf{B}}{\partial t} \\ \nabla \cdot \mathbf{B} &= 0 & \nabla \times \mathbf{B} &= \mu_0 \epsilon_0 \frac{\partial \mathbf{E}}{\partial t}\end{aligned}$$

These equations form the cornerstone of electromagnetic theory. For the vacuum case, the two divergence equations state that there are no sinks or sources of \mathbf{E} or \mathbf{B} fields,

while the two curl equations indicate that an oscillating electric field induces an oscillating magnetic field, while an oscillating magnetic field induces an oscillating electric field. Due to these mutual field inductions, electromagnetic waves do not require a medium in which to propagate. Maxwell's equations are coupled first-order partial differential equations, but they can be decoupled to yield separate second-order equations for \mathbf{E} and \mathbf{B} [50]:

$$\nabla^2 \mathbf{E} = \mu_0 \varepsilon_0 \frac{\partial^2 \mathbf{E}}{\partial t^2} \qquad \nabla^2 \mathbf{B} = \mu_0 \varepsilon_0 \frac{\partial^2 \mathbf{B}}{\partial t^2} \quad (2.1)$$

These take the form of equations describing a wave that has a propagation velocity of $1/\sqrt{\mu_0 \varepsilon_0}$, where μ_0 and ε_0 are the vacuum permeability and permittivity, respectively. This velocity corresponds to the speed of light in vacuum: $c \approx 3.00 \times 10^8 \text{ ms}^{-1}$. When an electromagnetic wave passes through a dielectric material, the atoms are polarised and magnetised in response to the oscillating \mathbf{E} and \mathbf{B} fields, respectively, and in turn create their own fields. The resulting combination of all fields is a single wave with the same frequency, but a different velocity. The only change required in the Maxwell equations is to replace $\mu_0 \varepsilon_0$ with $\mu \varepsilon$ (permeability and permittivity of the material), in which case, the propagation velocity of the wave is now:

$$\frac{1}{\sqrt{\mu \varepsilon}} = \frac{c}{n}, \text{ where } n = \sqrt{\frac{\mu \varepsilon}{\mu_0 \varepsilon_0}}. \quad (2.2)$$

n is the index of refraction of the material, and it describes how the propagation velocity is reduced compared to the vacuum velocity c . For the majority of dielectric materials, $\mu \approx \mu_0$, so $n = \sqrt{\varepsilon/\varepsilon_0} = \sqrt{\varepsilon_r}$, where ε_r is the dielectric constant or relative permittivity of the material. In this thesis, the materials of concern are assumed to be lossless, non magnetic ($\mu = \mu_0$), non-dispersive (ε_r is not frequency-dependent), and isotropic (ε_r is a scalar and is not direction-dependent). Additionally, the field intensities of interest here are small enough that any non-linear terms in the material polarisability are negligible, and only real, positive values of ε_r are considered (material absorption is commonly accounted for by making the refractive index a complex number, while metamaterials and metals can have negative values of n). I also note that from here on I only refer to the relative permittivity, so the r subscript is dropped for brevity: $\varepsilon_r = \varepsilon$. When the electromagnetic wave encounters an interface with a material of *different* ε , the boundary conditions enforced by Maxwell's equations give rise to Snell's law of refraction and the Fresnel equations, which predict the reflection behaviour of light at a dielectric interface. Furthermore, by exploiting the linearity of the Maxwell equations, the temporal and spatial terms can be separated, where the fields that satisfy the EM wave equations (eqns. 2.1) can be expressed as "harmonic modes": a spatial mode profile multiplied by a complex exponential with angular frequency ω :

$$\mathbf{E}(\mathbf{r}, t) = \mathbf{E}(\mathbf{r})e^{-i\omega t} \qquad \mathbf{B}(\mathbf{r}, t) = \mathbf{B}(\mathbf{r})e^{-i\omega t} \qquad (2.3)$$

The form of the spatial profile $\mathbf{E}(\mathbf{r})$ depends on the spatial distribution of ε and knowledge of this allows the spatial mode profiles to be calculated by treating Maxwell's equations as an eigenvalue problem. With this approach, the resulting mode profiles are the eigenfunctions of the system while the frequencies (ω) of the modes are the corresponding eigenvalues.

2.2 Light in periodic structures

The harmonic solutions to the wave equations in a homogeneous medium are plane waves. However, a special case arises when the spatial distribution of ε is periodic with a period (a) of a comparable size to the wavelength of light in the material. Such materials are known as photonic crystals, and may have a periodic variation of ε in one, two, or three dimensions. The effect of a periodic ε on electromagnetic waves is analogous to the effect of the periodic atomic potential encountered by the wavefunction of the electron in a crystalline lattice. As such, many of the phenomena that arise in electron transport through solids are observed for light transport through photonic crystals. The simplest photonic crystal is a stack of dielectric layers with alternating ε (figure 2.1(a)) - a 1D photonic crystal. The most useful property of such a stack is the ability to reach near 100% reflectance at certain wavelengths due to destructive interference from successive interfaces (the Bragg condition). More commonly known as a distributed Bragg reflector (DBR), these are crucial components in distributed feedback lasers, VCSELS (vertical cavity surface emitting lasers), and more. A diffraction grating is a special case of a 1D photonic crystal, where the dielectric layers have a finite size (usually of a similar size to the period) in one of the dimensions normal to the periodicity, illustrated in figure 2.1(b). This size corresponds to the depth (t) of the grating grooves.

According to Bloch's theorem, when $\varepsilon(\mathbf{r})$ is periodic, the spatial mode profiles $\mathbf{E}(\mathbf{r})$ can be expressed as a plane wave with an amplitude that is modulated by a function ($u_{\mathbf{k}}(\mathbf{r})$) of the same periodicity as $\varepsilon(\mathbf{r})$ [51]:

$$\mathbf{E}_{\mathbf{k}}(\mathbf{r}) = u_{\mathbf{k}}(\mathbf{r})e^{i(\mathbf{k}\cdot\mathbf{r})} \qquad (2.4)$$

These are known as Bloch modes (or states), and are distinguished by their \mathbf{k} -vector, \mathbf{k} . By expressing the periodicity of $\varepsilon(\mathbf{r})$ in terms of a grating vector, $\mathbf{G} = 2\pi/a$, where a is the period, the Bloch modes within the periodic structure take the form:

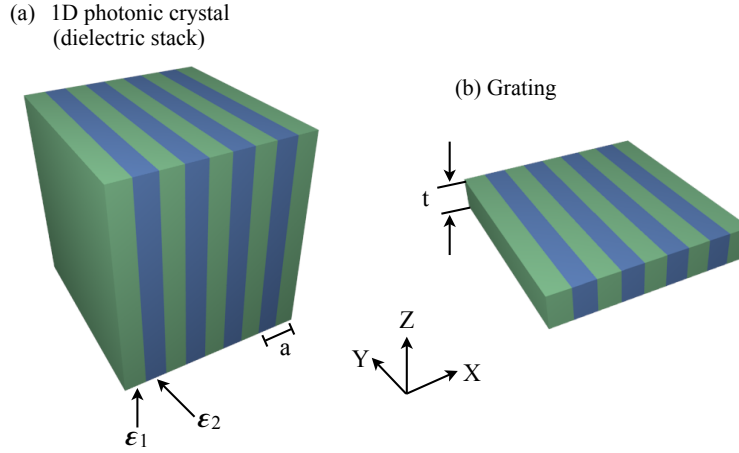


FIGURE 2.1: Illustration of (a) a regular 1-dimensional photonic crystal and (b) a grating. In (a), the crystal extends to infinity in all three dimensions, while for (b) there is a finite thickness in the z-dimension.

$$\mathbf{E}_{\mathbf{k}}(\mathbf{r}) = \sum_{m=-\infty}^{\infty} E_m e^{i(\mathbf{k}+m\mathbf{G})\cdot\mathbf{r}} \quad \text{for } m = \dots, -2, -1, 0, 1, 2, \dots \quad (2.5)$$

In other words, a plane wave can couple to the Bloch modes in the periodic structure by adding or subtracting integer multiples (m) of \mathbf{G} to the incident \mathbf{k} -vector. Physically, this means the incident wave splits into diffraction orders, each having a different \mathbf{k} -vector.

For the gratings discussed in this thesis, I restrict the discussion to one-dimensional periodicity in the x -direction (1D gratings). However, a 2D grating is demonstrated briefly in chapter 5, and its behaviour is discussed within the context of that chapter. Moreover, the following discussions focus on the case where light is incident on the grating from below and the reflectance response is measured, although some results shown later will show the transmittance response. This does not limit the relevance of the next sections to reflectance measurements; since all the materials used are non-absorbing, it is trivial to deduce the transmittance response using $T = 1 - R$, and vice-versa for the reflectance response. Figure 2.2 shows an illustration of the typical grating and denotes all the relevant parameters that are used throughout the thesis.

The field boundary conditions and conservation of momentum dictate the phase-matching condition in the direction of periodicity (the x -direction here):

$$k_{x,m} = k_{x,inc} - mG, \text{ for } m = \dots, -2, -1, 0, 1, 2, \dots, \quad (2.6)$$

where m denotes the diffraction order and G is the grating vector. This relationship (also known as the Floquet condition) describes all permitted harmonics in the grating.

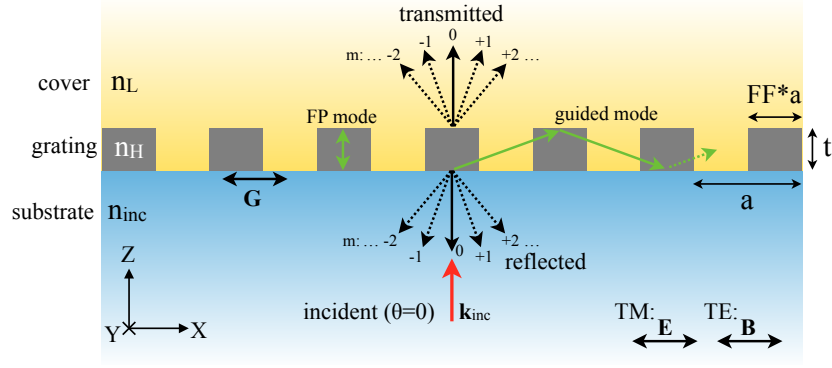


FIGURE 2.2: Illustration of the grating structure considered in this thesis. Light is incident on the grating from below with k -vector k_{inc} , through substrate material of index n_{inc} , at normal incidence ($\theta=0^\circ$). The incidence polarisation states are indicated in the lower right. n_H and n_L denote the ridge and groove refractive indices, respectively, and the cover region is also set to have index n_L . The grating thickness is denoted by t , the period by a , and the fill factor by FF . FF is the portion of a period that is taken up by the high-index material, n_H , such that the ridge width is given by $FF \times a$.

Substituting more general terms for k_x and G results in the familiar grating equation:

$$k_{x,m} = k_{x,inc} - mG \quad (2.7)$$

$$k_0 n_{eff} \sin(\theta_m) = k_0 n_{inc} \sin(\theta_{inc}) - m \frac{2\pi}{a} \quad (2.8)$$

$$n_{eff} \sin(\theta_m) = n_{inc} \sin(\theta_{inc}) - m \frac{\lambda_0}{a} \quad (2.9)$$

Here, n_{inc} is the refractive index in the cover region, θ_{inc} is the incidence angle, and λ_0 the incidence wavelength in vacuum. m denotes the diffraction order, θ_m is the diffraction angle of the m^{th} order (into the grating layer), a is the grating period, and n_{eff} is the *effective* refractive index of the grating layer. The effective refractive index is used to describe the refractive index while taking into account the physical dimensions of the grating and the mode profile, and it is therefore not a constant for a particular grating geometry but is also dependent on the shape of the mode. Due to the periodicity of ε being solely along x (for a 1D grating), different polarisations (directions of \mathbf{E}) experience different refractive indices - in a sense, the grating is birefringent. I define TE polarisation as being that with the \mathbf{E} vector aligned parallel to the grating, while TM has \mathbf{E} aligned with the grating vector \mathbf{G} , i.e. perpendicular to the grating. Approximations for n_{eff} for these two polarisations are found in [52]:

$$n_{eff,TE} = \sqrt{FF n_H^2 + (1 - FF) n_L^2} \quad n_{eff,TM} = \frac{1}{\sqrt{\frac{FF}{n_H^2} + \frac{1-FF}{n_L^2}}} \quad (2.10)$$

These approximations are accurate for the cases where $\lambda \gg a$, since the fine structure of

the grating is not resolved by the wavelength of the light, and the refractive index may be taken as a geometrical average. However, on the scale where $\lambda \sim a$, and especially when $\lambda < a$, these approximations become increasingly incorrect. More accurate expressions are beyond the scope of this thesis, and equations 2.10 are deemed to be sufficient for the discussions and calculations in this work.

2.3 Guided-mode resonances

Resonances in gratings have been known for well over 100 years, since they were first reported by Wood in 1902 [53]. Wood discovered "spectral anomalies" within the diffracted orders of a ruled grating, manifesting as sharp changes in diffracted power for small changes in incidence angle, or equivalently, wavelength. The subsequent study of grating resonances has gathered momentum and there is now a substantial body of literature on both the theoretical understanding and practical uses of such resonances. The gratings reported in this work exhibit guided-mode resonances (GMRs), a specific type of resonance that can occur if the grating layer operates also as a waveguiding layer. At a specific incidence angle or wavelength, a GMR grating can be designed to show complete reflectance or transmittance in a bandwidth typically of order 0.1-5 nm. In theory, the resonance linewidth can be made arbitrarily narrow by reducing the grating refractive index contrast: $n_H - n_L$, and, importantly, the resonance wavelength is highly sensitive to the refractive index surrounding the grating. It is this property of GMRs that is key to their success in biosensing. Figure 2.3 shows an example of the resonance employed in much of this thesis, for two different values of n_L , demonstrating its ability to detect changes in refractive index. These spectra are calculated using rigorous coupled-wave analysis (RCWA), which is discussed in chapter 3, while experimental spectra can be found in chapter 4. It is evident that the shape of this resonance is asymmetric. This arises because the resonance is an interference between two processes: the slowly-varying thin-film response of the grating layer combined with the quickly-varying Bragg resonance of the in-plane guided-modes, as will be discussed next. This physical behaviour is the basis of a Fano lineshape [54], and this concept is discussed further in chapter 4.

The careful design of GMR gratings has also led to a rich variety of other planar optical elements. For example, the narrow reflectance bands are highly useful in the design of filters [55]. Or, by designing the grating such that multiple resonances work in combination, broadband reflectance can be achieved over ranges of 100s of nm [56, 57, 58]. Due to the inherent asymmetry of a 1D grating, it is already polarisation-dependent, making it valuable as a polarising element [59] or a wave plate [60], where the TE and TM responses can be controlled almost independently. All of these optical elements can be made using only dielectric materials resulting in very low losses, and can be made ultrathin.

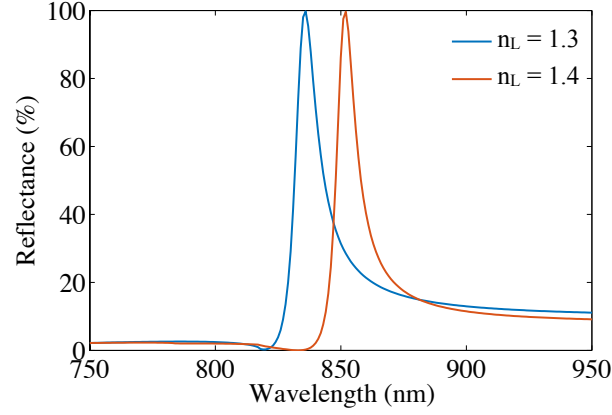


FIGURE 2.3: RCWA simulation of a typical guided-mode resonance for $n_L = 1.3, 1.4$. The grating parameters are: $t = 150$ nm, $a = 560$ nm, $n_{inc} = 1.46$, filling factor (FF) = 0.75, $n_H = 2.00$. Incident polarisation is TE, and is at normal to the grating ($\theta_{inc} = 0$).

The resonant behaviour at the heart of these devices is realised when the grating meets the following criteria:

$$n_{eff} > n_{inc} \qquad \frac{\lambda_0}{n_{eff}} < a < \frac{\lambda_0}{n_{inc}} \qquad (2.11)$$

The first condition states that the effective refractive index of the grating layer be higher than the surrounding indices (for my system, n_{inc} , being a glass substrate, is the highest of the surrounding indices). This ensures that the grating layer can support index-guided modes like a regular waveguide, where the number of waveguide modes it can support is dependent on the thickness (t) of the grating layer and λ . The second condition requires that the grating period (a) is smaller than the wavelength in the incidence medium, but larger than the wavelength in the grating layer. This regime of operation is referred to as the "near-wavelength" regime [61]. It is evident from the grating equation (eqn.2.9) that when this inequality is satisfied, only the 0^{th} order ($m = 0$) exists in the cover and substrate regions, but non-zero orders are allowed to propagate within the grating layer. Now, provided that the grating is thick enough to support a waveguide, the incident light can be diffracted into a guided mode which proceeds to propagate laterally along the grating. However, since the waveguide is periodic and not homogeneous, the guided modes scatter at each grating interface. In the literature, these are referred to as "leaky-modes" by a number of authors [59, 43, 58, 62]. This scattering allows the guided modes to be reflected back on to each other, but also to couple out of the grating. Therefore, depending on the grating thickness, the guided modes can phase-match to the freely-propagating 0^{th} order reflection or transmission. With careful design of the thickness, period, duty cycle, and refractive indices, this phase matching can be tuned to be completely destructive for the transmitted 0^{th} order wave, resulting in a single wavelength having 100% reflectance. At resonance, the guided modes form a standing wave field pattern due to being coherently

reflected from each ridge-groove interface. This enhances the electromagnetic field strength, making the resonance highly sensitive to the refractive index surrounding the grating (n_L) - crucial for its use in biosensing.

The ideal operating regime of a GMR grating is generally limited to the near- λ regime (defined by the second inequality in eqn. 2.11). For instance, if a is small enough to be subwavelength within the grating layer, the non-zero orders (and thus the guided modes) are not excited and the response is conventional thin-film interference of the 0^{th} orders. On the other hand, if a is large enough that it is no longer subwavelength in the incidence medium, GMRs still exist but the non-zero orders are able to carry energy away into different angles (θ_m), which (usually) renders the structure less efficient, less useful, and its optical response substantially more complicated.

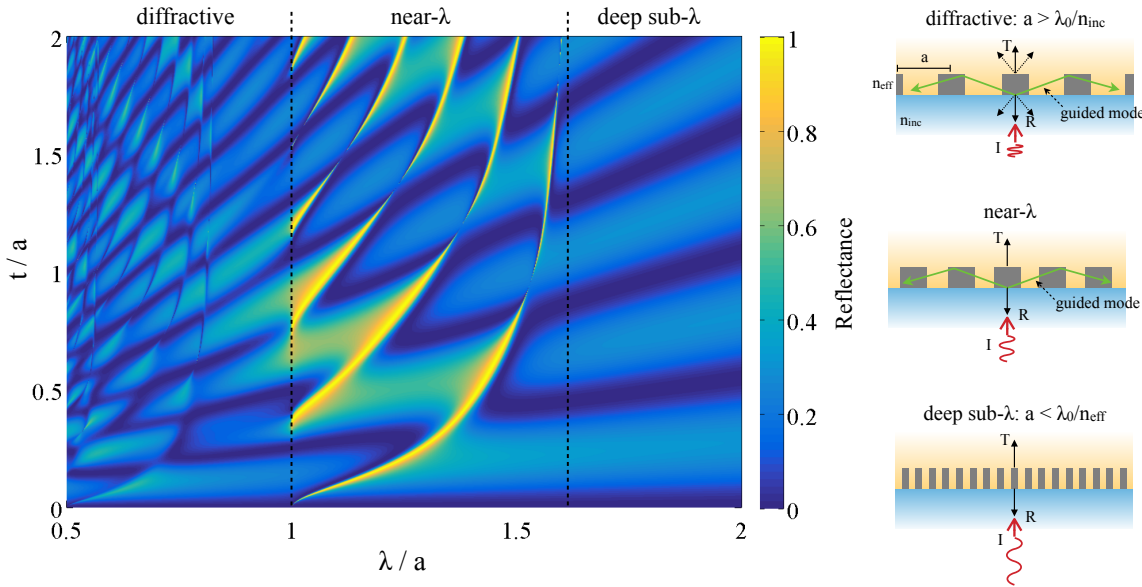


FIGURE 2.4: Reflectance versus wavelength (λ) and grating thickness (t), both normalised by the grating period (a). $FF = 0.75$, $n_H = 2.00$, and the grating is fully surrounded by air ($n_{inc} = n_L = 1.00$). The sub-wavelength and diffractive regions are indicated by the vertical dashed lines, and these are illustrated at the right hand side. Illumination polarisation is TE. (RCWA simulation).

A more physically intuitive picture of the grating behaviour can be seen by plotting the reflectance (or transmittance) against the grating parameters, an approach taken by many other theoretical studies [61, 63, 64, 57]. For example, figure 2.4 shows a surface plot of reflectance versus illumination wavelength (λ) and grating thickness (t) (both normalised to the grating period, a). For simplicity, the grating here is fully surrounded by air ($n_{inc} = n_L = 1.00$). Superimposed on the plot are vertical lines to indicate the various operating regimes, labelled along the top axis. When $\lambda/a < 1$, the grating is diffractive and the non-zero orders carry energy away from the grating into different angles (as per eqn. 2.9). As such, there are no high reflectance areas or resonances (yellow) in the diffractive region.

In contrast, when $\lambda/a > 1$, the grating is said to be "sub-wavelength", and only the 0^{th} orders can propagate away from the grating. However, as emphasised by Chang-Hasnain and Yang [61], the sub-wavelength regime can be further divided into "near-wavelength" and "deep-sub-wavelength" regimes. In the deep-sub-wavelength regime, $a < \lambda_o/n_{eff}$, and the grating structure is significantly smaller than the wavelength of the light and can be treated as a homogeneous slab having n_{eff} . Thus, typical thin-film interference behaviour is observed in the λ - t plot, manifested as a number of simple fringes that increases with thickness and decreases with λ . In the near- λ regime, the second inequality in eqn. 2.11 holds, and the resulting reflectance is a combination of thin-film interference with guided mode excitation, easily visible as the curved yellow lines along which 100% reflectivity can be achieved due to guided-mode resonances. The shape of resonance curves is similar to a tangent function, as expected for waveguide modes [55], where a thicker waveguide is needed to support the mode at a longer wavelength. Similarly, multiple guided modes appear as the grating becomes thicker, or as the wavelength becomes smaller.

2.4 Resonance dependence on grating parameters

Further insight into the resonance behaviour is gained by tracking the resonance wavelength (λ_R) as the grating parameters are changed. Figure 2.5 shows reflectance surface plots, with incidence wavelength along the x-axis versus the grating period, filling factor, thickness, and cover/groove refractive index. As before, these are simulated using RCWA. Superimposed on the plots are dashed white lines to indicate the parameters used for the main grating design in this thesis: $\lambda_R \approx 840$ nm (for $\theta_{inc} = 0^\circ$ and $n_L = 1.333$), $a = 560$ nm, $t = 150$ nm, $n_{inc} = 1.46$, and $n_H = 2.00$.

Looking at these plots in more detail, figure 2.5(a) clearly shows a highly linear dependence of λ_R on period a , as expected from the grating equation where $\lambda(a) \propto a$ for a given order m . The green and red dashed lines indicate where the grating becomes diffractive in the glass substrate and grating layer, respectively. It is clear that the GMR lies within the near-wavelength regime set by the second inequality in eqn. 2.11. In the top left, i.e. at long period and short wavelength, another guided mode resonance exists, however the grating is now diffractive into the substrate so the reflectance and Q-factor of this resonance are significantly reduced, hence the line is weaker.

Figure 2.5(b) shows the dependence on FF, which can be thought of as n_{eff} (eqn. 2.10), where a smaller FF yields a lower n_{eff} . The plot shows that λ_R is largely independent of FF across a large range, suggesting that n_{eff} remains high enough to allow guided modes to exist, and it is mainly the period (which is constant here) that dictates the coupling into a guided mode. The resonance only exists on the right-hand side of the red dashed line,

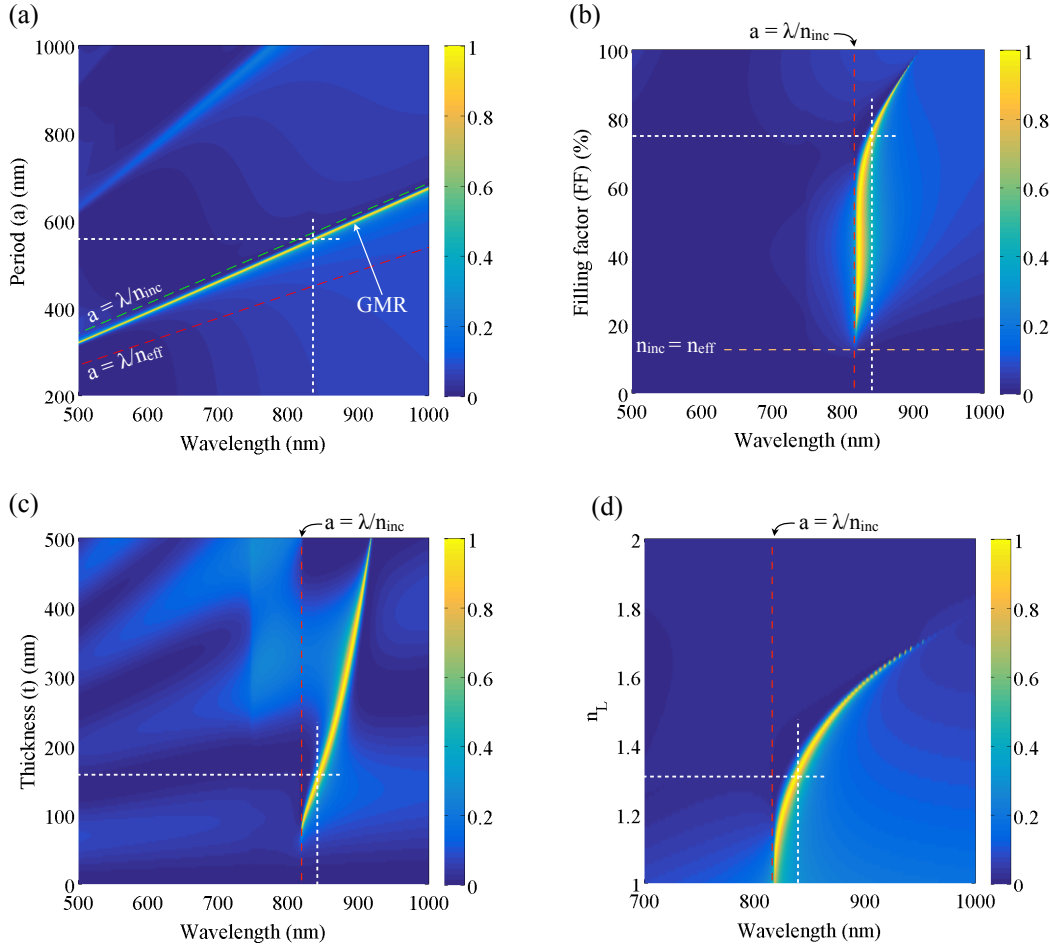


FIGURE 2.5: Reflectance surface plots with incidence wavelength on the x-axis and (a) period, (b) FF, (c) thickness and (d) n_L respectively. The white dashed lines indicate the parameters used in the grating that is designed to have a resonance wavelength of approximately 840 nm. Refractive indices are: $n_{inc} = 1.46$, $n_H = 2.00$, $\theta_{inc} = 0^\circ$. The other lines and indicators are discussed in the text. (RCWA simulation)

indicating the wavelength at which the grating becomes diffractive into the substrate. Additionally, when the FF drops below $\sim 16\%$ (the orange dashed line), the first inequality of eqn. 2.11 is no longer satisfied, so the grating layer is no longer able to support any guided modes and there is no resonance. For large FF, the grating is approaching a homogeneous waveguide and λ_R must increase with n_{eff} to fulfil the resonance condition. Finally, at 100% FF, there is no grating and therefore no resonance.

Figure 2.5(c) shows the dependence on grating thickness. The behaviour is similar to the case for FF (fig. 2.5(b)), and the resonance is again bounded by the red dashed line. Above a certain thickness, the grating is able to support the guided mode required for the resonance. Here, however, the wavelength dependence is quite clear, and is due to the higher wavelength required to phase-match with the reflected 0^{th} order. This plot is essentially a zoomed-in version of that shown in figure 2.4.

Lastly, figure 2.5(d) shows the dependence on the cover and groove index, n_L . Increasing n_L results in a higher value of n_{eff} , meaning a higher wavelength is required to meet the resonance condition. A similar dependence is seen for high FF values in figure 2.5(b), and again, the red dashed line creates a boundary for the resonance. An interesting feature seen here is the non-linearity of λ_R as a function of n_L , i.e. the sensitivity of λ_R to refractive index becomes higher at large index values - an important observation in the context of applying this grating as a biosensor.

2.5 Angular dependence and band structure

The final aspect of the resonant grating I present in this chapter is the dependence on incidence angle. Since the vertical symmetry is broken when $\theta_{inc} \neq 0$, the angles of diffraction of the ± 1 orders are different. Hence, two different guided modes can be excited simultaneously which are resonant at different wavelengths. To study these effects, I plot the reflectance versus wavelength and incidence angle. However, by translating θ_{inc} into k_x (the horizontal component of the wave vector \mathbf{k}), and plotting frequency instead of wavelength, the plot essentially becomes a band diagram.

Band diagrams (also known as a band structures [65]) are an integral part of crystal theory in solid state physics, and are applicable to both electronic and photonic crystals. The band diagram displays the dispersion relation of the structure: $\omega(k)$. In the context of photonic crystals, they are most often used to study the discrete set of allowed states for photons. These states lie below the "light line" ($\omega = \frac{c}{n}k$), where c/n is the speed of light reduced by the index of refraction in the medium surrounding the photonic structure. States below the light line are totally-internally reflected and do not have real propagation constants outside the structure. They are "bound states", i.e. spatially confined, and for this reason, the possible frequencies which the modes can assume are discrete and not continuous. This situation is analogous to the discretisation of energies of electrons confined around a hydrogen nucleus, for example.

Looking first at a conventional 1D photonic crystal, e.g. the dielectric stack represented in figure 2.1(a), but setting the permittivities to be equal ($\epsilon_1 = \epsilon_2 = \epsilon$), the dispersion relation becomes that of a homogeneous medium: $\omega = \frac{c}{\sqrt{\epsilon}}k$. This relationship is plotted on the graph at the right of figure 2.6, and is indicated by the arrow pointing to the straight diagonal black lines. Here, the periodicity means that the dispersion relation repeats for every multiple of $k_x = 2\pi/a$. Thus, there are degeneracies at the $k_x = \pi/a$ points, i.e. two modes with the same frequency. Now, if the permittivity is changed such that each layer is alternating, this degeneracy is lifted (purple lines in the graph) and the two modes assume either the high-frequency solution or the low-frequency solution, with each mode having

nodes concentrated in either the low- ε or high- ε material, respectively, as shown in the left-hand illustration.

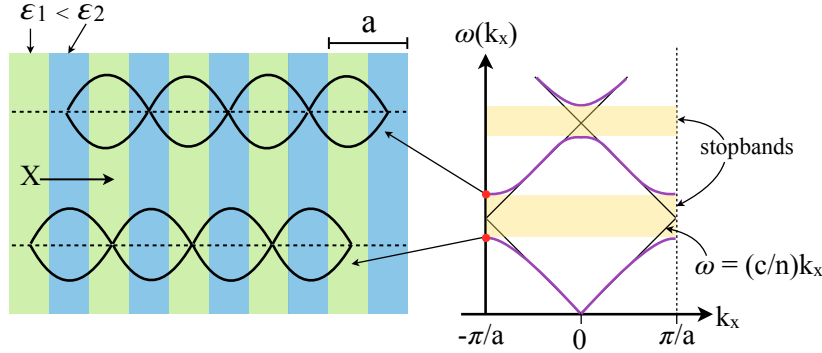


FIGURE 2.6: Illustration of the band structure of a 1D photonic crystal comprised of dielectric slabs of permittivities $\varepsilon_{1,2}$. The black diagonal lines in the graph on the right indicate the dispersion relationship for a homogeneous medium ($\varepsilon_1 = \varepsilon_2$), purple lines for the periodic structure ($\varepsilon_1 < \varepsilon_2$), and yellow regions indicate the stopbands. The band structure is shown in the reduced-zone scheme, hence the folding at $k_x = \pm\pi/a$. The left hand graphic shows the EM field profiles for two modes on either side of the stopband at $k_x = -\pi/a$.

The analysis of a resonant grating in terms of the band structure is slightly different to that of a conventional photonic crystal. Since the guided modes are excited using out-of-plane light in the RCWA simulation, the modes below the light line cannot be calculated. Nevertheless, these modes are not relevant here since my experimental work exclusively uses out-of-plane excitation. Above the light line, the available modes form a continuum instead of being discretised, and these modes have real propagation constants in the cover and substrate regions because they are not bound to the grating layer. Figure 2.7 shows the band diagram for the grating studied in this thesis (parameters are the same as in figure 2.3). $k_x = k_{inc} \sin(\theta_{inc})$ is used to translate incidence angle into the horizontal k-component.

In the lower right region (grey), lies the "photonic crystal" regime where modes are purely guided in the slab. Experimentally, these modes can be excited using in-plane light, or a grating coupler. Between the glass and water light lines lies a region of very high reflectance. This occurs due to total internal reflection at the interface between the grating and the cover, resulting in zero transmission through the structure. Across the continuum of states above the light lines, the guided modes are clearly seen, having a very similar shape to those found in pure photonic crystals as demonstrated in figure 2.6. These guided modes also exhibit band gaps associated with waves propagating through a periodic medium. At $k_x = 0$ (i.e. normally incident light) the guided mode resonance is seen at the upper edge of a stopband. This is consistent with the theory that the GMR arises when the in-plane guided modes are resonantly reflected from each grating interface to form a standing wave. This is in fact the second stopband of the structure, and it is well-reported in the literature that GMRs reside at the edges of the second stopband [66, 59]. As k_x (or equivalently θ_{inc}) increases, the resonance moves to a higher frequency (i.e. lower wavelength) because the

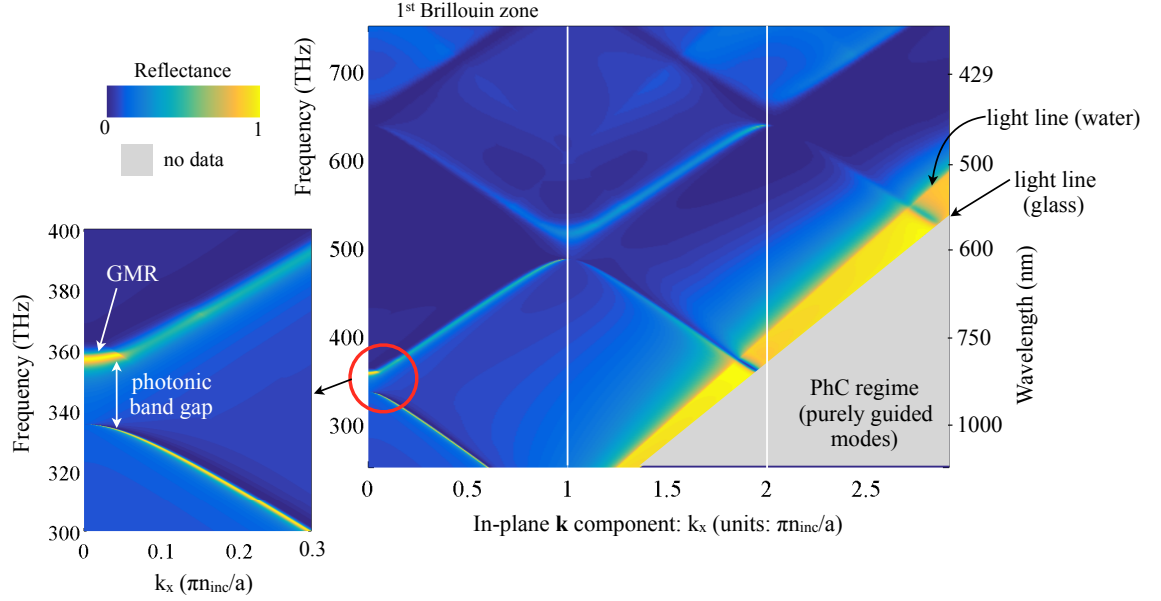


FIGURE 2.7: Photonic band diagram computed using RCWA by sweeping incidence angle and frequency. The structure is the same as the grating described in figure 2.3. The colour scale indicates reflectance. The inset shows the details of the photonic stop-band where the guided-mode resonance lies.

period of the grating appears smaller to the incident light. For this reason, guided mode resonances are particularly sensitive to incidence angle - an important consideration when designing an optical setup to measure them, as will be seen in the next chapter. Furthermore, a second resonance appears at the lower edge of the stopband, since the diffraction angles of the $m = \pm 1$ orders are no longer the same.

2.6 Cavity-based resonance

Although the majority of the results presented in this thesis are based on guided-mode resonances, another resonance mechanism was employed at the beginning of the work which was later deemed to offer inferior performance to the GMRs. However, the ideas have relevance to some parts of the thesis, and also to potential future work, so a brief description is given here.

As before, I begin with the case of a pure 1D photonic crystal that exhibits a stopband. Light with a frequency within the stop band cannot propagate through the crystal (in the direction of periodicity). It is well known that when the periodicity is disrupted by including a defect, a localised state can exist within the stopband [65, 67]. This is illustrated in figure 2.8, where one of the dielectric slabs is made thicker than the others.

I applied this idea of using a cavity to generate a resonance in a grating. Starting with a grating exhibiting a broadband region of high transmittance, a defect is introduced by

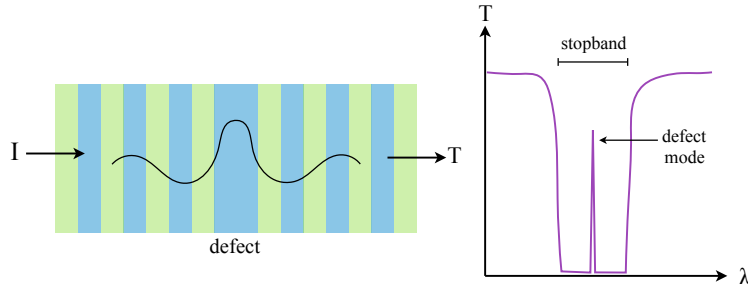


FIGURE 2.8: Demonstration of the introduction of a defect in a pure 1D photonic crystal, resulting in a defect mode that is spatially-localised and has a wavelength within the stopband.

increasing the width of every 5th grating ridge. Figure 2.9(a) shows simulated transmission spectra from such a grating, both with and without the defect, while an experimental measurement is shown in (b). This idea can be found in the literature, for example, by Zanotto et al. [68], who present a metal-coated grating that supports a defect mode. The motivation behind this approach is to prevent the lateral propagation of the guided modes associated with a GMR. As will be discussed in chapter 5, this effect reduces the spatial resolution of the biosensor. By creating a localised defect, however, the resonant mode is restricted from propagating laterally away from the defect because the grating either side acts as a mirror. Additionally, the cavity-based resonance becomes much less angular-dependent than a GMR, which is very practical during experimentation. Unfortunately, the size of the repeating unit (shown inset in figure 2.9(b)) must still be a few μm long, resulting in no drastic improvement over the spatial resolution offered by a GMR grating, as will be seen in chapter 5. A further disadvantage caused by such a long repeating unit (relative to the operating wavelength) is that it results in diffraction into the non-zero orders in the cover and substrate regions, thereby reducing the efficiency of any resonance effects.

2.7 Summary

In summary, this chapter has introduced the main ideas that describe the behaviour of the resonant gratings employed throughout the following chapters. In particular, guided-mode resonances have been the focus, which require certain conditions to be met before they come into existence. In brief, the effective index and thickness of the grating layer has to be sufficient to allow guided modes to exist, and the grating period must be such that it is subwavelength compared with the wavelength in the surrounding regions. In this case, light that is diffracted into the grating layer may couple resonantly to a guided mode that is subsequently rescattered to interfere with the 0th orders propagating outside the grating. The result is a narrow band of 100% reflection that is highly sensitive to the surrounding refractive index - a property that enables it to work excellently as a biosensor. Further simulations were employed to show how the resonance responds to varying different grating

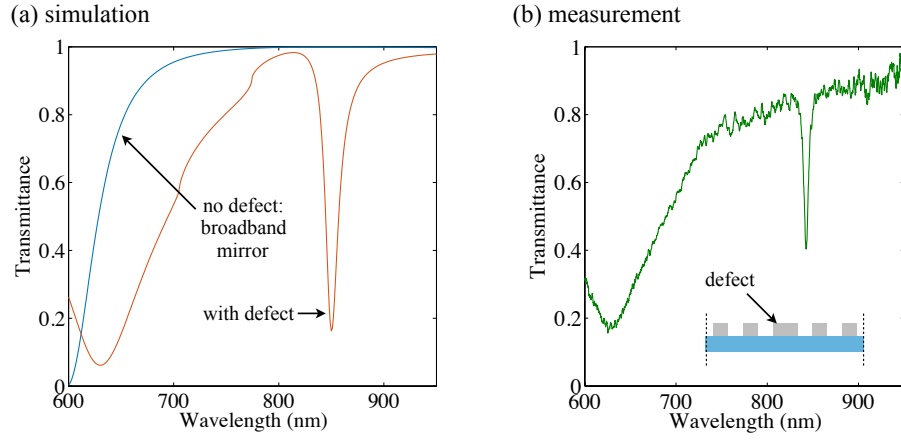


FIGURE 2.9: Simulated (a) and measured (b) spectra from a defect resonant grating. The blue curve in (a) corresponds to the grating having no defect, i.e. the central ridge is set to have the same width as the surrounding ridges, and the result is a broadband transmittance region. The addition of the defect introduces a resonance within this region, causing a dip in transmittance. This grating is fabricated in silicon ($n_H = 3.7$) with $t = 180$ nm, $n_{inc} = 1.46$, and $a = 340$ nm. The FF of the normal ridges is 26% while the defect has this increased to 38%

parameters such as period, fill factor and thickness. Next, the angular dependence of the resonant grating was investigated in the context of its band structure, where parallels can be made to a regular 1D photonic crystal. Finally, a defect-based mechanism for generating highly-localised resonances was introduced briefly, which was tested as a means to reduce the spatial resolution and the angular dependence of the sensor. However, as will be seen in chapter 5, this approach does not offer significantly better performance than the GMR resonance. The ideas discussed here have hopefully provided some insight into the behaviour and origins of the resonance, and will be beneficial in describing the results presented in coming chapters.

Chapter 3

Fabrication details & experimental methods

3.1 Introduction

The fabrication and measurement of gratings have formed significant aspects of my research. To reflect this effort, the chapter is divided into two parts. Firstly, the details of design and fabrication of a silicon nitride resonant grating are presented, and secondly, the experimental methods used in my research are demonstrated.

At the beginning of the project, our research group was in the process of relocating from the University of St Andrews to the University of York. This move saw our processing and measurement equipment installed in a new cleanroom and optics laboratory, and the installation of a newly-developed electron beam lithography system. As such, considerable time was spent developing and adjusting recipes for nearly all of our processes to give consistent fabrication quality using the new facilities. My personal contributions include the development of a protocol for creating gratings and photonic crystals in silicon nitride, and establishing a method for fabricating nanostructures on top of these gratings. In the optical laboratory, my contributions include: creating a bespoke optical setup to allow simultaneous imaging and spectral measurements of a sample, either in reflection or transmission; designing and constructing a bench-top tuneable narrow-band source; and developing planar microfluidic devices that fit within the working distance of a microscope objective lens. These achievements have not only been a fundamental part of my own research, but are now valuable to a number of other researchers in our group.

Additionally, I have worked extensively with the Evans group in the Biology department at York, learning the techniques of cell culture and making this accessible to our research group.

It has been a very rewarding experience to be involved with the setting up of our facilities, as it has allowed me to gain considerable knowledge of many nanofabrication tools and processes instead of simply treating them as a black box and being handed a recipe. The information provided here should be sufficient to allow the reader to repeat both fabrication steps and experimental measurements, and I hope will be helpful to future researchers.

3.2 Fabrication details

3.2.1 Choice of materials

Due to its relatively high refractive index and transparency at visible and NIR wavelengths, I chose silicon nitride (Si_3N_4) as the material in which to fabricate the resonant gratings. Si_3N_4 is also biocompatible [69], chemically inert [70], and mechanically robust, all of which are advantageous properties for its use as a biosensor material. Although crystalline silicon is a mainstay material for biophotonic structures, and is used extensively by our group and many others, it is etched slowly when exposed to cell media due to the slightly alkaline pH. It is therefore a poor choice for a biosensor intended to be exposed to cells for extended periods, although during my research I have developed a new protection method using a thermal oxide passivation layer. This research is still in its early stages, and it is therefore not included in this thesis. Si_3N_4 , on the other hand, is much more stable in biological environments, as is evident from its promising use in prosthetic limb joints [71, 72], and in cell culture by biologists employing environmental scanning electron microscopy (ESEM). Here a cell culture dish incorporates a very thin Si_3N_4 window on to which the cells adhere while allowing an electron beam to probe from below, through the nitride window [73].

The silicon nitride used here is deposited by PECVD (plasma-enhanced chemical vapour deposition) on to borosilicate glass wafers, and was sourced from Silson (UK). The glass wafers were chosen to be $500\mu\text{m}$ thick, to aid cleaving into smaller pieces. Because glass is amorphous, the cleaving often leaves an irregularly-shaped sample with uneven edges, however, this is not an issue since in-plane coupling to the high-index layer is not required, unlike the coupling to ring resonators or waveguide-based photonic crystals, for example.

In order to facilitate the modelling and design of the gratings (shown in a following section), the refractive index of Si_3N_4 is obtained from two sources [74, 75]. From this data, at a wavelength of 840 nm (the operating wavelength chosen for this work), the index is between 2.008 and 1.994 while the imaginary part (k) is zero. I therefore set the index to 2.00, between the two published values which are already very close. My simulations and experimental results are consistent, indicating that this value is reasonable. The choice of 840 nm as the target resonance wavelength is due to convenience. It lies within the tissue window, where absorption and scattering are typically low, and this wavelength is easily

detectable by a silicon CMOS or CCD camera sensor. Furthermore, this wavelength is far away from any visible fluorophore excitation/emission regions, leaving this space free for simultaneous fluorescence microscopy and resonance sensing.

3.2.2 Structure design

The design of the resonant gratings shown here was largely done computationally. Rigorous coupled-wave analysis (RCWA) was the principal tool used, with some finite-element analysis (FEA) modelling in COMSOL to observe electromagnetic field profiles within the grating. Finite-difference time-domain (FDTD) simulations were also used extensively at a later stage to investigate the spatial resolution performance of the gratings when they are used to generate resonance maps (please see chapter 5 for details on this). Brief details on the principles of RCWA are shown below.

3.2.2.1 Rigorous coupled-wave analysis

RCWA is a widely used method for calculating the diffraction efficiencies of a periodic structure [76, 77, 78]. The structure is composed of three regions: a grating region sandwiched between cover and substrate regions (figure 3.1). The grating is assumed to be infinitely periodic, and the cover and substrates both extend to infinity in the vertical direction. The refractive indices of all regions may be specified, along with the thickness, period and fill factor of the grating. Incidence wavelength (λ), angles (θ, ϕ) and polarisation are further input parameters.

In brief, the calculation begins with expressions for the total electric field in each region. For the cover region, this is the sum of the incident wave (I) plus all backward-travelling waves. For the substrate, it is the sum of all transmitted waves. Because the grating is an infinitely-periodic permittivity distribution, it can be expressed as a Fourier series where each Fourier harmonic corresponds to a diffractive order outside the grating layer. After including boundary conditions for the electric fields between all three regions (enforced by the Maxwell equations), the total electric fields may be re-written as a set of coupled-wave equations. These equations are then solved numerically to obtain the magnitudes of the reflected and transmitted diffracted orders (R and T).

By performing the calculation over a range of wavelengths, the R and T spectra are obtained. Furthermore, by dividing the grating layer into N slabs (figure 3.1), it is possible to model arbitrary grating profiles, such as a surface-relief grating or a sawtooth. RCWA was used extensively at nearly all stages of my research as an invaluable tool for structure design, and also for probing the sensitivity (by altering the refractive index of the cover region) and the angular tolerance of grating resonances. The calculations used in this work were implemented in MatLab using a script based on that by D. Brundrett published in

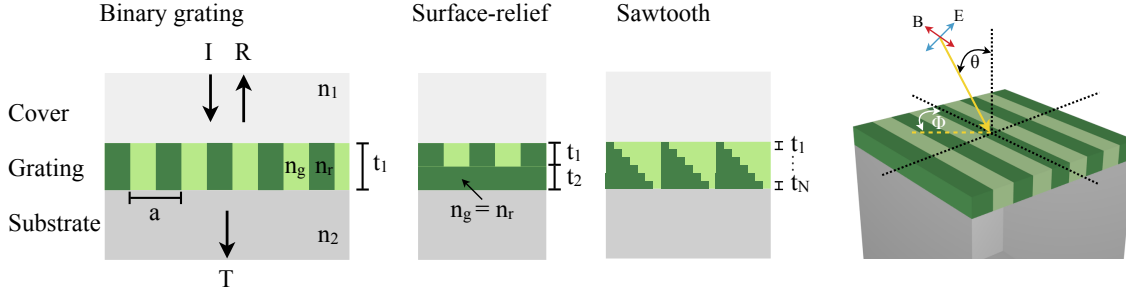


FIGURE 3.1: Geometry used in RCWA modelling.

[79], while scripts for sweeping the wavelength, period, duty cycle, refractive index, etc., were written by myself.

3.2.2.2 Particle swarm optimisation

While it is relatively trivial to find a design for a resonant grating by "brute-force", i.e. by calculating the output spectrum for all combinations of input parameters, this approach requires significant computing resources. Some time can be saved by performing the calculations in parallel across several computing cores if these are available. Yet, a far more elegant method is to use an intelligent algorithm to iteratively move towards the best combination of parameters for the desired spectrum. To this end, I wrote a particle swarm optimisation (PSO) program that can be used to identify the best grating parameters to give a desired resonance spectrum. This algorithm saves considerable computing time, allowing a target structure to be identified very efficiently.

Particle swarm optimisation (PSO) is a type of genetic algorithm first developed in the 1990s [80] to model the social behaviour of many-body systems. The technique was inspired by the complex interactions between birds in a flock, and can be applied to anything for optimisation purposes. My PSO program is loosely based on that presented in [81], but with some modifications. Each particle in the swarm is a point in the parameter-space (fig.3.2a), and undergoes a semi-random walk. For the case of a grating, the parameters might include period, filling factor, and thickness, for example, but there is no limit to the number of parameters. The path of each particle is pulled towards the best global location so far (social weight), and also that particle's own best location so far (cognitive weight). The best position is defined as that which minimises the difference (or error) with the target spectrum. Each particle also has an inertia value that controls how much its path is affected by the social and cognitive weights, and a random component. The result is a coarse probing of most of the parameter space, before honing on the best position. Figure 3.2 shows the results of the PSO process, which has successfully identified a grating that exhibits a resonance at 840 nm.

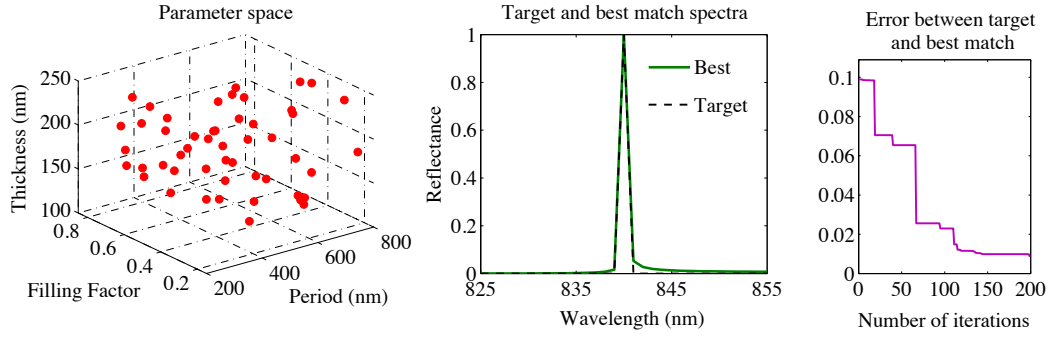


FIGURE 3.2: Demonstration of the PSO algorithm to find ideal resonant grating parameters.

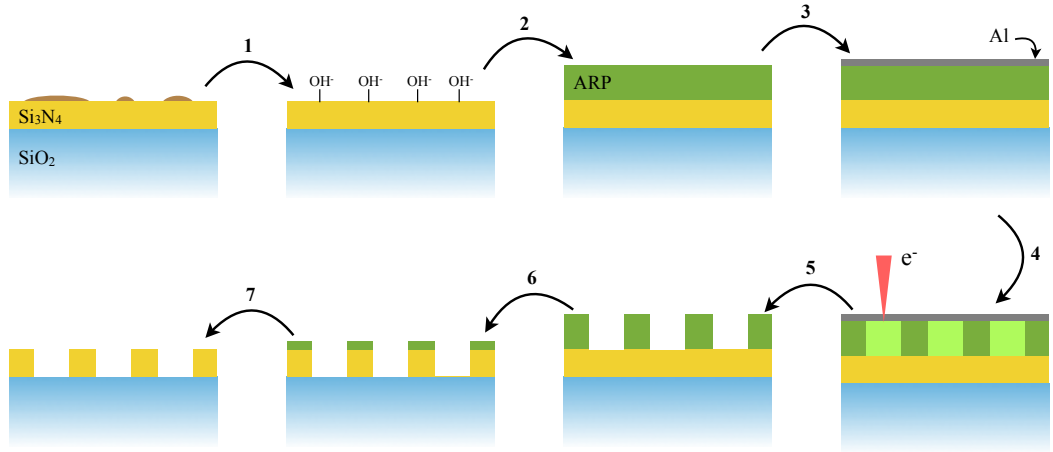


FIGURE 3.3: Fabrication flow diagram. Step numbers are referred to by each section below.

3.2.3 Device fabrication

The following sections discuss the details involved in the fabrication of the gratings shown in this work. The primary technique is electron-beam lithography, and the typical grating dimensions are as follows: period (a) = 560 nm; thickness (t) = 150 nm; filling factor (FF) = 0.75 (i.e. ridge width = 420 nm and groove width = 140 nm). An outline of the fabrication process is shown in figure 3.3 with details of each step in the following sections.

3.2.3.1 Substrate preparation (step 1)

Firstly, the substrate is cleaned thoroughly to remove any dust particles and organic material. For dust removal, sonication in acetone followed by a rinse in isopropanol is sufficient. Next, piranha solution removes any organic residue from the sample. Piranha is a mixture of 3 parts sulphuric acid H_2SO_4 to 1 part hydrogen peroxide H_2O_2 , and is a very widely-used cleaning method. It is a two-stage chemical reaction: firstly, the sulphuric acid acts a rapid dehydrator, extracting hydrogen and oxygen as water, leaving the organic material carbonised. The second stage, which occurs over a longer timescale, is the oxidation of the remaining elemental carbon. Piranha cleaning is quite exothermic and highly active, hence the name. As well as removing organic residue, piranha cleaning leaves the substrate surface

hydrophilic by creating hydroxyl (-OH) groups, making spin-coating easier and improving the bonding of the resist to the substrate.

3.2.3.2 Spin-coating of electron beam resist (step 2)

To achieve a very flat and even resist layer of a specific thickness, spin coating gives reliable results. After cleaning, the substrate is loaded into a spin-coater, and is held in place by vacuum during the spin. By altering the spin speed, acceleration and duration, the film thickness can be controlled down to accuracies of tens of nm or even less. I worked with AR-P 6200.09 (ALLRESIST) [82], which has a high sensitivity to electron exposure (step 4), good resistance to plasma etching (step 6), and can achieve structure sizes as small as 6 nm.

The resist is spin coated at a speed of 3000 rpm for 60 seconds, and is then cured on a hotplate at 180 °C for 10 minutes.

3.2.3.3 Deposition of charge dissipation layer (step 3)

Since a Si_3N_4 film on glass has a high electrical resistance, it exhibits significant charging during electron beam exposure. Unfortunately, this occurs for electron-beam lithography and in SEM (scanning electron microscope) analysis, distorting the shape and position of the beam. The consequences are over-exposure of the resist and inaccurate patterns. To solve this issue, a thin layer of aluminium is evaporated on top of the cured resist using a Mantis Hex thermal evaporator. Thermal evaporation is a simple method of depositing thin films, and is achieved through resistive heating of the material or by electron beam heating. Our evaporator is a resistive heating system. A small quantity of high purity aluminium is placed in a tungsten boat that is connected to a high current power supply. The chamber is pumped down to a pressure of 10^{-6} mbar before ramping up the current passing through the boat. The low chamber pressure and high boat temperature causes the Al to melt and vaporise, before condensing on the substrate which is situated above the boat.

At a thickness of 20 nm, the Al film is thin enough to have a negligible effect on the penetration of the incident electron beam during the lithography step, while still preventing charge building up.

3.2.3.4 Electron beam lithography (steps 4 & 5)

Once the charge dissipation layer has been deposited, the sample is ready for electron beam lithography. This form of lithography followed on from UV photolithography after the invention of the electron microscope. Instead of raster-scanning a tightly-focused beam of electrons (SEM), the beam is steered to expose specific areas of the sample. Upon electron

exposure, the chemical structure of the resist layer is changed, either allowing it to be dissolved in a solvent (positive tone resist), or preventing it from being dissolved in a solvent (negative tone resist). For a positive resist, the electrons destroy linkage bonds in the resist polymer to increase solubility. For a negative resist, the polymer molecules are cross-linked by electron exposure, rendering them insoluble. Exposure of a negative tone resist is often accompanied by a post-exposure cure to enhance the cross-linking and further decrease solubility. In analogy with film photography, the process of removing exposed regions with a solvent is called development.

With electron beam lithography, the beam size can be focused down to a few nm because of the shorter wavelength of high-energy electrons compared to UV photons. This allows patterns to be exposed at a very high resolution. Importantly, the smallest exposure size is not the diffraction limit because there is significant scattering and diffusion of the electrons within the sample [83]. In particular, back-scattered electrons from the interfaces within the sample being exposed cause a widening of the exposed area. This effect is largely dependent on the properties of the sample being exposed. Another detrimental effect is proximity error. This is a direct result of the scattering of electrons in the sample, where the centre of an exposed region receives a higher dose than the edges and, especially, the corners. Our lithography system includes software (NanoPECS) for calculating a correction factor that forces the beam to stay at the corners and edges of a polygon for longer, ensuring the dose everywhere is close to equal. I did not require this tool for much of my fabrication, as the edges and corners of a grating sensor are an insignificant proportion of the sensing surface and can often be ignored during operation.

Our electron-beam lithography system is a Voyager from Raith GmbH, and incorporates a fully electrostatic column for beam steering. This enables very quick writing speeds compared to more usual electromagnetic steering; up to 1mm^2 of grating in less than 5 minutes. The areas to be exposed are first defined in CAD (computer-aided design) software, or defined as sets of coordinates in an ASCII file. I often made use of a MatLab script to generate the ASCII design file, as it is far more efficient than using CAD software.

AR-P 6200.09 is a positive tone resist, meaning the exposed regions are removed. The clearing dose used here is $130\mu\text{C}/\text{cm}^2$, and was determined after dose tests until the exposed region was seen to be cleared fully after development. I note that this value is dependent on the sample substrate material and the resist properties such as thickness and curing temperature, and is therefore not universal. Once electron beam exposure is complete, the charge dissipation layer must be removed before development otherwise it prevents the solvent accessing the resist layer below, acting like a shell. To strip the aluminium, the whole sample is placed in a solution of warm (40°C) phosphoric acid (H_3PO_4), for 3

minutes. The acid is a very fast etchant of aluminium [84] but also attacks silicon nitride, however at negligible etching rate compared to aluminium [85, 84, 86]. The stability of the resist to phosphoric acid is not found in literature, but there is no apparent degradation, and the resist performance is the same after exposure to the acid. Development of the resist is 2 minutes in Xylene, at room temperature, followed by a rinse in isopropanol.

The result, after development, is a patterned layer of resist, where the exposed regions have been removed to leave windows open to the Si_3N_4 layer below. The resist acts as a shield, as the name indicates, against the plasma etching step that is detailed in the following section.

3.2.3.5 Pattern transfer using reactive ion etching (RIE) (step 6)

To transfer the pattern from the resist into the Si_3N_4 layer I use a dry etching process widely used in the CMOS and integrated circuit industry known as reactive ion etching (RIE). RIE is a plasma-based process that can take place in a reactor as shown in figure 3.4. The carbon stage and gas shower act much like a parallel-plate capacitor.

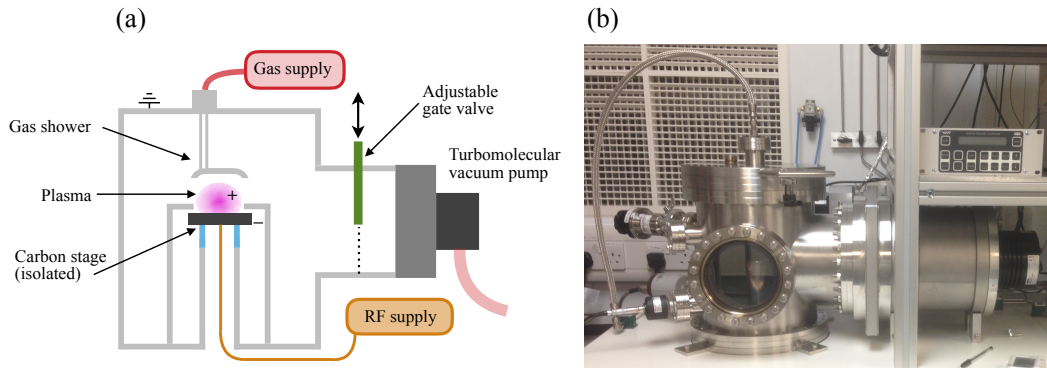


FIGURE 3.4: (a) Diagram and (b) photograph of our RIE system.

A plasma is an ionised gas which, due to the charged constituent particles, exhibits collective behaviour [87]. The role of the plasma in RIE is to generate reactive ions and radicals, such as fluorine (F^+) from the input gases [83]. These go on to react with the material to be etched. For the system used here, the gas shower (anode) is conductive but grounded while the stage (cathode) is electrically isolated from the rest of the system and coupled to an AC power supply driven at RF frequency (13.56 MHz). An AC electric field is activated between the two plates which strips electrons from the gas molecules (gas breakdown), igniting a plasma. The characteristic glow (also observed in gas discharge lamps and the Aurora) is caused by the relaxation of gas molecules that have been excited inelastically by a free electron, with the emission colour being specific to the type of gas. The electrons, being less massive, accelerate to the upper plate more quickly than the ions and are lost to ground. This leaves the plasma with an overall positive charge. Because

the carbon stage is isolated, there is a buildup of electrons here giving it a negative charge. Consequently, positively charged ions in the plasma are attracted to the stage. During the etch, the sample is situated on the stage and is etched by particles from the plasma via two mechanisms:

- Mechanical etching: occurs when material from the sample is ballistically ejected by an ion from the plasma as it accelerates towards the cathode. From the vertical acceleration, this mechanism is highly anisotropic, and it is analogous to the removal of target material in sputter deposition.
- Chemical etching: occurs when the creation of highly reactive species in the plasma react with the sample material to form volatile compounds that are removed by the vacuum system. Because these reactive species are not usually charged, they reach the sample by diffusion and give an isotropic (non-directional) etch.

By changing the pressure of the gases, the mean free path (MFP) of the particles in the plasma is altered. A low pressure equates to a longer MFP, allowing the ions to gain more momentum before hitting the sample, resulting in a more mechanical etch. Higher pressure, in contrast, causes a shorter MFP and therefore more frequent collisions before reaching the sample. This enhances the production of reactive species as well as slowing down the ballistic ions, giving a more chemical etch. The two mechanisms must be tuned in order to give the best etch results in terms of etch rate, selectivity (ratio of etch rates of Si_3N_4 and resist), minimal roughness, and vertical sidewalls (anisotropy). If mechanical etching dominates, material being sputtered back onto the sample causes roughness, but the sidewalls remain highly vertical. Also, selectivity and speed become poor, and sample damage is a possibility. If chemical etching dominates, the sidewalls become more rounded but selectivity and speed can be excellent, as well as low roughness. The chamber pressure, AC power and gas flow rates are tweaked to give the correct balance between chemical and mechanical etching. The mixture of reaction gases is also crucial, and depends on both the material being etched and the resist [83]. Additionally, by tailoring the chemistry of the reactive gases it is possible to form a passivation layer on the sidewalls, another mechanism for achieving high anisotropy. For Si_3N_4 , I use a mixture of fluoroform (CHF_3) and oxygen (O_2) at a ratio of 29:1 (developed by Dr. Yue Wang in our group). The CHF_3 is broken down by collisions in the plasma to fluorine which etches the Si_3N_4 chemically [88]. The small addition of O_2 readily binds to the hydrofluorocarbon ions remaining in the plasma and decreases the chance of the fluorine radicals recombining, thereby increasing etching efficiency.

By setting the pressure to 0.2 mbar using the gate valve, and the RF power to 39 W, the nitride is etched smoothly and vertically at a rate of around 23 nm/min. I therefore etch for 7 minutes to fully clear the 150 nm thick layer.

3.2.3.6 Final cleaning (step 7)

The final stage in sample fabrication is to strip off any remaining resist. A solvent (1165 Microposit Remover, Shipley) dissolves the resist after 5 minutes of gentle sonication. To remove any residue left from the stripping, a rinse in acetone then isopropanol is used before drying with nitrogen.

3.2.4 SEM analysis

Once fabrication is complete, the grating is ready to be prepared for biosensing, as will be described in detail in the next chapter. SEM images of the finished device are shown in figure 3.5. Due to the Si_3N_4 and SiO_2 substrate being highly resistive, as mentioned previously, SEM imaging is only possible if a thin layer of metal is applied to the structure. Here, a 7 nm thick layer of platinum-palladium alloy is sputter-coated before viewing in the SEM. Unfortunately, the Si_3N_4 and SiO_2 layers cannot be distinguished after they are coated with metal.

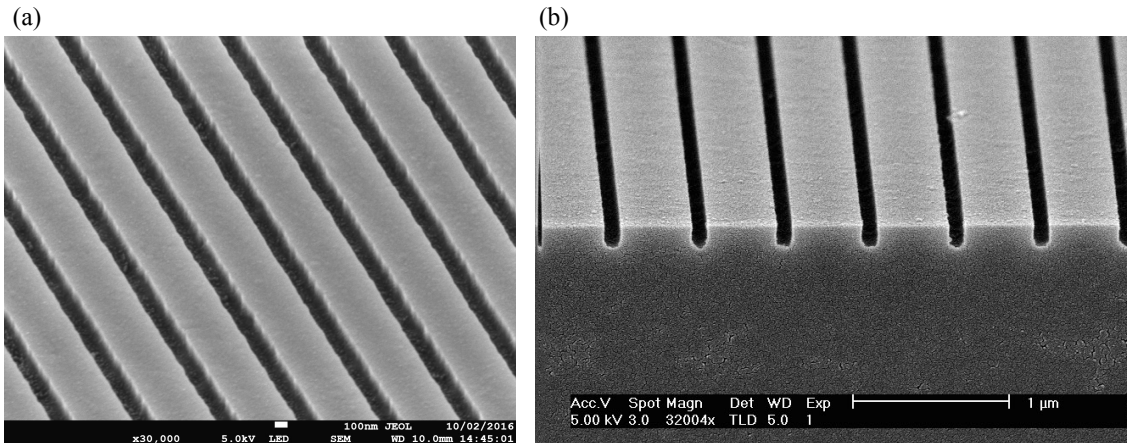


FIGURE 3.5: SEM images of the finished grating, including thin metal charge-dissipation layer.

3.3 Experimental methods

Throughout this thesis, three different measurement techniques have been implemented. The first is a measurement of the resonance wavelength from a large area of the grating as a function of time, much like a conventional biosensor. This measurement allows the monitoring of binding events, for example, but lacks any spatial information. Spectral data is typically acquired using a CCD spectrometer. Measurements in the chapter on sensing (chapter 4) are mainly performed using this method.

The second measurement technique acquires the same sensing information from monitoring the resonance wavelength, but it is spatially resolved. This measurement concept was illustrated in figure 1.2 (chapter 1), and previously in figure 5.2. The result is a "resonance

map” of the surface, which indicates local variations in refractive index. To achieve this, a sequence of brightfield images of the surface is acquired whilst tuning the illumination wavelength. Each image, or slice, in the resulting stack of images corresponds to a single illumination wavelength, so the z-dimension of the stack contains the spectral response of each pixel. Thus, the resonance wavelength can be determined for every pixel, allowing a resonance map to be created. This measurement can be repeated over time to monitor the evolution of the resonance wavelength as changes at the surface take place, and is seen extensively in chapters 5, 6 and 7.

The third technique is employed in the chapter on the chirped GMR biosensor. Here, the focus is on a very simple, compact and robust device that utilises a novel chirped grating sensing element. In essence, the chirped grating translates resonance information into spatial information on the chip, so illumination is with a single wavelength and no sweeping or scanning is necessary. The monochromatic illumination light resonates with only one region of the chip, and the *location* of this resonance is extracted simply by imaging the grating onto a camera. Further details of the chirped grating measurements are presented in chapter 7.

3.3.1 Measurement setups

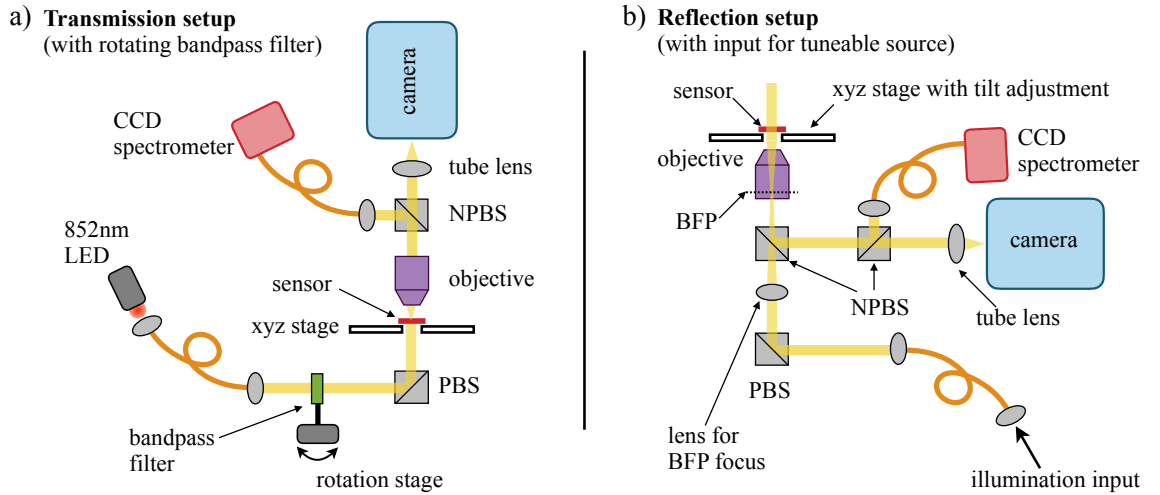


FIGURE 3.6: Diagrams of the measurement setup in (a) transmission and (b) reflection configurations. (N)PBS = (non)polarising beamsplitter, BFP = back focal plane.

At the outset of the project, the spectral response of the resonant grating was measured in transmission using the setup shown in figure 3.6(a). Measuring the transmitted light is simpler for two reasons: the angle of the sample does not need to be perfect, and the incident light reaches the grating *before* it passes through the objective lens, meaning it is easy

to keep highly collimated at the grating. Collimation is crucial due to the low angular tolerance of the guided-mode resonance (seen in section 2.5), and illumination with divergent or convergent light causes undesirable broadening of the resonance. But the transmission setup is not without drawbacks. In particular, the incorporation of a flow channel to deliver liquid to the sensor becomes challenging because it must be thin enough to fit between the chip and the objective lens. Not only is this difficult to engineer - the choice of objective lenses is also limited to those with a large enough working distance. Furthermore, the image quality is reduced since light must pass through any biological material on the sensor and through the flow channel material before being collected. This causes unwanted scattering and refraction.

In light of these drawbacks with the transmission measurement, I also constructed a reflection setup (3.6(b)). This configuration solves the two drawbacks encountered in transmission measurement: there is no restriction on flow channel thickness and imaging quality is improved since the collected light has passed only through the chip substrate (which is polished) and is not distorted by biological material or the flow channel. Moreover, the objective lens working distance must only exceed the substrate thickness of $500\mu m$ allowing a wider variety of objective lenses to be used.

Despite these rewards, there are new limitations. Firstly, the amount of collected light is highly sensitive to the angle of the sample so this must be aligned carefully using an adjustable stage. Secondly, the incident light must remain collimated after passing through the objective lens. One solution is to illuminate at an oblique angle and collect at the corresponding reflection angle, but this would require a long working distance objective lens and is not suitable for imaging large areas of the surface. Instead, I opted to focus the illumination light down to a spot in the back focal plane (BFP) of the objective lens to ensure it exits the front of the objective as a collimated beam. While this solution works in principle, in practice the collimation is not perfect because the spot in the BFP is not diffraction-limited. The collimation problem is exacerbated when using high NA objectives which translate an increased BFP spot size into even bigger divergence of the beam leaving the front of the objective. Nevertheless, by minimising the BFP spot size, the divergence angles of the light exiting the objective were small enough not to cause concern ($< 1^\circ$ for a 5x objective).

The advantages and disadvantages of the two configurations are summarised in table 3.3.1.

	Advantages	Disadvantages
Transmission	Easy to collimate incidence light. Sample angle is not critical.	Flow channel must fit between sample and objective. Imaging light affected by flow channel and bio. material.
Reflection	Unrestricted space above sample for flow channel. Imaging light only passes through sample substrate.	Difficult to collimate incidence light. Sample angle is critical.

All of the mechanical components used in the setups are standard Thorlabs parts. Lenses and beamsplitters are also sourced from Thorlabs, while objective lenses are Olympus NeoDPlan (5x (NA = 0.13), 10x (NA = 0.25), 20x (NA = 0.46)). For high-magnification imaging I used a water-immersion objective lens from Nikon (CFI APO 60x NIR, NA = 1.00). The camera is a CoolSnap Myo from Photometrics, and the spectrometer is a Thorlabs CCS175. The optical fibres used are multimode (50 μ m or 200 μ m core diameter), with NAs of 0.22 (Thorlabs M14L01 and M92L01). To collimate light exiting the fibres and collect light into a fibre, pre-mounted lenses were used (F240SMA-780). Finally, a halogen lamp was employed as a generic broadband light source for measuring spectra over a large wavelength range (Ocean Optics HL-2000).

3.3.2 Tuneable illumination

A fundamental aspect in either of the above measurement setups is the incorporation of a tuneable narrow-band source. This is necessary for the measurement of resonance maps, where spectral information is obtained by sweeping the illumination wavelength while taking a brightfield image at each wavelegnth. Explained below are two different tuneable illumination systems I have developed, each with its own advantages.

3.3.2.1 Rotating bandpass filter

Initially, I opted to use an LED (Thorlabs M850L3) with a narrow bandpass filter (Semrock LL01-852) situated on a rotation stage (Thorlabs CR1/M-Z7). By choosing a dichroic bandpass filter, which works using thin-film interference, changing the angle of the filter relative to the incident beam changes the central wavelength of the passband. This is because the condition for constructive interference varies with the cosine of the angle of incidence [89]. The biggest advantage here is the small footprint of this illumination system. It can fit onto a small breadboard along with the rest of the setup, making it portable, and no despeckling is needed as the source is incoherent. Despite the simplicity and efficacy of this tuning method, and low cost, the bandwidth of the output is limited to the width of the filter passband and the tuning range is quite small (< 30 nm). Moreover, it can

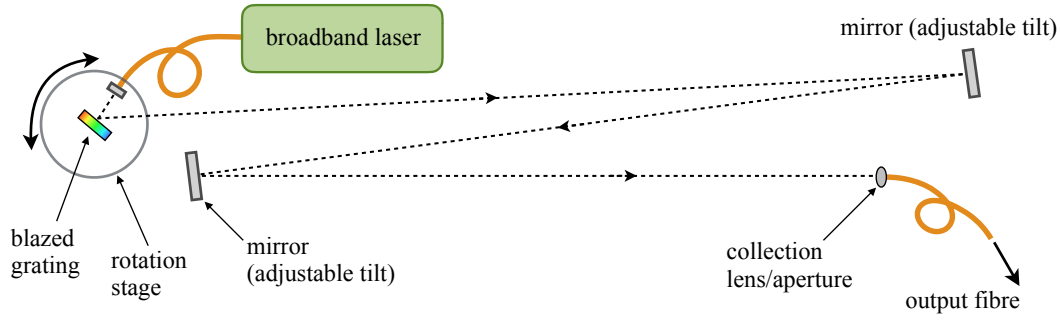


FIGURE 3.7: Diagram of tuneable illumination setup.

only be tuned towards bluer wavelengths due to symmetry about the rotation axis, and the transmitted intensity drops off as the angle of incidence is increased. These limitations along with the need for greater spectral resolution motivated the development of a different tuneable illumination system based on dispersion from a blazed grating and is discussed next.

3.3.2.2 Blazed grating filter

As is usual in a monochromator, broadband input light is incident on a blazed grating (Thorlabs GR25-1208) that disperses it into the usual diffraction orders (figure 3.7). The blaze ensures a higher diffraction efficiency into the first diffracted order instead of the zeroth order, making it ideal for use as a dispersive element. Here, a supercontinuum laser (Leukos SM30) was used as a source providing high spectral intensity white light. In my setup the incidence angle of light on the blazed grating remains fixed and the first diffracted order is directed towards a mirror on an adjustable mount. After travelling back to a second mirror, it then enters a fibre through a focusing lens to give a path length of 5 m. The collection lens has a radius of 5 mm, and acts like the exit slit of a monochromating system. Rotation of the blazed grating changes the wavelength collected by the fibre, and the long path length ensures a narrow bandwidth of < 1 nm.

This source gives a much smaller bandwidth in comparison to the bandpass filter. The tuning range is also considerably larger (~ 350 nm), and the bandwidth can be controlled by changing the path length between the blazed grating and the collection fibre, or by modifying the collection lens aperture. Figure 3.8 shows the capabilities of the blazed grating tuning system. The disadvantage of this source is that it has a relatively large footprint and is not as portable as the rotating filter method.

A comparison of the outputs from the two tuneable sources is shown in figure 3.9(a), along with the measurement of a narrow (~ 1 nm) grating resonance (figure 3.9(b)). In (b), the transmittance response from the grating is measured with the Thorlabs spectrometer

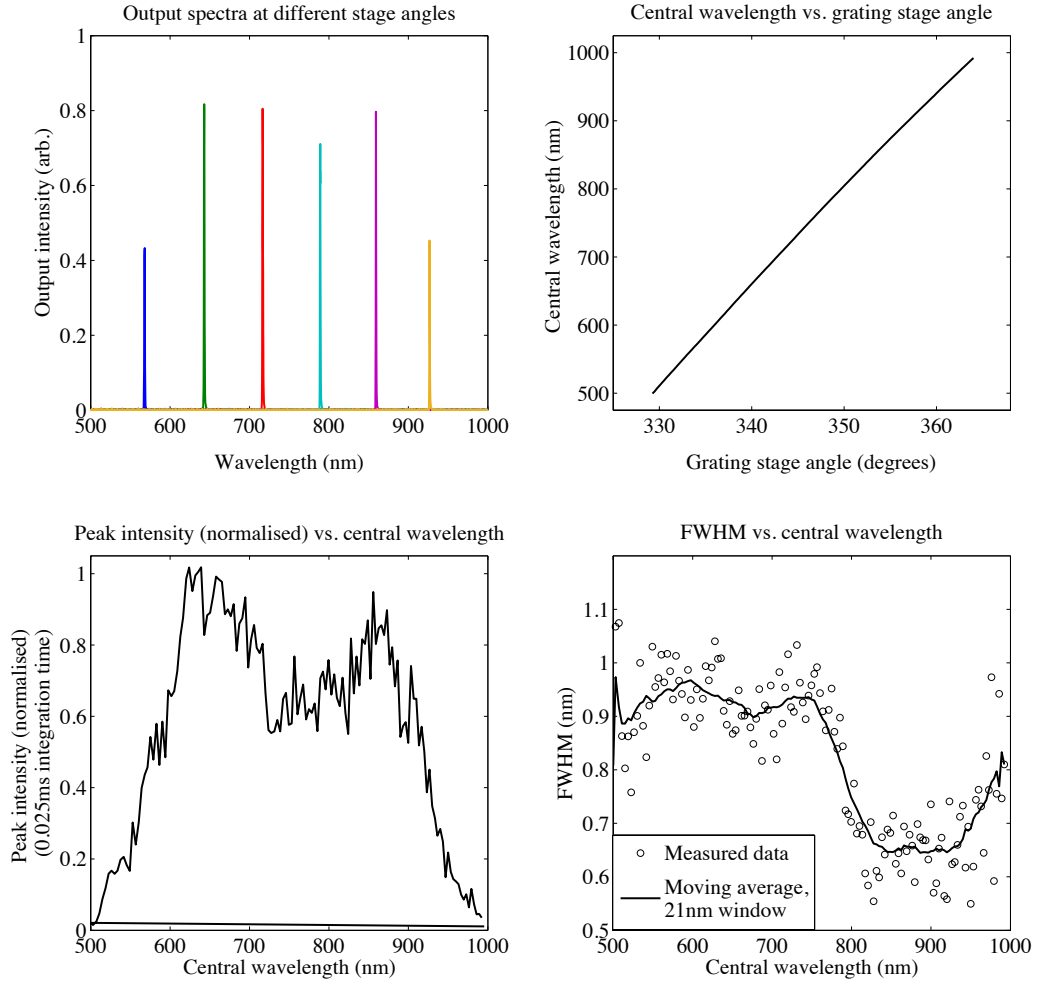


FIGURE 3.8: Monochromator characterisation, measured using the Thorlabs spectrometer.

(black line), and then with each of the tuneable sources. In these cases, the pixel intensity is monitored while the source is swept across the resonance to give the transmittance spectrum. For the bandpass filter (blue line), even with a small step size of 0.25 nm, the measured resonance is rounded-off due to the bandpass filter being broader. Exploiting the narrower linewidth of the blazed grating (blue line) allows the resonance to be resolved more finely.

The control of the rotation stage, camera and spectrometer is achieved through LabView programs. For the case of the rotation stage, which is used for wavelength tuning, the programs include a calibration step to ensure accurate tuning.

3.3.3 Microfluidics

A crucial part of most biosensors, especially lab-on-a-chip devices, is the design and construction of microfluidics to deliver an analyte to the sensor [90, 91, 92]. The following sections show details of two microfluidic devices used in this work.

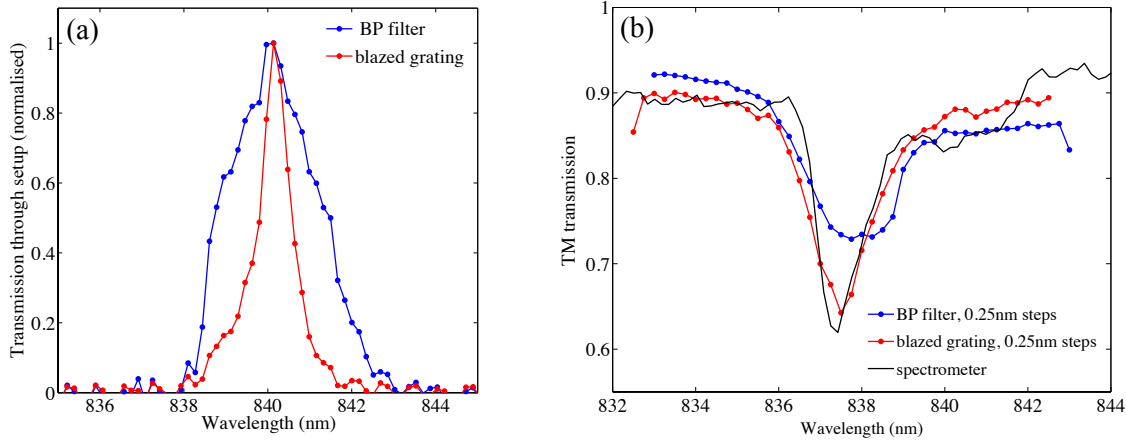


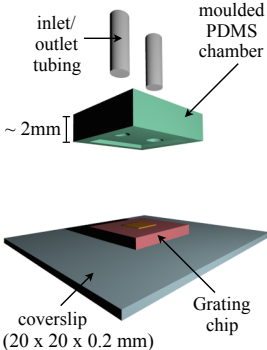
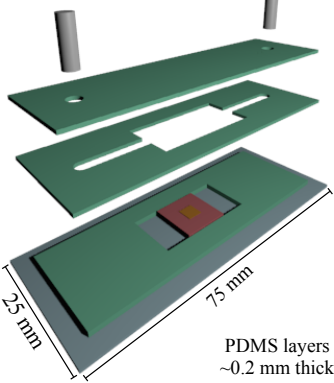
FIGURE 3.9: (a) Output spectra and (b) measurement of a narrow resonance (a GMR) using the different tuneable sources.

3.3.3.1 Flow channel

As discussed in section 3.3.1, the flow channel design depends on whether the measurement is being done in transmission or reflection. Figure 3.10 shows a table with details of two different designs I have developed to accommodate this, and a photograph of a finished sensor with flow channel design 1. Poly(dimethylsiloxane) [PDMS], a cornerstone material for microfluidic devices [93, 94], is used as the material for the flow channels, and is shown in green in the schematics. Prepared at a ratio of 10:1 (base:hardener), it gives a flexible yet robust elastomer after curing at 60 °C for two hours. There are a various ways to bond PDMS to a substrate or to itself [95, 96, 97], but here I rely on using uncured PDMS as an adhesive between surfaces to be bonded [98]. Further heating for 30 minutes is enough to cure this adhesion layer, and to strengthen the bond between PDMS and Si_3N_4 or glass, the chip can be first cleaned with piranha solution. Typically, the grating chip is also bonded to a glass cover slip or microscope slide using UV-curable optical adhesive (Norland).

3.3.4 Summary

In summary, the first half of this chapter presented details of the fabrication process employed for creating the gratings used in this work. First discussing material choices, the structure design process was then demonstrated, using RCWA simulations and a particle swarm optimisation algorithm. Once the desired grating parameters have been determined, the grating is fabricated using electron beam lithography and reactive ion etching, with each step of the process being discussed in detail. The second half of the chapter explored the main experimental methods employed throughout the thesis. In particular, both reflectance and transmittance measurement setups were shown, with two different approaches to achieve tuneable monochromatic illumination: a rotating bandpass filter, and a blazed

Design	1	2
Drawing		
Reflection	✓	✓
Transmission	X	✓
Fabrication	<ul style="list-style-type: none">• Mould used to create PDMS chamber• Chip bonded to coverslip using UV adhesive	<ul style="list-style-type: none">• Multilayer PDMS approach• Each layer patterned then stacked to realise a 3D channel• Chip bonded to microscope slide
Notes	<ul style="list-style-type: none">• Simple to fabricate & robust• Mould used to make cavity in PDMS block• Turbulent flow at sensor surface helps mixing	<ul style="list-style-type: none">• Difficult to fabricate, fragile• Multi-layer construction from thin PDMS• Laminar flow across sensor surface slows mixing

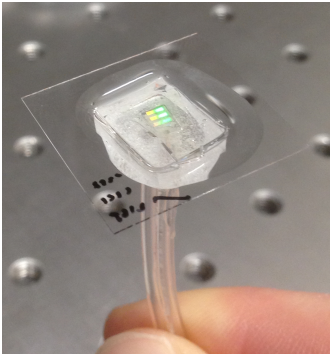


FIGURE 3.10: Table with comparisons between the two different flow channel designs, and a photograph showing the finished channel (design number 1).

grating monochromator. Lastly, details of the microfluidic flow channels used in the sensing experiments have been demonstrated.

Chapter 4

Sensing

4.1 Introduction

The operating principle of a resonant grating, when used as a sensing tool, is its response to changes in refractive index. This chapter focuses on investigating the performance of the Si_3N_4 grating presented in the previous two chapters to such changes by studying the sensitivity and limit of detection. Following this, the chapter presents a discussion on sensor functionalisation, which is a crucial step in making the sensor specific to a particular target molecule. A full demonstration of this is shown where the sensor is used to detect the binding of the biomolecule IgG.

4.2 Resonance characterisation

The key to monitoring small refractive index changes at the sensor surface is the grating resonance. The Si_3N_4 grating reported here in fact supports two different resonances, depending on whether the incident light is TE or TM polarised. Throughout this thesis, I refer to the "TE mode" as the resonant mode excited with TE-polarised light (i.e. \mathbf{E} parallel to the grating grooves, or perpendicular to the grating vector \mathbf{G}), and the "TM mode" being that excited with \mathbf{E} perpendicular to the grating grooves. Figure 4.1(a) shows the measured reflectance spectra for these two resonances, acquired using the reflection setup that was shown in figure 3.6(b) of the previous chapter. Figure 4.1(b) shows a normalised version of the TM resonance.

Included in these plots are Fano resonance curves that have been fitted to the data. As discussed in chapter 2, a Fano lineshape is chosen because the physical origin of the resonance is an interference between the thin-film response of the grating layer and the Bragg resonance of the guided-modes. Here, the thin-film response can be thought of as a slowly-varying background process, such that the overall response has a typical Fano

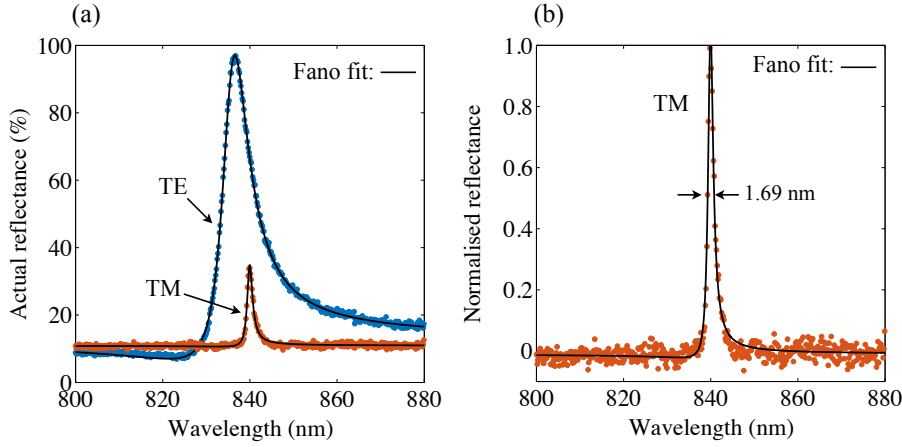


FIGURE 4.1: (a) Reflectance response measured from a resonant Si_3N_4 grating. TE (blue) and TM (red) resonances are shown; (b) Normalised version of the TM spectra to indicate FWHM, or linewidth. Black lines are Fano curves fitted to the data as described in the text.

lineshape [54]. However, for the gratings shown here, the Bragg resonance dominates, such that the Fano shape tends towards a Lorentzian shape. This is particularly true for the narrow (TM) resonance, although the characteristic Fano dip is seen more clearly for the TE resonance, suggesting that the thin-film background response should not be ignored. The equation used for the Fano fitting is of the form:

$$R(\lambda) = \frac{a(bc + \lambda - \lambda_R)^2}{c^2 + (\lambda - \lambda_R)^2} + d \quad (4.1)$$

The parameters in this equation are as follows: a is a scaling factor, b is the "Fano" parameter, c is related to the resonance linewidth, and d is a vertical shift parameter, required because the background of the measured curves is not zero. This equation is used in the built-in curve-fitting toolbox in MatLab, where a non-linear least-squares method is applied. By fitting a curve to the measured data, the resonance wavelength can be extracted much more accurately than if the raw spectrometer data is used. The quoted resolution of the spectrometer is 0.6 nm for a wavelength of 633 nm, and it is a reasonable assumption that this scales to ~ 0.8 nm for a wavelength of 840 nm. Moreover, the detector pixel resolution in the wavelength range of 800 - 899 nm has been measured to be 0.1695 nm/pixel. Of course, this value does not equate to a spectral resolution, which is also determined by the optics of the spectrometer, the entrance slit size, etc. For example, a monochromatic signal of bandwidth less than 0.1695 nm will almost certainly illuminate more than one pixel on the detector array. In addition to allowing more accurate spectral readout, the curve fitting also reduces the effect of random measurement noise in the raw signal.

To further study the properties of these two resonances, the grating was modelled using finite element analysis in COMSOL. Figure 4.2 shows the amplitude of the electric field at the resonance wavelength for the TE and TM modes. As expected, the modes take on

quite different spatial profiles, and it is evident that the TM resonance has a higher field strength by a factor of 3. This is consistent with the higher Q-factor of this resonance. Visually, the electric field looks to concentrate around the edges of the Si_3N_4 ridge for the TM mode, while the TE mode has more rounded lobes concentrating either in the centre of the ridge or in the grating grooves.

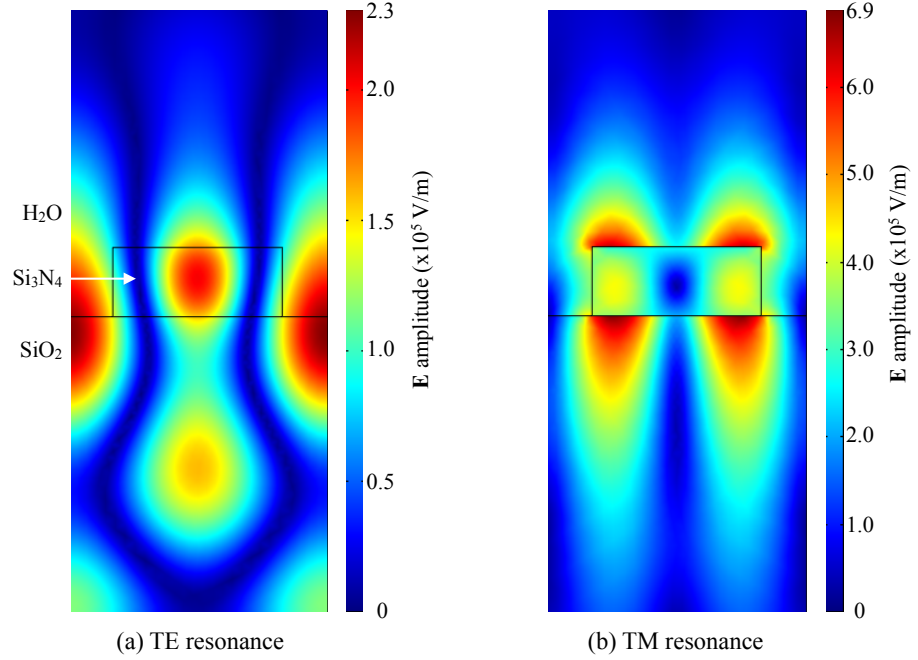


FIGURE 4.2: Simulated electric field amplitude, for the TE (a) and TM (b) resonances.

The table below summarises some of the characteristics of the two resonances (errors are obtained using the 95% confidence intervals of the fitting):

Mode	λ_R (nm)	FWHM (nm)	Q	fit R^2	\mathbf{E}_{max} (sim.) (V/m)
TE	836.7 ± 0.1	8.6 ± 0.1	97.7	0.998	2.3×10^5
TM	840.0 ± 0.1	1.7 ± 0.1	496.2	0.940	6.9×10^5

4.3 Sensitivity measurements

A fundamental property of any sensing system is its sensitivity. For the family of sensors that are based on an optical resonance, the sensitivity is often quoted in nm/RIU (RIU: refractive index units). This is a measure of the size of resonance wavelength shift for a unit change in refractive index. Other figures of merit are possible, depending on how the resonance information is read-out. For example, if the resonance is interrogated by sweeping the angle of incidence at a fixed wavelength, as for a surface plasmon resonance sensor, a $^\circ$ /RIU sensitivity may be more appropriate [99]. Or if the relative intensity between two different resonant modes is monitored, dB/RIU might be quoted [100]. To measure the sensitivity here, the grating was exposed to glucose solutions of varying concentration while the resonance wavelength is monitored by recording the reflectance spectra. These

measurements were carried out using the reflection setup, with the flow channel connected to a syringe pump to pull liquid through the channel. By pulling the analyte instead of pushing, a negative pressure is exerted on the flow channel, thus minimising the chance of the PDMS bonds rupturing and leaking. The sensitivity is measured for both the TE and TM resonances in an effort to establish which performs better. Figure 4.3 shows the resonance wavelength shift ($\Delta\lambda_R$) as the glucose solutions are introduced. The refractive index of the solutions is obtained from [101], where a concentration of 25 % w/v (0.25 g/mL) yields a refractive index of 1.3629 and dilution with water then provides any refractive index down to 1.333.

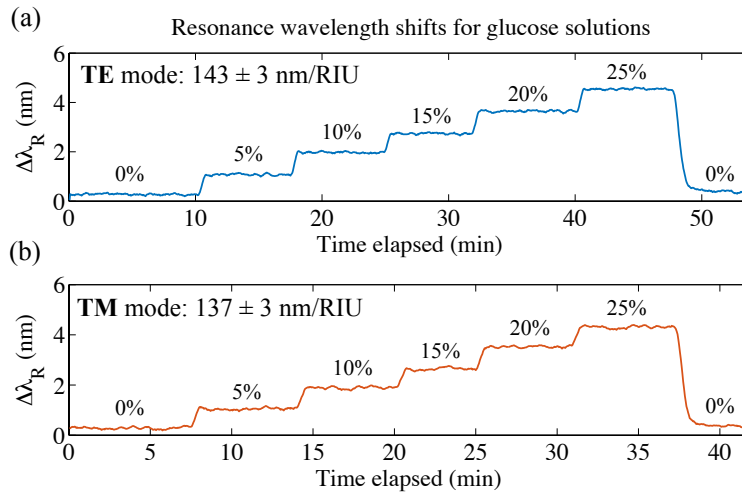


FIGURE 4.3: Resonance wavelength shift for the TE (a) and TM (b) resonances as different concentrations of glucose are introduced to the flow channel. Each concentration is indicated in % w/v.

From the resonance shifts plotted in figure 4.3, the sensitivity is measured by averaging the signal along the plateau for each glucose concentration, and then finding the height of each step. With Δn known, the value of nm/RIU can be obtained for each step. The results of this analysis are: 143 ± 3 nm/RIU for the TE resonance, while the TM resonance shows a value of 137 ± 3 nm/RIU. The errors here are the standard deviation in the average sensitivity for each step change.

In order to compare these measured values to those reported in the literature, please note a selection of reported sensitivities in the table shown in figure 4.4 [37, 102, 103, 104, 44, 105, 102, 106, 107, 108, 6, 109, 110, 111, 112, 113]. As well as the details of several grating-based devices, I include the sensitivities for some other resonant photonic devices as well, namely: photonic crystal cavities and microring resonators. The sensitivity of my sensor fits in well with values reported for other grating sensors. While slotted photonic crystal cavities may offer significantly higher sensitivities, they are often limited to performing a measurement that is not spatially-resolved, and cannot be used to generate a resonance

map, unlike gratings. Still, there are examples where individual photonic crystal cavities with distinct resonance wavelengths are arrayed on the same chip to provide some degree of spatial resolution, on the scale of a few μm [114]. The biggest advantage of grating surfaces compared to these other devices, however, is that in-plane fibre coupling is not required. This substantially simplifies the optical setup needed for sensor operation.

Structure type	Structure details	Bulk sensitivity (nm/RIU)	Assay	Reference
Resonant grating surfaces	My grating: Si_3N_4 on glass	134 - 143	Glucose solutions	n/a
	Low-index grating with TiO_2 coating	102	Isopropyl alcohol	[37]
	Porous glass grating with TiO_2 coating	140	Isopropyl alcohol	[102,103]
	Silicon oxynitride grating coupler	142	Isopropyl alcohol and NaCl solutions	[104]
	Low-index grating with Ta_2O_5 coating and additional SiO_2 “tie layer”	159 - 271	Polyelectrolyte layer deposition	[44]
	SiO_2 grating on silicon-on-insulator (SOI) waveguide	110	Simulations	[105]
	Low-index grating with TiO_2 coating	117 - 394	Simulations	[102]
Photonic crystal cavities	1D cavity in SOI	130	CaCl_2 solutions	[106]
	Slotted cavity in 2D crystal in SOI	415 - 600	Various	[107,108,6]
Microring resonators	Standard rings in SOI	70 - 141	Various	[109,110]
	Slotted rings in SOI and Si_3N_4	212 - 298	Various	[111-113]

FIGURE 4.4: Table comparing the bulk sensitivities of various resonant grating sensors in the literature, along with selected other photonic resonance sensors: microring resonators and photonic crystal cavities.

4.4 Limit of detection

Having measured the sensitivity of the resonance to bulk refractive index changes, the next and equally important figure of merit is the limit of detection (LOD). The LOD is determined here by measuring the noise in λ_R at a constant refractive index. The smallest observable shift is then deemed to be three times the standard deviation in λ_R : 3σ . During the measurement, I opted to use phosphate-buffered-saline (PBS) as the analyte that the sensor was exposed to. PBS is a very common buffer solution used throughout cell biology and immunology assays, so it is appropriate to use it for measuring the LOD instead of using a very pure analyte such as water; any deviations in optical density due to gradients in salt concentrations in the buffer will contribute to the noise. The main salt present is

sodium chloride (NaCl), at a concentration of 8 g/L, and additional salts are potassium chloride (KCl), sodium hydrogen phosphate (Na_2HPO_4) and potassium dihydrogen phosphate (KH_2PO_4), all at much lower concentrations than the NaCl. Additionally, since the assays I perform with my sensor are done with the analyte flowing through the flow channel, the noise is also measured while the PBS is pumped through the flow channel at the usual rate of approximately 20 $\mu\text{L}/\text{min}$. Although it is pumped at a constant rate, this fluid flow over the sensor may also contribute to the experimental noise.

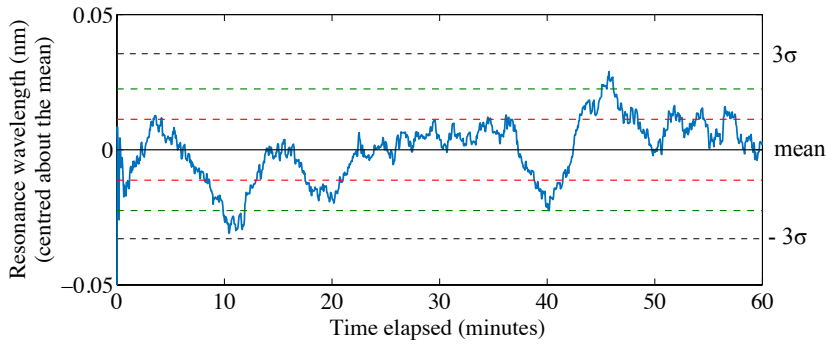


FIGURE 4.5: Resonance wavelength (centred about the mean) versus time, measured during the flow of PBS buffer solution.

Figure 4.5 shows a graph of resonance wavelength for PBS over a time period of 1 hour, where λ_R has been centred using the mean value (841.11 nm). The dashed red lines indicate $\pm 1\sigma$, and the dashed black lines indicate $\pm 3\sigma$, measured to be 33.8 pm. Multiplying this by the sensitivity of 143 nm/RIU, measured previously, I find the LOD to be 2.36×10^{-4} RIU. A low-pass (smoothing) filter is applied to the data, using a window of 3.75 minutes. This is acceptable since the rate of change of the real resonance signal is far slower than the noise frequency (typically a shift due to molecular binding, for example, occurs over a timeframe of several minutes). Therefore, the underlying signal is not changed appreciably by applying a low-pass filter on a minute-scale. There still remains a slowly-changing deviation in the signal, as evident from the three obvious dips at 10, 20 and 40 minutes in the graph of figure 4.5. The source of these deviations is unlikely to be due to mechanical vibrations or random noise, due to the timescale being a few minutes. It is plausible that the deviations are due to thermal fluctuations, or variations in the concentration of salts in the PBS as mentioned before.

Despite the considerable number of examples of resonant grating biosensors presented in the literature, relatively few report a LOD explicitly. Grego et al. [104] quote a refractive index LOD of 10^{-5} RIU, where a grating is used as a coupler into a waveguide, with the signal being observed as waveguide transmission. Still, Fan et al. [3] present an extensive review of various label-free optical biosensors, including LOD values. Here, the bulk LOD for different grating-based sensors varies from 10^{-3} and 10^{-5} RIU. Therefore, the LOD of

my sensor is in good agreement to other similar sensors in the field.

4.5 Sensor functionalisation

So far, the ability of the grating to detect changes in refractive index has been demonstrated by measuring the sensitivity and LOD with sugar solutions. However, for the sensor to have real value in biomedical applications, it must be able to detect a small quantity of a specific molecule, potentially from a mixture of hundreds of other biomolecules. To achieve such specificity, many biosensors utilise antibodies that can be fixed to the sensing surface (immobilised) in order to capture a target biomolecule. An antibody is a large protein molecule consisting of four peptide chains arranged in a Y-shape. At the open end of the Y, known as the "Fab region" (fragment, antigen-binding), there exist sites that only bind to a specific target molecule. The process of modifying a sensor to detect a specific antigen is known as "functionalisation", and there are a plethora of protocols to choose from to accomplish such antibody immobilisation. Moreover, functionalisation methods are not limited to antibodies, but can also be achieved using aptamers, for example, or self-assembled monolayers (SAMs) [115]. A discussion of different approaches to functionalisation is beyond the scope of this thesis, so I refer to [116, 117] for very comprehensive reviews of bio-functionalisation, and also to [118] for a brief but helpful overview.

4.5.1 EDC-NHS protocol

The functionalisation method I chose for my work is the EDC-NHS protocol [119], although glutaraldehyde and poly-lysine protocols were also tested, but these were abandoned after showing inferior performance. Figure 4.6 shows a detailed step-by-step illustration of the EDC-NHS protocol, to accompany the description in the following text.

After the introduction of hydroxyl groups (OH) via piranha cleaning, the sensor is silanised by exposure to (3-Aminopropyl)triethoxysilane (APTES). Silanisation takes place overnight in a solution of 1:19 APTES:ethanol, resulting in primary amine groups (NH_2) being attached to the surface of the sensor (see figure 4.6(f)). Following this is the reaction of the antibody with EDC (N-(3-Dimethylaminopropyl)-N-ethylcarbodiimide hydrochloride). Here, the carbodiimide molecule (EDC) reacts with the carboxyl group - ideally those at the base of the antibody molecule - to produce a urea ester. In principle, this antibody compound can now immediately react with the free amine groups on the sensor surface, but it is unstable in aqueous solution and rapidly hydrolyses before attaching to the sensor surface [119]. Therefore, sulfo-NHS (N-Hydroxysulfosuccinimide) is added to the reaction mixture, which aids the formation of a more stable compound that is still amine

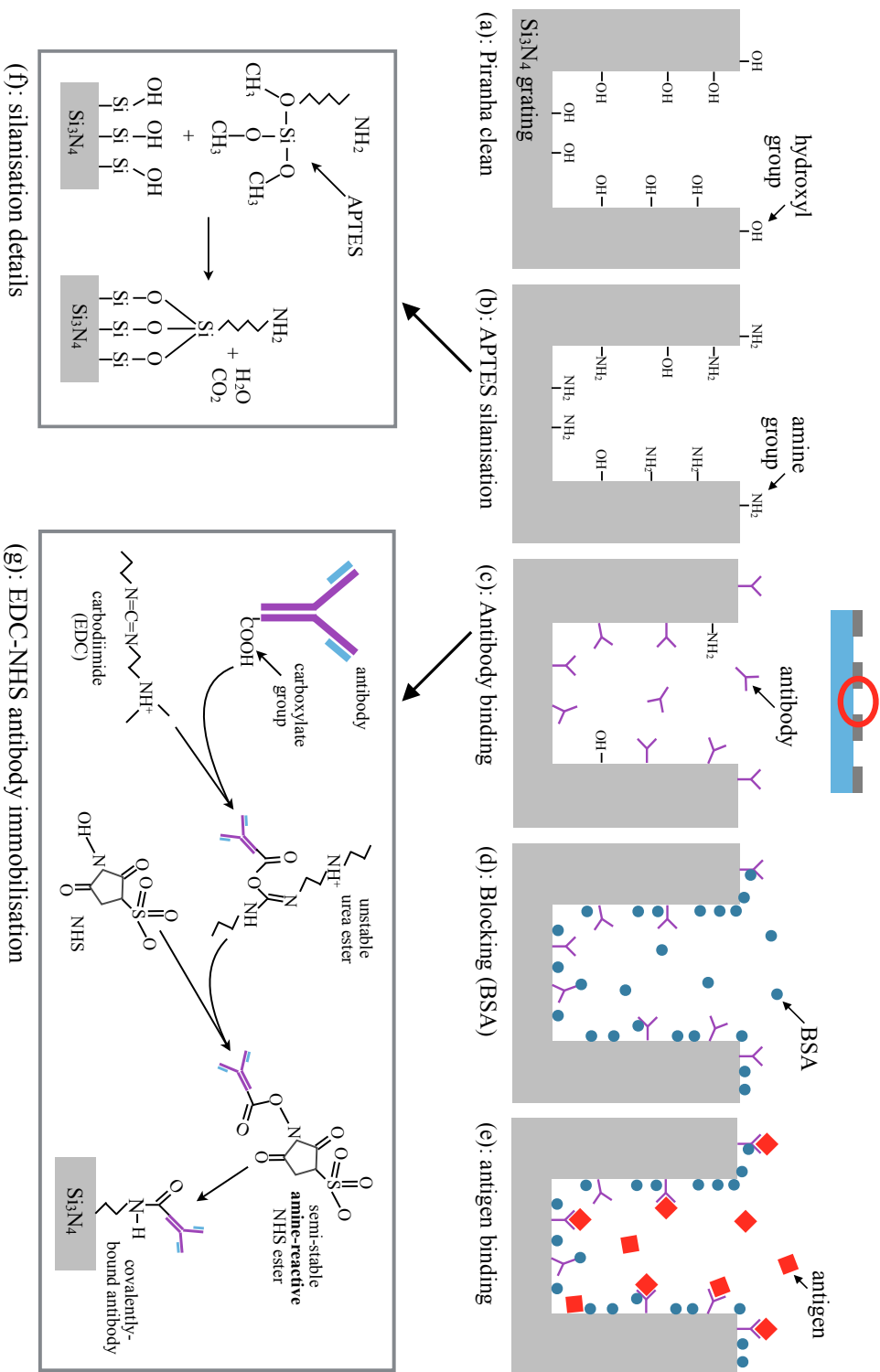


FIGURE 4.6: Step-by-step illustration of the EDC-NHS protocol for antibody immobilisation, with each step described in the text.

reactive. Consequently, the antibody can form an amide bond with the silanised sensor surface (figure 4.6(g)). It is desirable to have a large proportion of antibodies bound in the correct orientation for accepting the antigen, however, there may also be carboxyl groups at other sites on the antibody molecule that can bind to the sensor, making the orientation random and reducing the efficiency of the functionalisation. Step (d) in figure 4.6 shows the blocking stage of the assay. After antibody attachment, blocking is a crucial step in order to occupy any free (non-specific) binding sites on the surface. This is often done using bovine serum albumin (BSA), a serum protein that readily binds to any available sites, such as amine groups that have not been occupied by an antibody, for example.

I believe that there is considerable room for improvement concerning the protocol described above. There is some evidence, for example, that using EDC without the NHS may yield a better antibody immobilisation efficiency [120]. Optimising the pH and type of buffer solutions used in the reaction mixture at specific stages could also potentially improve the overall immobilisation efficiency [119]. An insightful experiment to determine the quality and coverage of the amine groups after the silanisation stage might follow that presented by Chen et al. [121]. Using an amine-reactive fluorescent marker that is allowed to bind to the available amine groups on the sensor, the amine coverage may be quantified via the fluorescence intensity. This experiment could be enhanced by tuning the resonance wavelength of the grating to match the excitation wavelength of the fluorophore, thereby boosting the fluorophore excitation in a similar way to that seen in [42]. Using this measurement as a figure of merit, different process conditions [122] for the silanisation step could be compared in an effort to optimise amine coverage, thereby increasing the number of available binding sites for the antibody.

4.6 Demonstration of binding of IgG

The final section of this chapter on sensing highlights the ability of the resonant grating to detect the binding of a biomolecule. The target molecule chosen is immunoglobulin G (IgG). IgG is also an antibody molecule, and is highly abundant in human blood, making up some 10-20% of all proteins contained in blood plasma [123]. IgG plays a crucial role in the immune system by binding to foreign pathogens to trigger various immune responses such as phagocytosis, whereby the IgG-labelled pathogen is recognised and engulfed by a macrophage (a white blood cell). Deficiencies of specific classes of IgG in humans can be linked to recurring respiratory tract infections [124], and increased susceptibility to bacterial infections [125], although the principal reason for using it here is that it provides an excellent testbed for measuring biosensor performance.

Drawing on the same experimental approach used for the sensitivity measurements at the beginning of this chapter, the resonance wavelength here is measured directly from the grating over an area of approximately 0.19 mm^2 ($1.9 \times 10^5 \text{ } \mu\text{m}^2$). The assay reagents are introduced to the sensor via a flow channel connected to a syringe pump. After acquiring the spectra, a Fano curve is fitted to the data and the precise resonance wavelength extracted from this fit. Plotting the resonance wavelength shift versus time gives the graph shown in figure 4.7. The various stages involved in the binding assay are indicated, and proceed as follows. First, a baseline measurement is made with the sensor exposed to PBS at a pH of 5.4. This is diluted 1:4 using PBS:H₂O because this is the same ratio as used for the EDC reaction next. The EDC and NHS are dissolved in PBS at pH 5.4 to concentrations of 8 mg/mL and 10 mg/mL, respectively. The antibody is then dissolved in water and added to the EDC-NHS mixture to yield a concentration of $50 \text{ } \mu\text{g/mL}$. The reaction is left for 20 minutes before being introduced to the sensor. A very clear binding curve is seen as the anti-IgG is immobilised on the sensor, saturating after ~ 100 minutes. After the anti-IgG immobilisation, the buffer is switched to PBS at pH 7.4. This causes an abrupt shift due to the refractive index mismatch between the anti-IgG solution (largely water) and PBS. There is also an indication of a reduction in resonance wavelength during the PBS stage, possibly due to poorly-bound antibodies being released. The next stage involves blocking the non-specific binding sites using BSA, as described in the previous section. A clear resonance shift occurs during the binding of BSA, however, this is seen to return to the original post-antibody level after PBS is flushed through, possibly suggesting that there are not many free sites, or that the BSA does not bind strongly. Next, PBS is flowed for around 1 hour to establish a baseline before introducing the antigen solutions. The antigen of anti-IgG is IgG, and it is dissolved in PBS to concentrations of $50 \text{ } \mu\text{g/mL}$, $5 \text{ } \mu\text{g/mL}$ and 500 ng/mL . The inset of figure 4.7 shows that all three concentrations cause a resonance wavelength shift. Because antigen binding is not permanent, there is always some amount of detachment from the sensor; antigen binding occurs in a dynamic equilibrium. Consequently, the different concentrations of IgG exhibit different binding curves. At low IgG concentration (500 ng/mL), there is no apparent saturation since it takes a long time to reach a dynamic equilibrium whereby the antigen binding rate equals the release rate. When the concentration is increased ($5 \text{ } \mu\text{g/mL}$), there is clear evidence of saturation after approximately 20 minutes. Further increasing the concentration ($50 \text{ } \mu\text{g/mL}$) incurs an even quicker saturation, taking around 5 minutes. The final stage in the assay is to verify that binding has been successful, and these shifts are not simply caused by IgG accumulating on the sensor without binding. To this end, PBS is again introduced, and since there is no visible negative shift, it is confirmed that IgG binding has been successful.

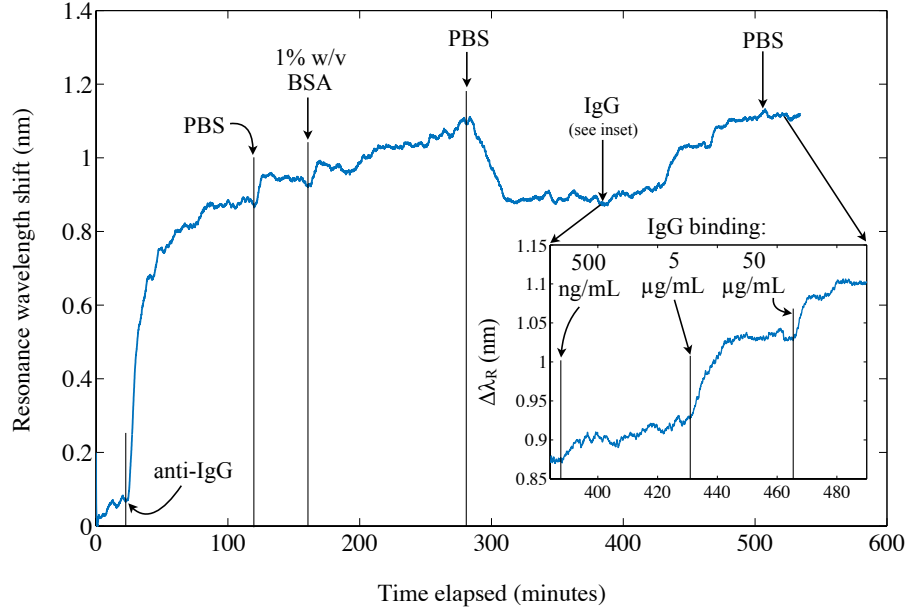


FIGURE 4.7: IgG binding assay. Plot shows resonance wavelength shift (nm) versus time elapsed, with the inset zoomed-in on the region of IgG binding. Each stage of the assay is indicated with a vertical black line and is described in detail in the text. The curve here has been smoothed using a window of 3.75 minutes.

4.7 Summary

In this chapter, I have demonstrated the sensing capabilities of the resonant grating, in particular in response to refractive index changes and biomolecular binding. Beginning by exploring some of the spectral characteristics of the two resonant modes supported by the Si_3N_4 grating, the resonance response to glucose solutions of different refractive indices is shown. The resonances both exhibit a bulk sensitivity of approximately 140 nm/RIU, in good agreement to other grating-based sensors found in the literature. Using this sensitivity, and by measuring the noise in resonance wavelength for a constant refractive index, the limit of detection is found to be 2.36×10^{-4} nm/RIU, again competitive with similar sensors in the field. After establishing the sensor performance with these control experiments, I focused on sensor functionalisation, describing in depth the NHS-EDC protocol for antibody immobilisation in order to detect a biomolecule. This was then tested with an IgG binding assay, where concentrations down to 500 ng/mL are confirmed to be within the detection range of my sensor.

Chapter 5

Imaging

The results on spatial resolution and its dependence on refractive index contrast presented in this chapter have been published in: G. J. Triggs, M. Fischer, D. Stellinga, M. G. Scullion, G. J. O. Evans, and T. F. Krauss, “Spatial Resolution and Refractive Index Contrast of Resonant Photonic Crystal Surfaces for Biosensing,” *IEEE Photonics J.*, vol. 7, no. 3, pp. 1–10, 2015. © IEEE 2015.

5.1 Introduction

In section 3.3, I introduced three different types of measurement that can be carried out using a resonant grating biosensor. This chapter focuses on the capabilities of using the grating as an imaging tool. While many other photonic biosensors, such as microring resonators, also employ a resonance that is sensitive to the external refractive index, they are used to perform a bulk measurement that lacks any spatial information. This was also the case for the results shown in the previous chapter, where the resonance shift was measured from the whole grating, resulting in a “bulk” refractive index measurement. However, since the grating resonance is excited with out-of-plane light, the resonance information may also be accessed by imaging the surface at different wavelengths. The result is the same highly-sensitive measurement of differences in refractive index, but it is now spatially-resolved and can thus be used as a contrast mechanism to produce an image, or a refractive index map. This resonance map can show, for example, cells living and growing on the sensor surface, or it can give a map of specific molecular binding at different sites on the surface. Such a spatially-resolved measurement of surface binding, without the use of fluorescent labels, is extremely valuable in biological research.

The resonance imaging concept is re-iterated in figure 5.1. Cells are used for illustration here, but any object that has a refractive index contrast with the surrounding medium may be imaged in this way. By acquiring a series of brightfield images at different illumination

wavelengths (using either of the setups shown in figure 3.6, for example), a hyperspectral image stack is obtained (fig. 5.1(b)). Typically, for the maps shown in this thesis, the wavelength is tuned in 0.2 nm steps across a range of 20 nm. Then, the spectral response for each pixel in the field of view can be read out, revealing the resonance wavelength for that pixel (figure 5.1(c)). These values are then used to create a resonance map, where the colour scale indicates λ_R , and thus highlights any refractive index variation across the surface (figure 5.1(d)).

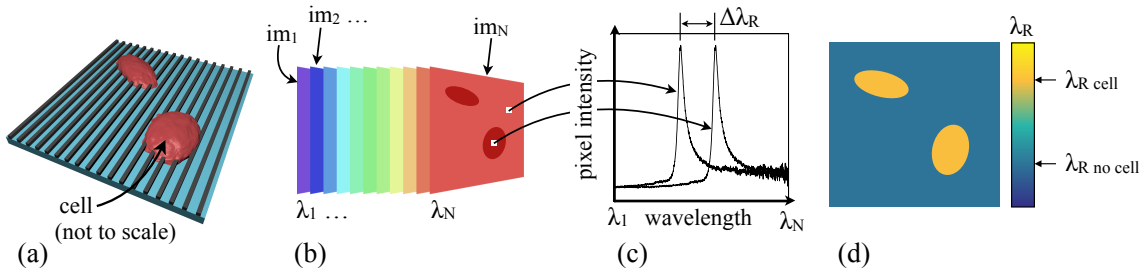


FIGURE 5.1: Measurement of a resonance map. (a) the grating with, for example, cells cultured on the surface; (b) brightfield images of the grating are collected as incident wavelength is swept from λ_1 to λ_N to produce a hyperspectral stack; (c) for each pixel in the field of view, the spectrum may be extracted by plotting pixel intensity vs position in the stack (i.e. wavelength); (d) by finding the wavelength where the pixel intensity is highest, for each pixel, the resonance map is obtained, where the colour bar indicates resonance wavelength.

Figure 5.2 shows two examples of resonance maps from gratings, measured using the setup shown in figure 3.6(b) of chapter 3. In (a), there are three gratings, each having a different period and therefore a different resonance wavelength. Meanwhile, (b) shows an example of a resonant grating that has a smoothly-changing period. This novel "chirped" grating design will be expanded upon in chapter 7. The resonance maps shown here exemplify the ability to delicately tune the grating resonance wavelength with electron beam lithography. The dislocations visible on the grating in (a) are caused by a slight error in writefield alignment during the e-beam exposure. Our system was particularly prone to these stitching errors at the time these images were acquired, and the issue has since been resolved. Nevertheless, they aptly demonstrate the high degree of sensitivity to tiny perturbations in the grating, as is the case when utilising them for biosensing. In particular, the horizontal dislocation has been measured with SEM to be just 180 nm - far below the optical diffraction limit, yet it clearly stands out in this low-magnification resonance map.

Before I move on to biological results to demonstrate the full potential of the resonant grating as a imaging tool, I first look at two important characteristics of the sensor in terms of its imaging capability. Firstly, the penetration depth, or sensing depth, is measured: How close to the grating does a cell need to be before it is detected? Secondly, the spatial resolution is measured using a novel technique that facilitates a study into how the resolution depends on refractive index *contrast*. Since these two topics are comprehensive,

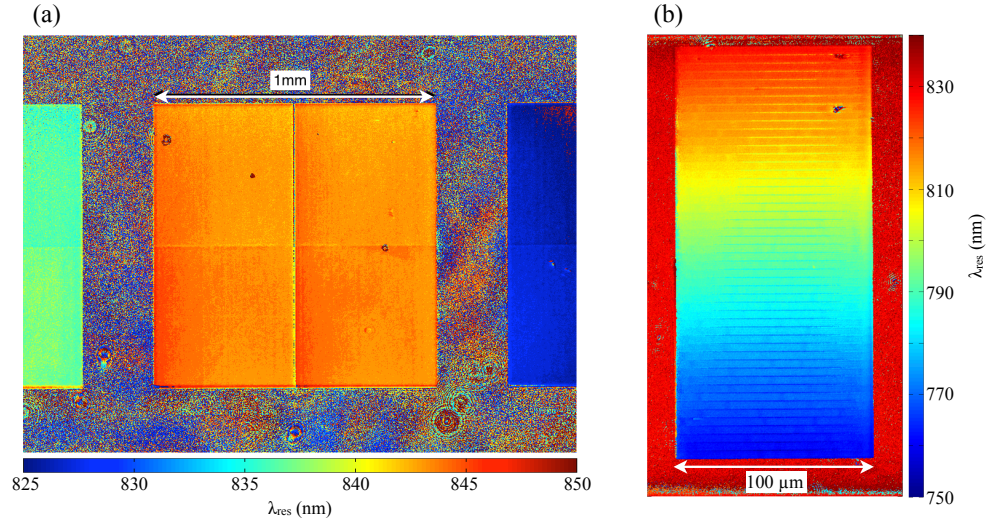


FIGURE 5.2: Resonance maps of gratings with (a) a fixed resonance wavelength, and (b) a spatially-varied resonance wavelength. In (a), the central grating has $\lambda_{res} \approx 848$ nm, while those on the left and right have $\lambda_{res} \approx 836$ nm and $\lambda_{res} \approx 828$ nm, respectively. The dislocations are writefield stitching errors, with the horizontal one measured at just 180 nm. The slight gradient across each writefield is caused by very small fabrication variation. The grating in (b) is composed of individual strips, each having a different period.

they make up the rest of this chapter, and I devote the following chapter (chapter 5) to biological measurements that combine the sensing and imaging aspects of the sensor.

5.2 Penetration depth

In a similar fashion to other photonic biosensors that employ a resonance, the resonant mode supported by the gratings in my work has a strong field overlap, or "evanescent tail", that extends outside the grating layer and into the sensing region. It is this mode overlap that links a change in optical density in the vicinity of the grating to a measurable change in the resonance wavelength. The penetration depth of the evanescent field defines the maximum detection distance of the sensor and is typically a few hundreds of nm [126] for optical sensors. For a resonant grating biosensor or a photonic crystal, the field within the grooves or holes also plays an important role in detecting changes in refractive index, in addition to the evanescent field which extends away from the grating. Currently, there is very limited study on the penetration depth of resonant grating biosensors in the literature. The best example is by Cunningham et al. [44], where polyelectrolyte layers of known thickness are deposited sequentially on top of a resonant grating to probe the sensitivity as a function of distance from the grating. By changing the grating structure to tune where the resonant field is concentrated, the surface sensitivity may also be enhanced. However, the main focus is the enhancement of surface sensitivity. It is reasonable to assume that different grating structures and resonant modes provide different penetration depths, so it is important to characterise this quantity for any particular sensor. Measuring penetration

depth is a challenging measurement to perform, requiring, for example, the deposition of layers of well-known thickness and refractive index - properties that are difficult to ascertain accurately if they are both unknown. Nevertheless, below I demonstrate a simple alternative experiment to directly measure the sensing depth of my resonant grating.

5.2.1 Measurement idea

A convex glass lens is placed directly on top of the resonant grating (figure 5.3(a)), and the resonance map is obtained (figure 5.3(b)). At the centre of the lens, the glass is in direct contact with the grating, causing the largest shift in resonance wavelength (~ 18 nm for this case). When moving radially away from the centre, the separation between the lens and the grating becomes greater and so the resonance wavelength decreases until the lens is no longer detected. At this point, it is too far from the sensor surface to influence the resonant mode, and the resonance wavelength has returned to the background value. The surrounding liquid here is water, and the lenses are spherical N-BK7 glass lenses of refractive index $n = 1.51$. (Thorlabs LSB04).

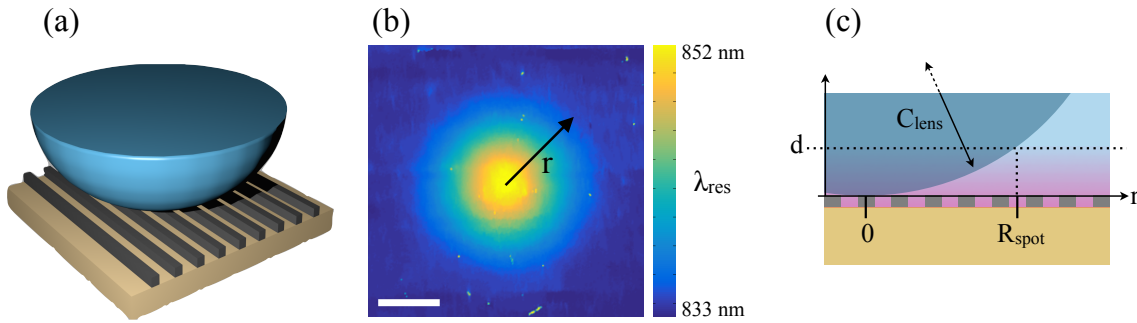


FIGURE 5.3: (a) Representation of a lens on top of the grating (not to scale); (b) Resonance map of a lens. Scale bar = $250 \mu\text{m}$. The black arrow indicates the radial distance (r) away from the centre of the lens; (c) Geometry used in the calculations described in the text. Pink indicates the evanescent field, which extends vertically to d .

Purely geometrically (figure 5.3(c)), the radius of the spot in the resonance map (R_{spot}) is related to both the radius of curvature of the lens (C_{lens}), and the sensing depth (d) via equation 5.1. Since the curvature of the lens is known to a high degree of accuracy, the sensing depth can be calculated from measurements of R_{spot} using the rearranged equation 5.2. By repeating the measurement with lenses of different curvature radii (focal lengths), the estimation of d becomes more accurate.

$$R_{spot}(d, C_{lens}) = \sqrt{2 \cdot d \cdot C_{lens} - d^2} \quad (5.1)$$

$$d(R_{spot}, C_{lens}) = C_{lens} - \sqrt{C_{lens}^2 - R_{spot}^2} \quad (5.2)$$

5.2.2 Results

After collecting resonance maps for various lens curvatures, the radial profiles of pixel grey value are obtained using ImageJ. Two such profiles from different lenses are shown in figure 5.4(a), where each profile is averaged through 360° about the centre of the resonance map. R_{spot} is obtained from these profiles as the point at which the pixel grey value drops to within 10% of the background level (dashed line in figure 5.4(a)). A graph can then be plotted showing lens curvature C_{lens} vs. measured spot size R_{spot} (figure 5.4(b)). Fitting the curve of equation 5.1 to this data gives a graphical estimation of the sensing depth to be $d = 183nm \pm 14nm$ ($R^2 = 0.97$), as shown by the red line in figure 5.4(b). Alternatively, solving equation 5.2 for each lens-spot combination gives an average depth of $186nm$ and a standard deviation of $29nm$.

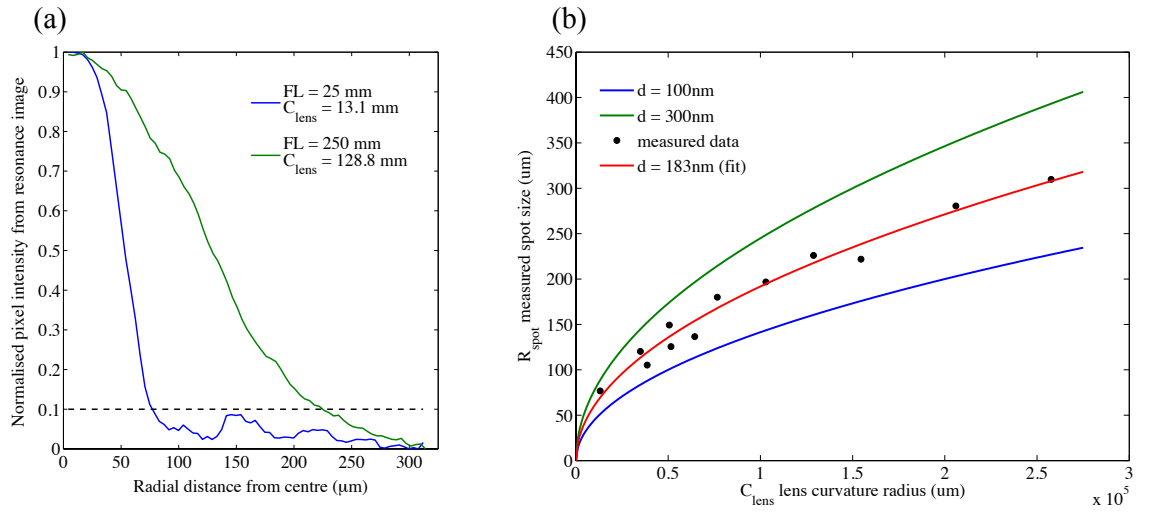


FIGURE 5.4: (a) Radial profiles from the resonance images of two different lenses vs. distance from the centre of the lens. Dashed line shows 10%; (b) Lens curvature radius (C_{lens}) vs. resonance spot size (R_{spot}). The green and blue lines represent the theoretical spot sizes for specific sensing depths using eqn. 5.1, while the red line is the best fit to the data.

The (broader) TE resonant mode was used in the above measurements, but repeating the measurement for the (narrower) TM resonance that this grating also supports yields a slightly longer sensing depth of $d = 220nm \pm 13nm$ (goodness-of-fit: $R^2 = 0.98$). This difference can be related to differences in the evanescent electric fields that penetrate out of the grating layer. As discussed in chapter 2, to support a guided-mode resonance, the grating layer must have a higher overall refractive index than the surrounding media, enabling it to operate as a waveguiding layer. Like a conventional waveguide, the effective refractive index of the mode is an indication of its penetration into the surrounding regions. Here, the refractive index of the grating is approximated using the effective index expressions shown in equations 2.10 in chapter 2, for the TE and TM resonances respectively. By inserting values that correspond to the grating used here into these expressions, I find $n_{eff,TE} = 1.855$, while $n_{eff,TM} = 1.746$. The values used are $FF = 0.75$, $n_H = 2.00$, $n_L = 1.333$,

corresponding to the Si_3N_4 grating with water filling the grooves. The fact that the TM mode has a lower n_{eff} indicates that it has a larger overlap with the medium surrounding the grating layer, as is indeed the case experimentally. This can be seen analytically, by expressing the electric field in the medium surrounding a conventional waveguide as a decaying exponential:

$$\mathbf{E}(z) = E_0 e^{-pz}, \quad \text{where } p = k_0 \sqrt{n_{eff}^2 - n_{sur}^2}, \quad (5.3)$$

where z is the distance away from the waveguide. The decay constant p is a function of n_{eff} , and the decay length can be obtained from $1/p$. In this formulation, the decay length of the TE mode is 104 nm while for the TM mode it is 119 nm. The ratio between these two values (0.87) is in good agreement with the ratio from my experimental results (0.83), especially when the experimental uncertainties are taken into account. The reason that the analytical value of penetration depth is lower than my measured value is due to the fact that I chose the point at which the resonance wavelength drops to 10%, and not the value of $1/e$, i.e. 37%, as is the case in the analytical treatment. Repeating the calculation for 10% ($\ln(10)/p$ instead of $\ln(e)/p$) yields values of 239 nm and 273 nm for TE and TM, respectively. These values are higher than the measured values (as might be expected for a "perfect" analytical system), and below I discuss potential limitations of the measurement before introducing a simulation in an effort to back up my results.

Although the measurements are in agreement with what is predicted from the geometrical model (they follow equation 5.1 closely), it is important to discuss potential limitations. Perhaps the most obvious is the assumption that the lens is sitting directly on top of the surface and that there is no water gap. A second query is: how will the sensing depth be affected by different refractive indices in the region above the grating? The lenses used here have a relatively high index of 1.51 ([127, 128]) compared to most biological material, so how do the results compare when a more relevant index of, say, 1.38 is used? According to the analytical expression for field decay shown in equation 5.3, decreasing n_{sur} causes p to increase, resulting in a shorter penetration length. Therefore, it is sensible to assume that the values measured here using the glass lenses represent an upper limit to penetration depth in the context of biosensing where the refractive indices are unlikely to exceed $n = 1.51$. To further study these points, I have implemented RCWA simulations to model the resonance shift in the presence of the glass lens, which is shown next.

5.2.3 RCWA model of sensing depth

Firstly, I simulate the grating being surrounded by water to establish the background resonance wavelength before introducing a flat block of material with a refractive index of 1.51 to mimic the lenses used in the experiments. Here, the geometry of the lens is unimportant

and I focus solely on the resonance wavelength shift caused by the presence of the glass block. The block is gradually moved towards the grating, and the resulting resonance shift is shown in figure 5.5(a) versus the grating-block separation distance (t_{sep}). This is done for both the TE and TM resonances: blue and red curves, respectively. This data reveals that the TE mode is influenced more within the grooves of the grating ($t_{sep} < 150nm$) while the TM mode is affected more in the region immediately above the grating ($t_{sep} > 150nm$). The slopes of these curves can be thought of as the sensitivity as a function of distance from the grating. This is also evident from the electric field profiles shown in figure 4.2 (chapter 4). These effects compensate for each other somewhat, so the magnitude of the resonance shift at $t_{sep} = 0nm$ is very similar for both modes. This is in agreement with the fact that both resonances exhibit roughly the same overall sensitivity (as shown in figure 4.3 (chapter 4). Moreover, there is an obvious indication of a slightly longer penetration depth for the TM mode, in agreement with the measured values of d shown in the previous section ($d_{TE} = 183nm$, $d_{TM} = 220nm$), and with the analytical calculation on penetration length shown above.

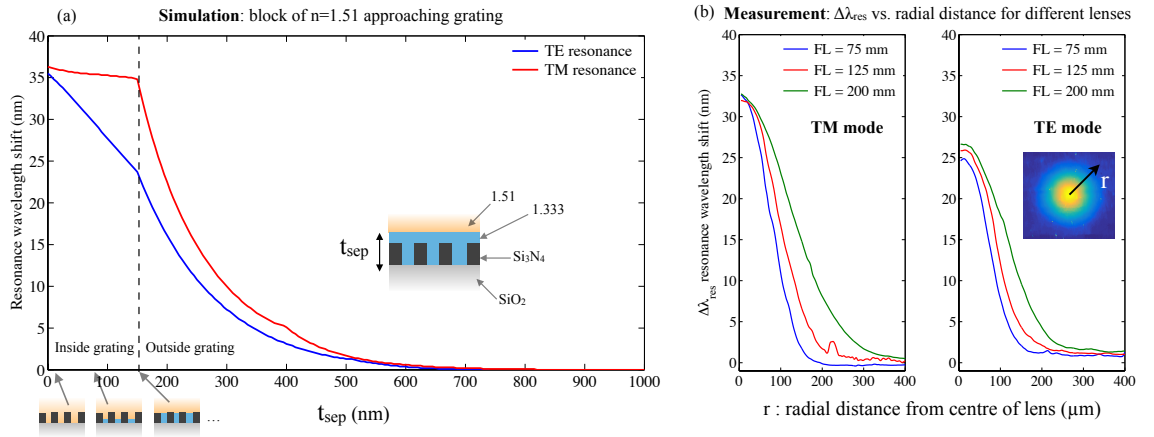


FIGURE 5.5: (a) RCWA simulation showing λ_{res} changing as a block of N-BK7 glass is brought into contact with the resonant grating. (b) Measured λ_{res} from resonance image profiles for different lens focal lengths (curvatures), showing TE and TM resonances.

In the experiment, the lens cannot move any closer than $t_{sep} = 150nm$ so $\Delta\lambda_{res}$ at the centre of the lens (assuming no water separation layer) should be approximately $24nm$ and $35nm$ for the TE and TM modes respectively (intercepts with the dashed line in figure 5.5(a)). Figure 5.5(b) shows the measured radial profiles from resonance images of lenses with different curvatures for both TE and TM resonances. These results agree well with the values obtained in the RCWA model, and provide evidence that there is no water gap, or it is negligible. A water layer would noticeably reduce the resonance wavelength measured at the centre of the lens (i.e. at $r = 0$), resulting in a large difference between measurement and simulation. When doing the experiments, the lens was gently pressed into contact with the grating to help eliminate any water layer between the lens and the grating. I also used

this model to look at the effect of reducing the refractive index of the block from glass (1.51) to a more biologically-relevant value of 1.38. By taking the penetration depth to be the value of t_{sep} where $\Delta\lambda_{res}$ has fallen to within 10% of the background level, I find a reduction in penetration of 17% for $n_{block} = 1.38$ compared to $n_{block} = 1.51$. This is consistent with the evanescent mode having a longer decay length, and therefore a longer penetration depth, into a material of higher refractive index, since the mode is less well-confined to the high-index grating layer.

5.3 Spatial resolution in X and Y directions

Just like for any other imaging technique, a fundamental measure of the imaging capability of a resonant grating biosensor is its spatial resolution. Although the spatial resolution is limited by the resolution of the optical system (ultimately down to the diffraction limit of $d = 0.61\lambda/\text{NA}$), the actual resolution of the resonance maps is larger than this limit, and an understanding of what governs the resolution is not trivial. An excellent study on the spatial resolution of a resonant grating surface is presented only by Block et al. [47], where a resolution test pattern was *etched* into the grating in order to provide the resonance shift needed to create contrast in the resonance map. The authors report an asymmetric spatial resolution, as expected due to the asymmetry of the grating in the X and Y directions. While this is an elegant way to create the contrast in the resonance image, it is not faithful to what happens when the sensor is used to measure real biological samples where refractive index differences alone provide the imaging contrast.

In light of this, I have developed a new method for measuring spatial resolution, again using a test pattern but here it is fabricated in electron-beam resist *on top* of the resonant grating. Not only is this approach more consistent with real biosensor operation, where resonance shifts are caused by refractive index contrast, it also allows me to investigate the relationship between spatial resolution and refractive index *contrast*; something not seen in the literature before.

The next sections on spatial resolution are broken down in the following way: Firstly, I present details on the fabrication of the resolution test patterns, before using these to measure the spatial resolution in the X and Y directions. This is followed by a discussion then the development of a theoretical model to describe the experimental findings. This model is then tested experimentally using a 2-dimensionally patterned grating - a study that is also not found in the literature. After this, section 5.4 deals with the dependence of the spatial resolution on refractive index contrast, first by presenting experimental results and then by supplementing these with modelling.

5.3.1 Fabricating the resolution test patterns

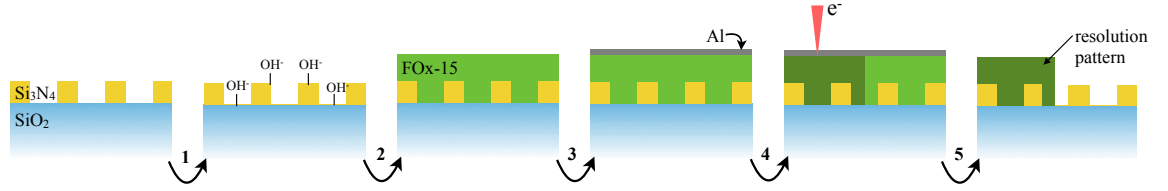


FIGURE 5.6: Fabrication of resolution test pattern on top of a resonant grating. Step 1: The Si_3N_4 grating is cleaned using piranha solution. Step 2: FOx-15 resist is spin-coated on top of the grating. Step 3: an Aluminium charge dissipation layer is thermally evaporated on top of the resist. Step 4: Electron-beam exposure to cross-link the resist polymer and render it insoluble. Step 5: Development to remove the unexposed resist regions.

The resolution test pattern follows a similar design to the commonly-used USAF test pattern. Fabrication of the pattern follows the same process shown in chapter 3, but beginning with the resonant grating as the substrate, instead of unpatterned Si_3N_4 , and not proceeding beyond the development stage. The process is reiterated in figure 5.6, where the end product is a resonant grating, on top of which are the exposed resist regions that make up the resolution test pattern. The resist used for the test pattern is "flowable oxide" FOx-15 (Dow Corning), also known as HSQ (hydrogen silsesquioxane) in the electron-beam lithography community. The main solvent in the resist is methyl isobutyl ketone (MIBK), and this may be added to reduce the viscosity to produce films of different thicknesses. The primary reason for using FOx here is the low refractive index (between 1.35 and 1.5), compared to other common resists such as SU-8 or PMMA (MicroChem). This is beneficial during the refractive index contrast measurements, which are discussed in the next section. I spin-coat FOx (diluted with MIBK at a ratio of 1:2), on top of the grating at a speed of 6000 RPM to achieve a film thickness of approximately 100 nm (measured using atomic force microscopy). The electron dose used is $600\mu\text{C}/\text{cm}^2$, which is relatively high in comparison to other resists. However, since FOx is a negative tone electron-beam resist, only the pattern itself needs to be exposed. So, despite the high electron dose needed, the patterning time is very fast. Development of FOx is with solvent MF-319, which dissolves the un-exposed areas, followed by a rinse in isopropanol and drying with nitrogen.

This fabrication process is followed to produce a resolution test pattern on top of the resonant grating, where the pattern is arranged in three different formats, as illustrated in figure 5.7. Throughout the remainder of this chapter, I refer to the "X-direction" as being perpendicular to the grating ridges, i.e. in line with the grating vector (\mathbf{G}), as indicated in figure 5.7(a), while the "Y-direction" is parallel to the grating ridges. \mathbf{G} is also included in other figures throughout this chapter to indicate the orientation of the grating in relation to the resolution patterns. Figure 5.7(a) shows a large block of resist, which enables qualitative measurements of the change in resonance wavelength across the edge of the block in the X and Y directions. Meanwhile, to obtain a quantitative measurement

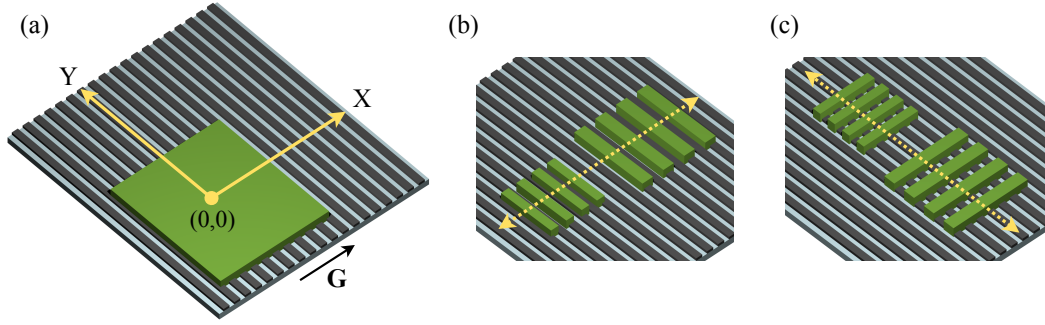


FIGURE 5.7: Illustrations of the arrangement of resolution test patterns, fabricated in resist on top of the resonant grating. (a) A large square block for measuring the difference in resonance wavelength across the edges in the X and Y directions; (b) A ruler pattern, aligned to measure the spatial resolution in the X direction and (c) the Y direction, as indicated by the dashed yellow arrows.

of the spatial resolution, I employ a "ruler" structure as shown in figures 5.7(b,c). These patterns consist of multiple groups of four rectangular bars of a specific width and spacing (only two such groups are shown in the illustration), where the bar width and inter-bar spacing used for each group is varied along the resonant grating. By aligning the bars in two different orientations with respect to \mathbf{G} , the spatial resolution along X (5.7(b)) and Y (5.7(c)) can be measured.

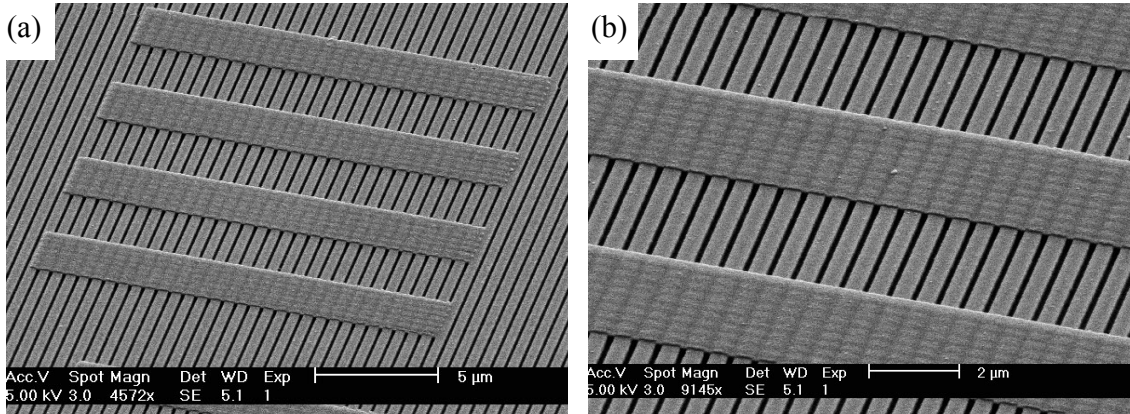


FIGURE 5.8: (a) SEM image of a group of four blocks of the FOx resist pattern, fabricated on top of the resonant Si_3N_4 grating. This orientation is used to measure spatial resolution in the Y direction, perpendicular to \mathbf{G} ; (b) Zoomed-in view.

Figure 5.8(a,b) shows SEM images of one group of four bars from the ruler resolution test pattern, fabricated on top of the resonant grating. The SEM images clearly indicate that the patterns are well-defined and that there is no residual resist between the bars - something that would significantly affect the spatial resolution measurements. There is also evidence that the grating pattern is transferred somewhat into the resist, meaning that the top of the resist blocks are not flat. Indeed, the planarisation of layers deposited on top of patterned substrates is a significant challenge in nanofabrication [83]. In order to

investigate this in more detail, and to measure the thickness of the resolution test patterns, atomic-force microscopy (AFM) measurements were performed, with results shown in figure 5.9. The thickness of the FOx patterns is measured to be ~ 100 nm, and the deviation on the top surface due to the influence of the underlying grating is $\sim \pm 10$ nm. I note that the AFM scan speed used here prevents the full depth of the Si_3N_4 grating grooves from being resolved, so they appear only as a small corrugation.

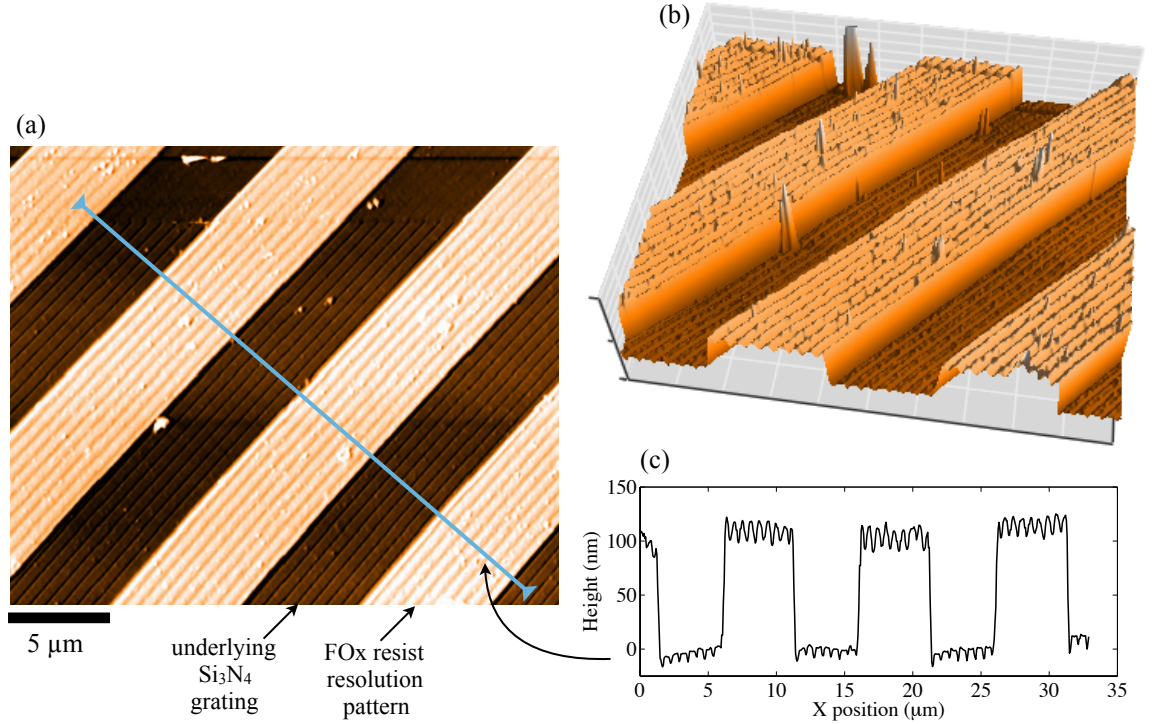


FIGURE 5.9: (a) Colour map from the AFM scan over four bars of FOx resist on top of the resonant Si_3N_4 grating; (b) 3D version of the AFM scan; (c) Height profile along the blue line indicated in (a). AFM scans obtained with help from José Juan Colás, Department of Electronics, University of York.

5.3.2 Influence of resist on resonance wavelength

To determine how the FOx resist layer affects the resonance wavelength, I first analyse the resonance map of a simple block of resist as shown in figure 5.7(a). The higher index of the resist gives rise to a localised shift in the resonance wavelength. Figure 5.10(a) shows this shift spectrally, where the averaged reflectance spectra are extracted from the regions indicated on the resonance map shown in figure 5.10(b). A 3-dimensional view of the resonance map is shown in 5.10(c). The resist causes a shift in λ_R of approximately 10 nm from the non-covered grating region.

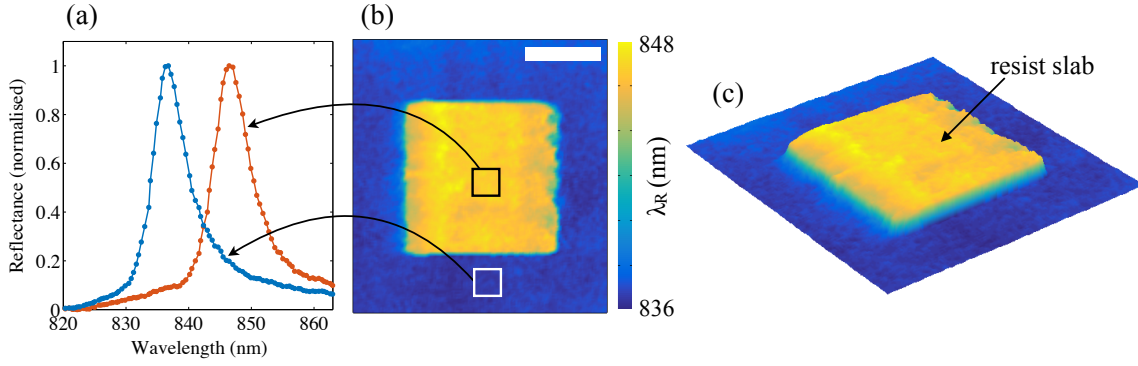


FIGURE 5.10: (a) Average reflectance spectra taken from the regions indicated on the resonance map in b; (b) Resonance map of a block of resist situated on the resonant surface. Scale bar = $10\ \mu\text{m}$, colour bar indicates resonance wavelength in nm; (c) The same map shown in three dimensions as a surface. Here, water is the surrounding medium.

5.3.3 Results: spatial resolution in X and Y directions

To investigate the spatial resolution along X and Y, I now turn to resonance maps of the "ruler" resist patterns, like those in figure 5.7(b,c). Figure 5.11(a) shows a resonance map of a portion of the resist pattern, with bar groups oriented in both the X and Y directions. Here, water is used as the liquid surrounding the resist bars, and all images are obtained using a 20x objective lens with $\text{NA} = 0.46$. Qualitatively, there is a clear difference in spatial resolution along X and Y, with the resolution being better in Y, i.e. perpendicular to \mathbf{G} . This agrees with the results reported by Block et. al. [47], where the resolution pattern was etched into the grating. The root of this asymmetrical resolution is discussed next, but first, quantitative measurements of the spatial resolution limit are done using the resonance maps of the ruler pattern.

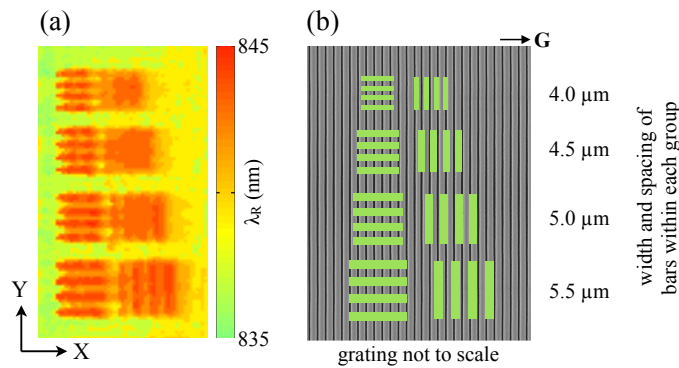


FIGURE 5.11: (a) Resonance map of selected groups of bars from the resolution test pattern. Colour bar indicates the resonance wavelength in nm; (b); illustration of the orientation of the resist bars with respect to the grating (not to scale). Width and spacing of the bars decreases in the Y direction, as specified at the right.

Measured profiles from the resonance maps, through the groups of resist bars oriented along the X and Y directions, are shown in figures 5.12(a) and 5.12(b), respectively. I define the resolution limit to be the point at which the difference in resonance wavelength

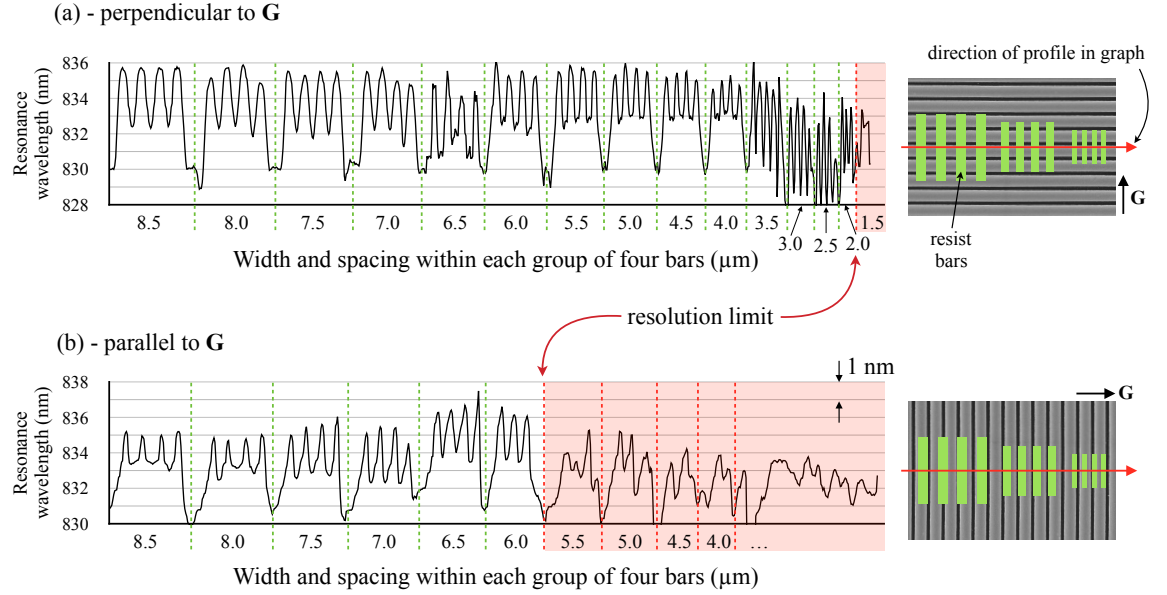


FIGURE 5.12: Profiles measured from the resonance images of the ruler resist pattern, with groups of bars orientated perpendicular to (a), and parallel to (b) the grating vector (\mathbf{G}). Images on the right indicate the orientation of the patterns and grating (not to scale) with respect to the measurement direction. The pink shaded regions indicate the point at which the individual bars can no longer be distinguished. [© IEEE 2015]

between the individual blocks drops below $1/e$ of the "bulk" difference between each group of four blocks. This resolution limit is indicated by the pink shaded areas on the graphs. Using this definition, I measure a resolution limit of $2 \mu\text{m} \pm 0.5 \mu\text{m}$ for the profile in figure 5.12(a) (perpendicular to \mathbf{G}), while it is $6 \mu\text{m} \pm 0.5 \mu\text{m}$ in figure 5.12(b) (parallel to \mathbf{G}). The errors here are taken to be \pm the smallest change in bar width/spacing.

5.3.4 Discussion on spatial resolution

So far, I have experimentally demonstrated that the spatial resolution of the resonant grating sensor is higher along Y (perpendicular to \mathbf{G}) than it is along X. Ultimately, the resolution depends on the propagation length of the resonant mode in the grating layer, and it is fundamentally limited by the usual diffraction limit ($0.61\lambda/\text{NA}$). The effect of the grating (as is discussed below) means that the resolution measured here is always above this diffraction limit. Since the grating used here is periodic only in one direction (X), incident light is not coupled into a guided mode propagating in the Y direction. Instead, it is coupled into a guided mode that oscillates resonantly in the X direction. This idea can be better understood by considering the \mathbf{k} -vectors involved, as shown in figure 5.13(a). The incident light, which only has a k_z component, receives a k_x component from the grating vector via diffraction, since \mathbf{G} is aligned solely along X. Thus, the propagation is directed along the X direction but not along Y. This lateral propagation in X effectively blurs out the resonance information in the X direction, reducing the spatial resolution. This is an

interesting and perhaps counter-intuitive result; The spatial resolution is higher in the Y direction, even though lateral propagation in the X direction is required for the resonance to occur in the first place [129]. In order to check the validity of this model, the spatial resolution of a 2D periodic grating is measured and discussed next.

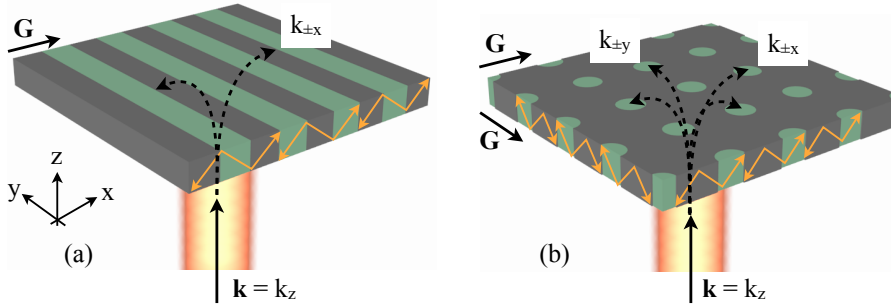


FIGURE 5.13: Illustration of incident light coupling into a guided-mode resonance for a 1D grating (a) and a 2D grating (b). [© IEEE 2015]

It should be mentioned here that the in-plane propagation length (and thus spatial resolution) is also related to the spectral linewidth of the resonance. In the case of a narrow linewidth, the mode has a long propagation length in the grating and experiences reflections from more grating interfaces. This is analogous to increasing the number of layers in a distributed Bragg reflector (DBR) to provide sharper reflectance band edges. Consequently, using a spectrally-narrow resonance for imaging is detrimental to the spatial resolution, as demonstrated in [47]. Unfortunately, a narrower resonance intrinsically gives more accuracy when reading the peak wavelength, so a compromise must be made between spatial and spectral resolution. For this reason, all the image-based sensing presented here was carried out using the broader TE resonance, while the sensing experiments presented in the previous chapter generally utilised the narrow TM resonance for greater spectral precision. Additionally, an alternative method for measuring the spatial resolution might be to differentiate the profile measured across a step change in refractive index, such as over the edge of the resist slab shown in figure 5.10. The differentiated profile would show as a single Gaussian peak, and the width of this would indicate the spatial resolution.

5.3.5 Extension to a 2D grating

To extend the model developed above from a 1D periodic grating to a 2D periodic grating (i.e. an array of holes), I again examine the \mathbf{k} -vectors involved, as shown in figure 5.13(b). In the same fashion as the 1D grating, the incident light receives additional \mathbf{k} components due to the grating vectors \mathbf{G}_x and \mathbf{G}_y , thereby directing propagation into *both* the X and Y directions via diffraction. If the model is correct, it follows that the spatial resolution for this structure should be *equal* in the X and Y directions, and not asymmetric like the

case of a 1D grating, since the resonant mode propagates equally along X and Y. However, this assumes that the incident light is *unpolarised*. For the case of polarised light (if the incident \mathbf{E} vector is aligned solely along Y, for example), then diffraction causes a change in orientation of \mathbf{E} for the mode propagating in the Y direction, while the orientation of \mathbf{E} for the mode propagating in the X direction is unaffected by this diffraction. Consequently, the excitation of the guided mode is different in the X and Y directions, which again leads to a difference in spatial resolution as is the case for a 1D grating. To investigate this behaviour experimentally, I used a 2D grating in Si_3N_4 (figure 5.14(a)), with a very similar structure to the usual 1D grating in my work. This is a square array of holes, with a period $a = 540\text{nm}$ and a hole radius $r = 0.204a$, which supports a guided-mode resonance at a wavelength approximately the same as that of the 1D grating ($\sim 840\text{nm}$). As before, the resolution test pattern was fabricated on top of this structure, and resonance maps were measured.

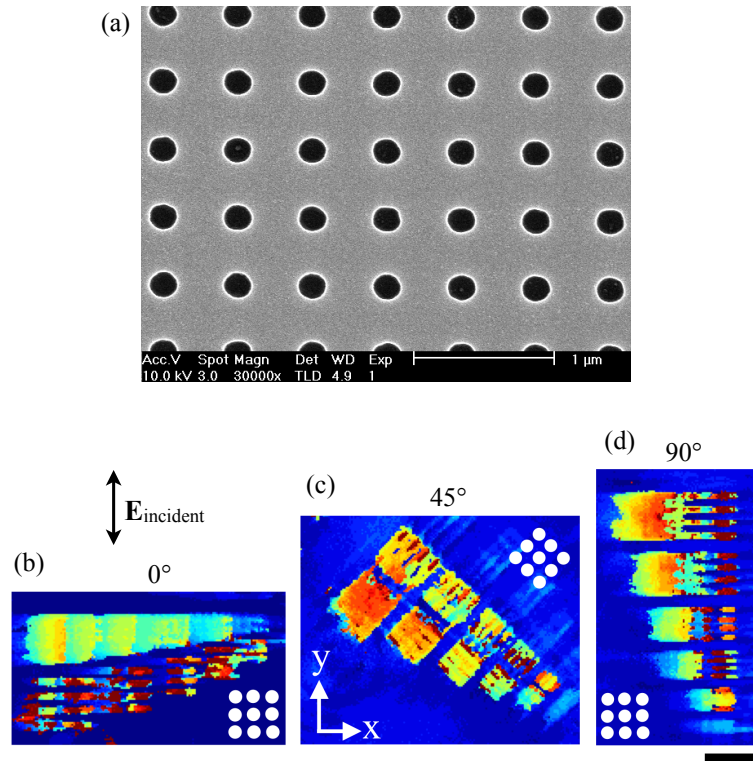


FIGURE 5.14: (a) SEM image of the 2D grating employed for measuring the spatial resolution. Grating fabrication and SEM imaging done by Dr M. Fischer, Department of Physics, University of York. Resonance maps of the resist pattern on top of the 2D grating with the illumination polarisation indicated by \mathbf{E} , and being the same for all images. The grating is oriented at (a) 0° , (b) 45° , and (c) 90° with respect to \mathbf{E} , as indicated by the white circles inset on each map. The scale bar (bottom right) is $25\mu\text{m}$. [© IEEE 2015]

Figures 5.14(b,c,d) show the maps for the cases where the incident light is polarised with \mathbf{E} aligned in the vertical direction, while the 2D grating is rotated with respect to this incident polarisation. The case where the grating is oriented at 45° (figure 5.14(c)) is equivalent to the incident light being unpolarised, because \mathbf{E} may be represented as a vector sum of

equal terms in E_x and E_y . For this case, the spatial resolution in the X and Y directions is indeed equal, in agreement with my model where the resonant modes propagating in X and Y are equally excited. The resolution is thus not high enough to fully distinguish the individual bars in any direction. However, if the grating is oriented at either 0° (figure 5.14(b)) or 90° (figure 5.14(d)) to the incident \mathbf{E} , the spatial resolution returns to being asymmetric like the case of a 1D grating. Here, there is a clear difference in resolution, with the bars being easily distinguished in the Y direction but not in X.

5.4 Dependence of spatial resolution on index contrast

In addition to directly probing the spatial resolution of the grating sensor in the X and Y directions, my approach of placing the resolution test pattern on top of the grating also enables an investigation into the role of refractive index *contrast*, and its effect on the spatial resolution. This is an important question when resonant gratings are used as biosensors, where the refractive index contrast between a living cell and culture media, for example, can be small, i.e. of order 10^{-2} RIU [130]. To this end, I prepared sucrose solutions of varying concentrations and used these to vary the refractive index of the medium surrounding the resist pattern on the grating. Sucrose was chosen instead of glucose due to its substantially higher solubility, allowing much higher refractive index solutions to be prepared in an effort to index-match to the FOx resist (i.e. reduce the index contrast to zero). The refractive indices of sucrose solutions are obtained from [131, 132], where a 150% w/v (1.5 g/mL) solution yields a refractive index of $n \approx 1.61$. This solution is approaching saturation point (2 g/mL), and dilutions with water lead to any refractive index down to $n = 1.333$. The refractive index of the FOx resist (n_{FOx}) is found in the literature to be between 1.39 and 1.40 [133], but this is also known to increase after electron-beam exposure [134], so the refractive index of the FOx structures fabricated here is not known exactly. Measurements using an ellipsometer would have been carried out if an instrument had been available, as this would be the best method for determining the true refractive index of the resist resolution patterns. Nevertheless, I have still been able to estimate the value of n_{FOx} from my measurements which are presented below.

5.4.1 Results: simple slab of resist

Beginning, as before, with a block of resist, I obtain resonance maps taken at different values of surrounding liquid index (n_{liquid}) by flowing different sucrose solutions into the flow channel. The map for water (0 %) is shown in figure 5.15(a). Extracted from this map is the average resonance wavelength within two different regions of interest (ROIs), shown in figure 5.15(b) as a function of n_{liquid} . The fact that λ_R on the resist slab (yellow line)

increases is an indication that the resonant mode is also sensing the liquid changing *above* the resist slab. Having previously measured the penetration depth to be around 180nm (section 5.2.2), this is to be expected since the thickness of the resist slab is only 100nm (from the AFM measurements). Thus there is some field overlap into the liquid above the resist. This was unintentional, as the FOx resist was expected to be much thicker at the time of spin-coating. Nonetheless, this effect is not ignored in the following analysis, and it contributes to a more detailed picture of the behaviour when thin layers are present on the sensor surface, as is often true for biological samples.

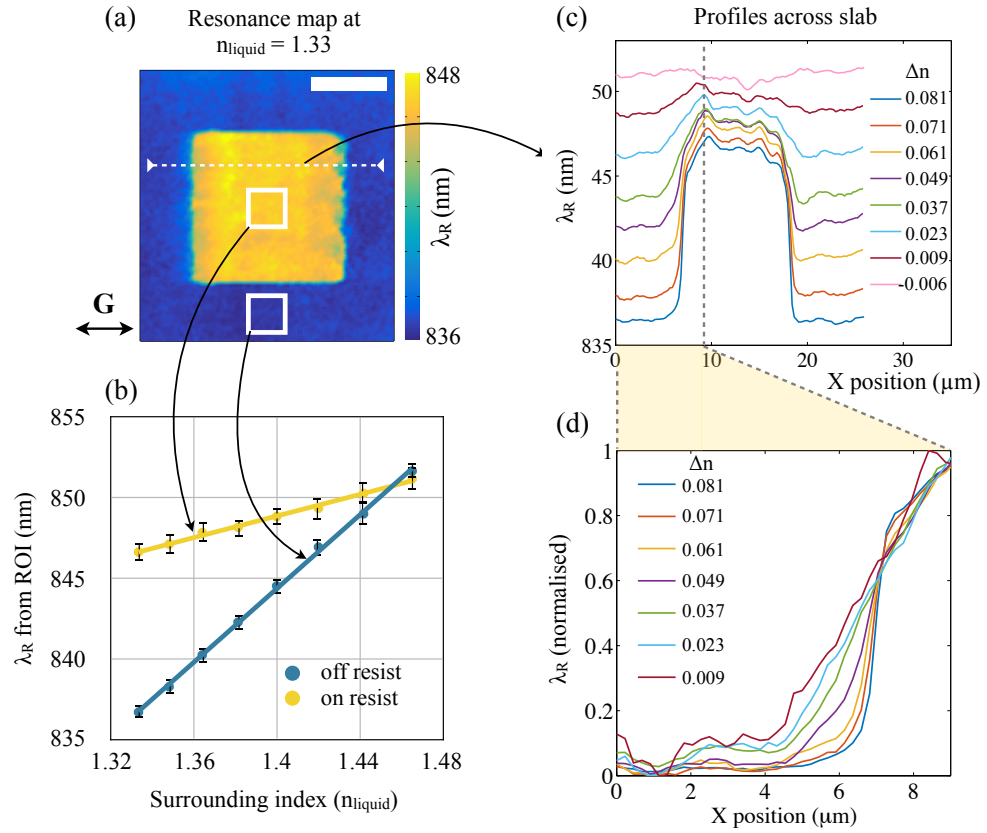


FIGURE 5.15: (a) Resonance map showing a slab of resist on the grating surface, surrounded by water ($n_{liquid} = 1.333$). Scale bar = $10\mu\text{m}$; (b) Resonance wavelength measured from the two indicated ROIs (on and off the resist) as n_{liquid} is increased. Error bars are obtained from the standard deviations of λ_R over each ROI; (c) Profiles measured along the white line indicated in (a), showing resonance wavelength shift vs. X position for different index contrasts (Δn); (d) zoomed-in and normalised section of the graph shown in (c).

Much more can be learned from the data contained in figure 5.15(b). For example, the crossing point of the two lines gives an estimation of the refractive index of the FOx layer. And the relative slopes of the lines, which correspond to the sensitivity, can be related to the different EM field overlaps in each region. The sensitivity in the region above the resist is significantly lower, since much of the field resides within the FOx slab with only a small part of the evanescent tail extending further than this. Since the resonance wavelength

measured from the resist-covered region is not constant as n_{liquid} is varied, it is sensible to define an average refractive index for the FOx:

$$n_{avg}(n_{liquid}) = \alpha n_{FOx} + (1 - \alpha)n_{liquid} \quad (5.4)$$

This equation is based on a simple linear average of the different refractive index regions, where α is an indicator of the proportion of electric field overlap in the n_{FOx} , while the remaining portion $(1 - \alpha)$ overlaps with n_{liquid} . From the measured data shown in the graph in figure 5.15(b), α can be calculated, and is found to be ≈ 0.70 . This value gives an indication that there is a 70% overlap of the resonant mode with the FOx and a 30% overlap with the liquid *above* the FOx. These are reasonable values considering the exponentially-decaying field extends to ~ 180 nm and yet the FOx is only 100 nm thick. Substituting the extracted values for α and n_{FOx} , the equation for n_{avg} can be rewritten as:

$$n_{avg}(n_{liquid}) = 0.700n_{FOx} + 0.300n_{liquid} = 1.019 + 0.300n_{liquid} \quad (5.5)$$

I note here that this model ignores the possibility that the FOx may not penetrate fully into the grating grooves. If this is true, then there may be air trapped under the FOx, isolated from the surrounding liquid. Therefore, the expression for n_{avg} should include some overlap with air. However, since air has a much lower refractive index than the other materials involved, the field overlap is expected to be minimal ($< 10\%$) and will not have a significant affect on the value of n_{avg} . Finally, the refractive index *contrast* between the FOx structures and the surrounding liquid can now be defined as $\Delta n = n_{liquid} - n_{avg}$:

$$\Delta n(n_{liquid}) = n_{liquid} - (1.019 + 0.3n_{liquid}) = 0.7n_{liquid} - 1.019 \quad (5.6)$$

Thus, zero contrast is achieved when $n_{liquid} \approx 1.456$ (equal to the index of the FOx), and for values larger than this, Δn becomes negative, indicating that the index of the surrounding liquid is *higher* than n_{avg} .

Moving back to the measurements of the resist slab, figure 5.15(c) shows profiles of the resonance wavelength along the X direction, across the slab, measured at different values of Δn (calculated using equation 5.6). As Δn is decreased, so too does the resonance shift caused by the slab. Normalising this data (shown in figure 5.15(d)) allows a comparison of the resonance wavelength profile at the edge of the slab. As Δn decreases towards zero, the slope of the transition becomes less steep, i.e. it becomes blurred out in the resonance map, and the sharpness of the edge is lost. This can be explained by thinking about the propagation of the resonant mode across the edge of the resist. The mode beneath the resist (at a higher wavelength) cannot propagate very far away from the slab, since the grating here cannot support it due to the lower refractive index of the surrounding liquid. But, as the index of the liquid is increased, the mode beneath the resist is able to penetrate further and

further out from beneath the slab. The same occurs for the resonance on the liquid-covered side of the grating, penetrating further under the slab as Δn is reduced towards zero.

5.4.2 Results: ruler resist pattern

While the previous results qualitatively show that reducing refractive index contrast reduces the sharpness of the resonance map, I now focus on the ruler resist pattern to show more quantitative measurements. Figures 5.16(a-g) show the resonance maps taken from a portion of the resolution test pattern while the index of the surrounding liquid is increased using sucrose solutions. Here, I used even higher index solutions than before in order to exceed the index of the FOx patterns. As n_{liquid} is increased, Δn between the resist bars and the liquid approaches zero, as suggested by the decreased contrast in the resonance images. The resist patterns in figures 5.16(f,g) generate a *lower* resonance wavelength than the surrounding grating, showing that n_{avg} has been surpassed by the surrounding liquid. Correspondingly, Δn here is negative. Figure 5.16(h) shows the transmission spectra extracted from individual pixels in the map in (a), showing how the spectrum shifts when moving off a resist bar and on to the liquid-covered grating.

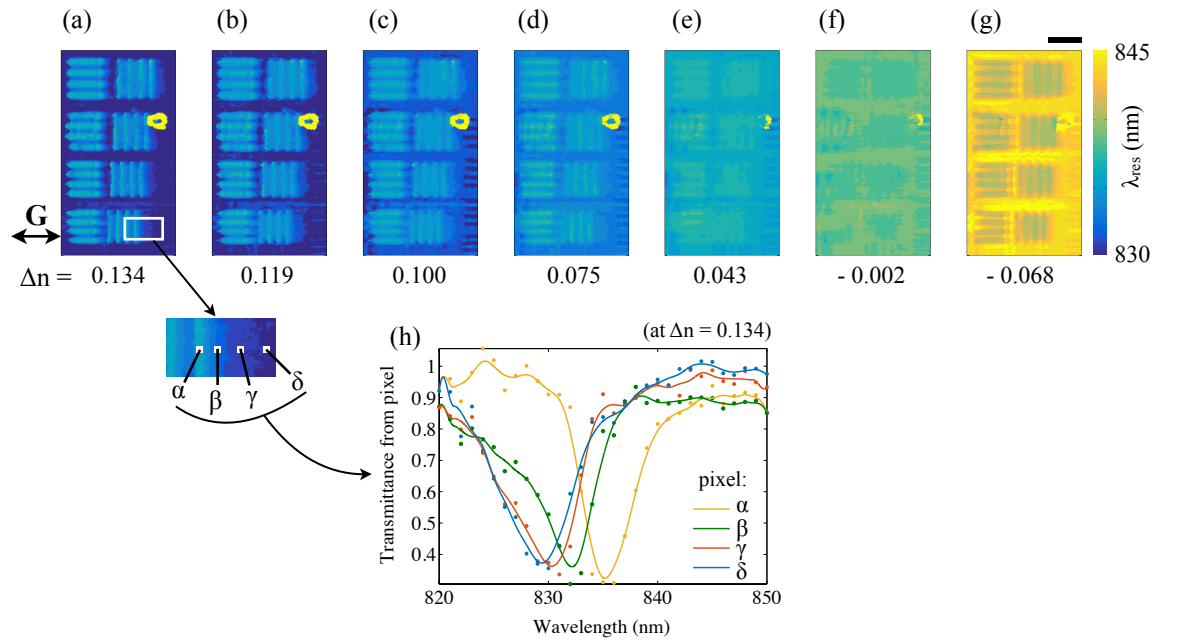


FIGURE 5.16: (a-g) Resonance maps of the ruler pattern at different values of Δn . Scale bar = 50 μm ; (h) Spectra extracted from individual pixels in the map in (a), corresponding to different locations moving off a bar of resist ($\alpha - \delta$).

As in the previous section for a single slab of resist, figure 5.17(a) shows a plot of the average resonance wavelength both on and off a resist bar as n_{liquid} is changed. Again, the yellow line has a positive slope due to the fact that the FOx is thin enough to allow the mode to be affected by the surrounding liquid. Additionally, figure 5.17(b) shows

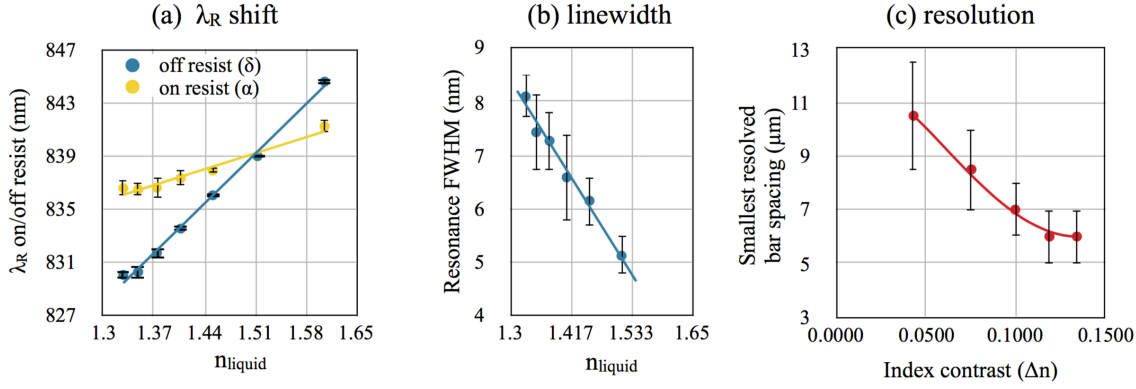


FIGURE 5.17: (a) Resonance wavelength extracted from the regions on and off a resist bar, vs index of the surrounding liquid (n_{liquid}); (b) measured resonance linewidth (FWHM), averaged over a small liquid-covered region of the grating, vs n_{liquid} ; (c) Spatial resolution measurement - smallest resolvable resist bar separation vs. refractive index contrast.

the average resonance linewidth (FWHM) from a liquid-covered region of the grating (i.e. away from the FOx). The trend is that the FWHM decreases as n_{liquid} is increased. This is consistent with resonant grating theory: as n_{liquid} is increased, not only does the contrast between the liquid and FOx structures become lower but the contrast between the Si_3N_4 grating ridges and the liquid-filled grooves also becomes smaller. It is well known that by decreasing the grating contrast, resonant modes tend towards higher Q-factors [43] since they have an increased in-plane propagation length. In analogy, decreasing the index contrast between the layers of a distributed Bragg reflector (DBR) also causes a narrowing of the reflection bandwidth. Finally, using the same approach shown in section 5.3.3, where the resolution in the X and Y directions was shown, a profile is measured through the bars in the resonance maps and the spatial resolution limit (along X) as a function of refractive index contrast (Δn) is determined. This is plotted in figure 5.17, showing the trend that spatial resolution decreases with Δn .

5.4.3 FDTD Simulations

I end this chapter by modelling the spatial resolution dependence on refractive index contrast using finite-difference time-domain (FDTD) simulations. For this purpose, I use MEEP; a free software package for computing electromagnetic simulations [135]. The model I created is shown in figure 5.18(a), and is comprised of a finite number of periods (150) of the resonant Si_3N_4 grating, half of which are covered with a slab of resist having index of 1.41, to simulate a resist like FOx as used in my experiments. Also in equivalence to the experiments described above, the refractive index of the surrounding liquid is changed, thereby altering the index contrast with the resist slab. As this is done, the transmission spectrum is extracted at discrete positions along the grating by collecting the transmitted light in different bins situated above the grating. This approach gives an indication of how the resonance wavelength changes as a function of position (X), particularly across the edge

of the slab ($X = 0$), and also as a function of refractive index contrast. The thickness of the resist slab in the model was set to be 500 nm, such that it is greater than the penetration depth of the mode (unlike the case for the experiments shown previously). This makes the calculation of the refractive index contrast simpler, since the mode senses either the resist or the liquid, not a combination of both. The results remain equally comparable to the experimental situation.

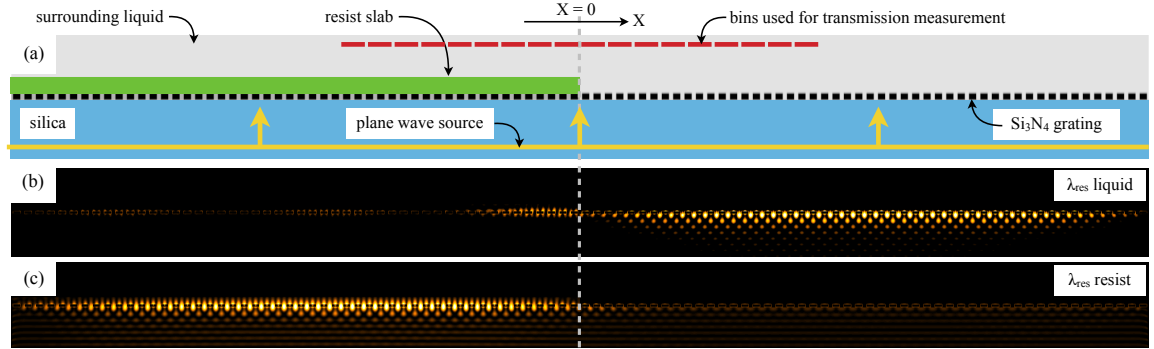


FIGURE 5.18: (a) diagram of the model used in MEEP; electromagnetic field energy density (normalised, black = 0, white = 1) is shown at two different wavelengths corresponding to resonance beneath the resist block (figure 5.18(b)) and resonance for water covering the grating (figure 5.18(c)).

Figures 5.18(b,c) show the (normalised) electromagnetic energy density at two different incidence wavelengths: the resonance beneath the resist is excited at approximately 848 nm (figure 5.18(b)), while it is at approximately 830 nm for water (figure 5.18(c)). The field profiles clearly highlight a higher field intensity either below the resist slab or below the water, depending on the incidence wavelength.

In order to extract some meaningful numbers from these simulations, I plot the resonance wavelength as a function of position in X in figure 5.19(a). I show this for four different refractive index contrasts by increasing the index of the surrounding liquid, where the resonance wavelength measured on the right-hand side of the curves increases correspondingly. I note that the resonance wavelength at the left-hand side of the curves (i.e. on the resist block) is almost constant since the resist is thick enough for the resonant mode to be unaffected by the liquid above. To compare the four different profiles, I normalise them as shown in figure 5.19(b). As the refractive index contrast is reduced, the slope of the transition becomes less steep, in good agreement with experimental results shown in figure 5.15(d).

To quantify the changes in slope of the transition, I define a "transition length" as being the distance required along X for the resonance wavelength to drop from 0.8 to 0.2 as

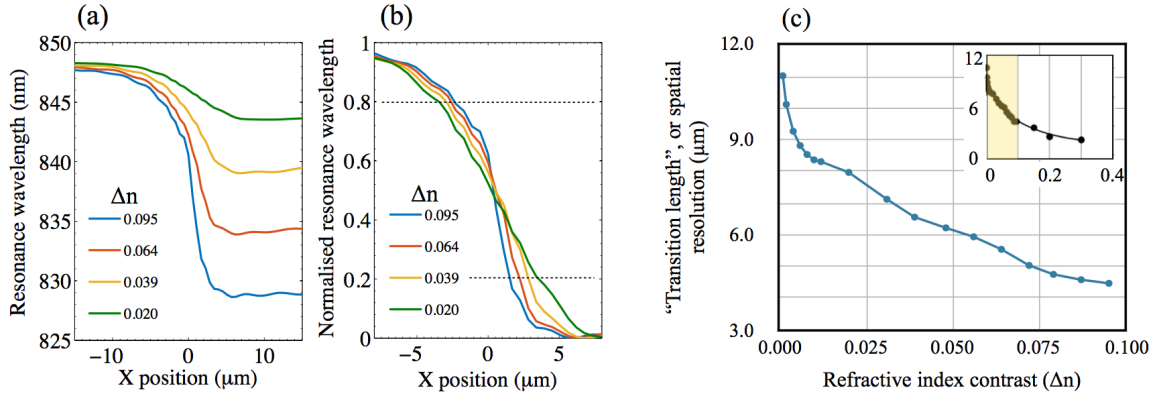


FIGURE 5.19: (a) Resonance wavelength as a function of X position for different refractive index contrasts; (b) Normalised version of the same graph, zoomed-in on $X=0$; (c) Plot of the transition length (defined in the text), i.e. spatial resolution, vs. refractive index contrast (Δn); Inset: extended range of Δn , with the shaded yellow part indicating the area used for the main plot.

indicated by the dashed lines in figure 5.19(b). Repeating this analysis for different refractive index contrasts gives the results plotted in figure 5.19(c). Again, there is a trend of spatial resolution becoming worse as refractive index contrast is lowered, with asymptotic behaviour as $\Delta n \rightarrow 0$. This is expected: at zero index contrast, there are no differences in λ_R and therefore there is no contrast in the resonance map. Although the choice of the 0.8 and 0.2 thresholds here is arbitrary, it still provides a useful way to compare the four different curves after they have been normalised. Choosing different threshold values would not change the overall shape of the spatial resolution dependence, but instead would shift it up or down in figure 5.19(c). Therefore, the spatial resolution obtained from my simulations serves to give a good idea of the trend as refractive index contrast is reduced. An advantage of studying the spatial resolution using my model is the ability to extend the study to much more extreme index contrasts than is possible experimentally. To this end, I plot data for values of Δn ranging from 2×10^{-4} up to 0.3, shown in the inset of figure 5.19(c). At large index contrasts, the spatial resolution converges towards a finite positive value which is determined by the size of the bins used to collect the transmitted light, i.e. the imaging resolution. Eventually, the refractive index of the surrounding liquid would become so high that it index-matches to the Si_3N_4 grating, at which point the grating is lost and no resonance exists.

5.5 Summary and discussion

In this chapter, I started by demonstrating the concept of measuring a resonance map of a resonant grating surface in order to extract spatially-resolved refractive index information. Next, I explored two important characteristics of a resonant grating surface in terms of its imaging capability: the penetration depth and the spatial resolution. Using a simple yet

surprisingly accurate technique, i.e. by making use of glass lenses, the penetration depth was found to be around 183 nm. This was extensively backed up with an RCWA model, a study that also uncovered some interesting differences between the penetration depths and field profiles of TE and TM resonant modes.

I then concentrated on the topic of spatial resolution, where a novel method of fabricating a resolution test pattern on top of the grating was employed to probe the spatial resolution in the X and Y directions. In particular, resolutions of 6 μm and 2 μm are measured in the X and Y directions, respectively. The physical basis of this asymmetric resolution is discussed in the context of in-plane propagation, and the validity of this model is checked using experiments on 2D gratings. A unique advantage of my approach is the ability to alter the refractive index contrast between the resolution patterns and the surrounding liquid, allowing a thorough investigation of the dependence of spatial resolution on refractive index contrast. Here I find the resolution decreasing with index contrast, a result that is supported by a FDTD model focusing on the edge of a resist slab. There are only a few publications in which the spatial resolution of a resonant grating biosensor is quoted explicitly, so it is challenging to directly compare my results to those reported in the literature. I refer first to [42], where a TiO_2 resonant grating sensor is used to image the refractive index shift caused by printed DNA monolayers. The DNA is applied directly on to the surface of the sensor in 50 μm spots, and there is an obvious decrease in resolution in the X direction, visible from the blurred-out edges in the resonance map. While resolution is not quoted, I believe it to be in the region of 10-20 μm . For such a thin film of biomolecules, the refractive index contrast would be expected to be very low, as this spatial resolution suggests. Another example is found in [136], where individual TiO_2 nanoparticles are imaged with a resonant grating. The radius of the particles is just 500 nm, however the authors state that the resonance shift caused by the nanoparticles extends laterally by approximately 6 μm , and they quote that in order to resolve two neighbouring particles, a separation of at least 3.2 μm is required - in good agreement with the results presented in this chapter.

Chapter 6

Biosensing results

6.1 Introduction

In chapters 4 and 5, I focused separately on the sensing and imaging capabilities of the resonant grating sensor. These aspects are now brought together to harness a wealth of information from different biological systems. I begin by applying the sensor to monitor biofilm development before moving on to more extensive experiments on living cells. These are motivated by the potential of imaging, label-free and in real time, the secretion of a specific biomarker as it is released from a cell *in vitro*. The details of cell culture and incubation are discussed, as well as an investigation into the effect the grating has on the growth of the cells. Examples of resonance imaging of living cells are presented, where the resonant grating offers much greater imaging contrast and information on cell attachment than conventional microscopy. In the effort to measure secretion from cells, in-depth experiments are undertaken using hybridoma cells, which release IgG that can bind to the functionalised sensor.

6.2 Analysis of biofilm formation

6.2.1 Motivation

The first application of the grating sensor is to monitor the growth of a microbial biofilm. Biofilms are the oldest form of biological community on our planet, thought to have originated some 3.6 billion years ago [137]. First described by van Leeuwenhoek in the 17th century, a biofilm is a microorganism that can form on a wide variety of substrates that are submerged in an aqueous environment, such as the ocean or rivers, a water filtration system, or in the human body. They are primarily composed of bacteria, fungi, diatoms, protozoans, larvae and spores [17], with these components being connected by a polysaccharide matrix [138]. In comparison to individual microorganisms in suspension in the ocean, for example, biofilms exhibit a distinct communal behaviour, rapid growth rates and specific attachment mechanisms [139]. Everyday evidence of microbial biofilms is often found as

”slime”, and may be found on almost any submerged substrate. Due to the abundance of biofilms, their role in medical, industrial and environmental settings is prolific, where the collective behaviour of a biofilm provides an extra degree of protection and enables them to survive in harsh environments [18]. This presents a severe issue in industrial and environmental settings, where a biofilm can degrade the performance of fluidic systems such as heat exchangers [140], and can trigger the onset of corrosion and biofouling. In the context of medicine and healthcare, some 80% of all bacterial infections are biofilm-related [141]. There are numerous potential sites for biofilm contamination, including heart valves, dental implants, contact lenses, catheters and prosthetics [142], and a major obstacle is that they exhibit strong resistance to antibacterial agents [143, 144], rendering them difficult to remove and leading to persistent infections [18]. A striking example is reported by Marrie et al. [145], where a patient with an implanted pacemaker suffers three consecutive cases of bacterial infection from *S. Aureus*. After the onset of each infection (vomiting, fever, shaking and sweating) he was treated with antibiotics for a number of weeks before being discharged from hospital, only for the infection to return within a matter of days. After the third admission, the pacemaker system was removed entirely and the infection did not return. Subsequent examination of the pacemaker cables revealed a heavy biofilm of *S. Aureus*, despite the intensive antibiotic treatment. Thus, biofilms play an important role in the cause and spread of infections within healthcare environments, and estimates of the cost of caring for such healthcare-associated infections are in the region of tens of billions of US\$ per year [146]. As such, there is considerable research effort in biofilm detection and monitoring, and for a comprehensive review of biofilm characterisation methods, I refer to Denkhaus et al. [147]. Here, for the first time in the literature to my knowledge, I monitor biofilm development using a resonant grating sensor to reveal information about the growth characteristics without the use of fluorescent labels.

6.2.2 Results

Figure 6.1 shows a sequence of resonance maps, acquired every four hours during biofilm development. The sensor was initially treated with piranha cleaning, and the bacteria-rich analyte is obtained from a small lake and has been filtered to remove any particles exceeding $5\ \mu\text{m}$. The area shown in these maps is relatively large ($150\ \mu\text{m} \times 250\ \mu\text{m}$), and indicates widespread but inhomogeneous biofilm growth, causing a resonance wavelength shift of up to $\sim 2\ \text{nm}$ after 52 hours.

The resonance imaging also reveals small regions of very high optical density, shown in figure 6.2 (from the same experiment). The formation of this small island of material causes a significant resonance shift of $\sim 7\ \text{nm}$, in comparison to the shift of $\sim 2\ \text{nm}$ measured above.

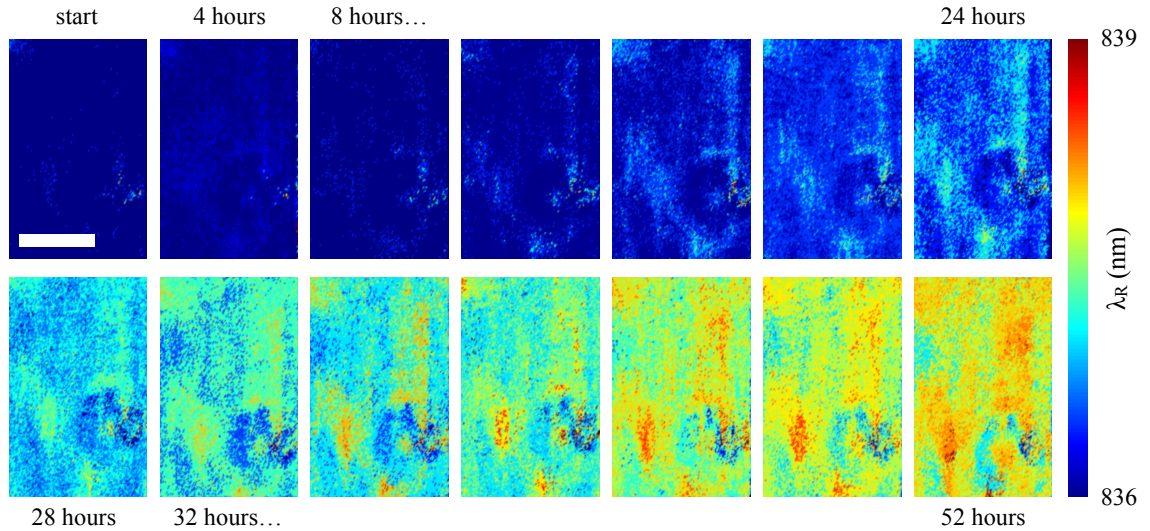


FIGURE 6.1: Resonance map time-lapse, taken every 4 hours, showing biofilm growth over a large area of the sensor (approx. $150\ \mu\text{m} \times 250\ \mu\text{m}$). Scale bar is $100\ \mu\text{m}$.

This further demonstrates the highly irregular structure of the biofilm.

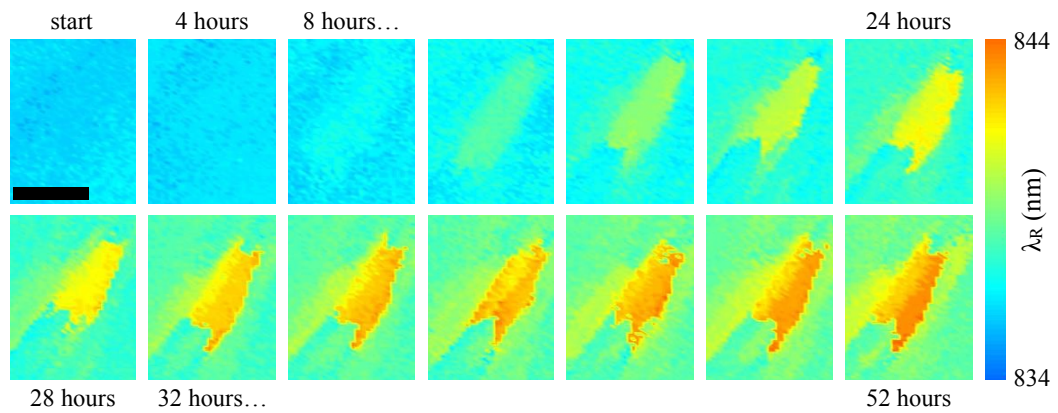


FIGURE 6.2: Resonance map time-lapse, taken every 4 hours, showing a high density biofilm island forming on the sensor. The scale bar is $50\ \mu\text{m}$.

To accompany the biofilm measurements above, fluorescence microscopy images were captured using an optical microscope with a magnification high enough to resolve individual bacterial colonies. After the biofilm growth, the samples are washed and fixed using paraformaldehyde. Next, the fluorescent label DAPI (4,6-diamidino-2-phenylindole) is applied. DAPI is capable of passing through intact cell membranes and consequently binds to DNA. Because the bacterial cells are prokaryotes, the DNA is not confined within a cell nucleus and is instead distributed throughout the whole cell volume, making DAPI an ideal marker for observing bacteria. The excitation wavelength of DAPI (once bound to DNA) is in the ultra-violet (364 nm) and the emission is in the blue region of the visible spectrum (450 nm) [148]. A fluorescence image is shown in figure 6.3(a). Along with isolated bacteria, there are clear colonies forming, as seen in the resonance maps. It is worth noting here

that without the use of a fluorescent label, it would be challenging to observe the biofilm colonies, whereas the resonance maps provide excellent contrast and are label-free.

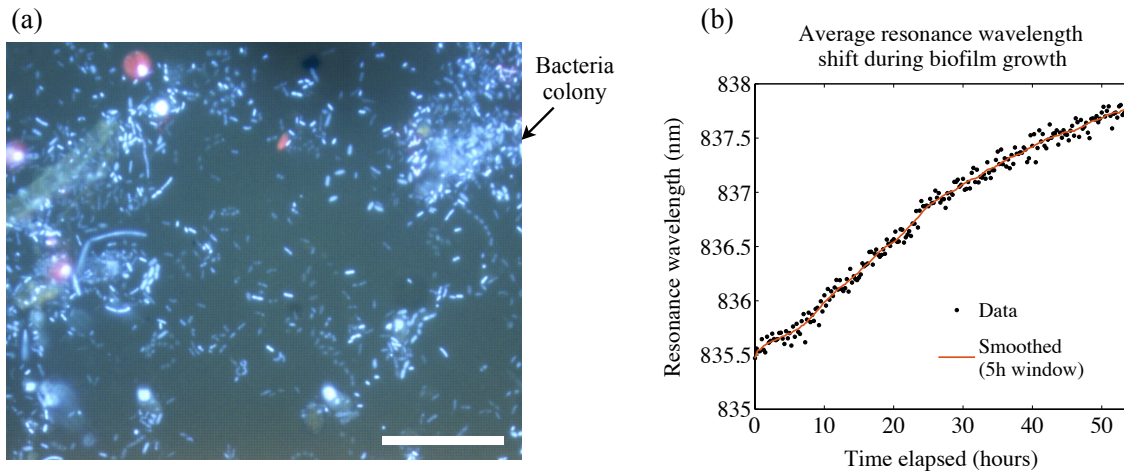


FIGURE 6.3: (a) Fluorescence microscope image of a DAPI-stained bacteria, cultured on a resonant grating (images obtained with help from Dr. Matthias Fischer, Department of Physics, University of York). Scale bar = $30\ \mu\text{m}$. A prominent colony of bacteria is indicated. (b) Resonance wavelength vs time, averaged over a similar region of interest as used for the maps in figure 6.1, with black dots showing raw data and a red line showing data after smoothing with a window of 5 hours.

To conclude this section on biofilm monitoring, I investigate the dynamics of binding revealed by the resonance wavelength shift extracted from a specific region on the grating. Figure 6.3(b) shows the averaged resonance wavelength as a function of time, extracted from a similar region to that used in the resonance maps of figure 6.1. The shift is found to be quite non-linear, starting with a short "lag" time before a period of exponential growth that then slows. This activity is in agreement with the typical "three-phase" growth dynamic reported in the biofilm community [149]. The resonant sensor is shown here to be capable of monitoring the initial stages of biofilm growth in the first few hours, where the surface is modified with proteins before the buildup of bacteria colonies, and it is at this stage that intervention with antimicrobial treatment would be most effective. With hindsight, the measurement should ideally have continued for longer, but unfortunately this was impractical at the time.

6.3 Considerations for cell culture

Before moving on to applying the sensor to the study of cells, I first discuss some important aspects of cell culture that I have learned and depended upon.

6.3.1 Incubation

Mammalian cells require certain environmental conditions to ensure that they are kept healthy and viable. The four main considerations are the temperature and pH of the culture medium, a supply of nutrients, and sterility. The cells are incubated to a temperature of 37°C to match that of the cell's natural environment (body temperature). The culture medium contains a rich array of ingredients to promote cell growth and health, including salts, amino acids, vitamins, glucose, serum, and others. Usually, it also contains a "buffering" component such as sodium bicarbonate (NaHCO_3), which balances with dissolved CO_2 and allows the pH of the medium to be controlled. Incubation with a bicarbonate buffer occurs at an elevated CO_2 level of between 5% and 10%, resulting in a pH of around 7.3. A colour indicator such as phenol red is used as a rough pH indicator that turns yellow or purple if the media is too acidic or alkaline, respectively.

To achieve a stable incubation temperature during my *in-vitro* measurements on cells, I developed a small heated stage (figure 6.4) that can be used in combination with the reflection measurement setup (figure 2.6(b)). The stage incorporates a reservoir of water, immersed in which is a petri dish containing the resonant grating chip, and the cells in culture medium. Typically, I bonded the grating chip to the petri dish using a UV-curable optical adhesive (Norland). The reservoir water is warmed via two electronic heating pads connected to a basic thermostat, and remains at $37^{\circ}\text{C} \pm 1^{\circ}\text{C}$. Despite achieving the correct temperature, my stage does not currently provide the 5% CO_2 level needed to maintain proper pH in bicarbonate-buffered media. To solve this issue, I make use of a different buffering agent called "HEPES", which is able to maintain a pH of ~ 7.3 in normal atmospheric CO_2 conditions. HEPES is an organic compound with formula $\text{C}_8\text{H}_{18}\text{N}_2\text{O}_4\text{S}$, and it is frequently used for time-lapse imaging of cells while they are outside the incubator (i.e. in normal CO_2 conditions) for an extended time period. Although HEPES is a better regulator of pH and does not require elevated CO_2 , the disadvantages of using this buffering system is that it is toxic to some cell types and is more expensive than bicarbonate [150].

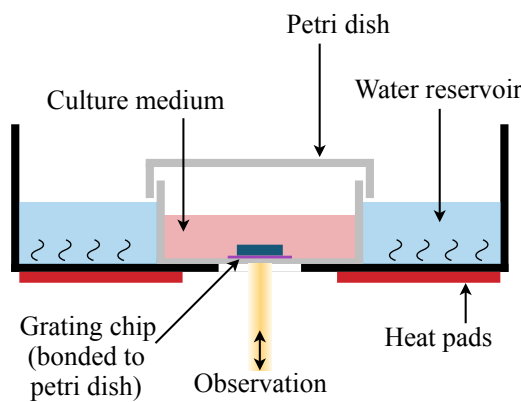


FIGURE 6.4: Schematic of the cell incubation stage.

6.3.2 SEM analysis of cells cultured on a resonant grating

A further consideration to take into account is the effect of the grating on the cell growth. On the scale of the mammalian cells used here ($5\mu\text{m}$ to $30\mu\text{m}$), can the size of the grating (period = $0.56\mu\text{m}$) be ignored? In order to investigate what effect, if any, the grating has on the growth of cells, I cultured a neuroblastoma cell line (B104) on a grating before probing the cells with a scanning electron microscope (SEM). The grating was first treated using poly-D-lysine (PDL) to promote the attachment of cells. PDL is polymer that has a positively-charged amine group that can bind to negatively-charged sites on the cell surface, and is widely used throughout cell culture. After cell culture, the cells are fixed using glutaraldehyde/formaldehyde and osmium tetroxide solutions, dehydrated using an ethanol series, and finally a ~ 5 nm conductive coating of gold-palladium alloy is sputtered across the cells and grating. Figure 6.5(a) shows SEM images of the cells on a non-patterned surface, while figure 6.5(b) shows the cells on the grating (grating direction is indicated). There is an obvious trend for the cell growth to be directed along the grating grooves, presumably due to increased surface area available for adhesion. B104 neuroblastoma cells exhibit neurite-like "processes"; thin projections along which electrochemical signals propagate to and from the nucleus of the cell. Figures 6.5(c,d) show zoomed-in images of such processes, indicating that the grating grooves are used as supports by the cell. The effect on cell growth seen here is not a new discovery; it is well-documented that patterned substrates can provide control over cell growth and behaviour [151, 152]. Aside from the directional growth, the cells remain viable and healthy when cultured on the grating, by comparison to cells cultured in a standard microwell plate.

6.4 *In-vitro* cellular imaging

Resonant gratings have already been demonstrated as an excellent tool for probing living cells. Lidstone [36] and Chen [37] et al. use a resonant grating to investigate cell attachment to a surface, in particular focusing on the changes induced by the application of drugs that influence growth and development. Lin et al. [153] also present a detailed study on cell attachment, highlighting the ability of the resonant grating surface to distinguish, again via differences in adhesion, cells with or without specific surface molecules. Fang et al. have also shown advances in using resonant gratings for biosensing on a cellular level by measuring changes in cell adhesion and distribution of material within the cell [28, 27], and additionally they have investigated cell clustering behaviour [39]. Lastly, Nazirizadeh et al. report an excellent analysis on the topography of living cells, where the measured resonance shift is calibrated to allow an accurate estimation of cell thickness [40].

To demonstrate the performance of my sensor for the *in-vitro* analysis of cells, figure 6.6(a) shows a resonance map of COS7 kidney cells, after culture on the grating for two

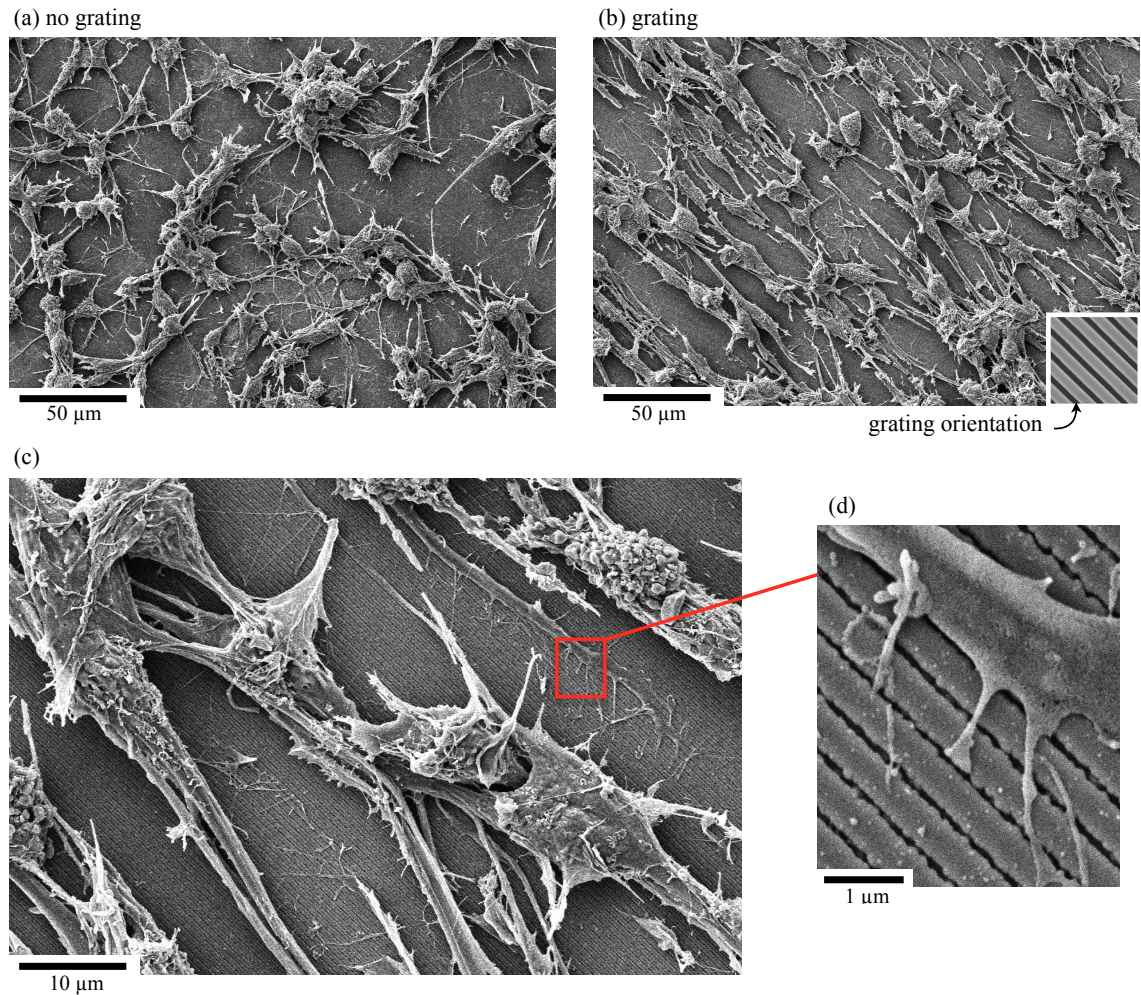


FIGURE 6.5: SEM images of B104 neuroblastoma cells after culture on a grating (images acquired by Meg Stark, Department of Biology, University of York). The influence of the grating on the direction of growth of the cells is clear by comparing (a) and (b), while (c) and (d) show images at a higher magnification.

hours. As before, the grating is treated with poly-D-lysine to encourage cell attachment. It is immediately clear that the resonance map shows significantly higher contrast than the conventional brightfield image (figure 6.6(b)). These two images can be directly compared as the brightfield image is one of the slices of the hyperspectral stack used to generate the resonance map. This is due to the exquisite sensitivity of the resonance wavelength to refractive index changes at the surface. Furthermore, the true extent of the cell membrane is revealed - something that would only be seen using fluorescence labelling or phase contrast microscopy, for example. There is also the suggestion that sub-cellular components such as nuclei are detected in the resonance map, however, detection of these requires close proximity to the sensor surface ($< \sim 180 \text{ nm}$), and therefore not all cell nuclei are visible. The size of sub-cellular components such as the nucleus ($< 10 \mu\text{m}$) is also approaching the spatial resolution limit of resonance imaging, as discussed in chapter 4. Finally, there is an indication that the extra-cellular matrix (ECM) is detected, as much of the space between individual cells is filled with some material of higher refractive index than the background.

This is thought to be seen as the light blue-green colour between the cells on the resonance map, and it is completely invisible in the brightfield image. The ECM is a network of fibrous proteins such as collagen, which are secreted by the cells to provide the structure needed to form tissue.

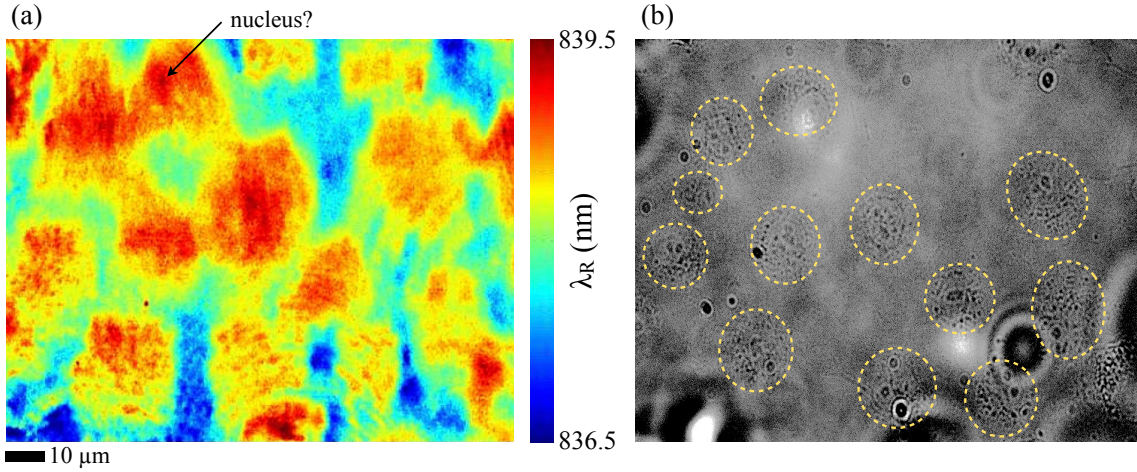


FIGURE 6.6: Resonance map (a) and corresponding brightfield image (b) of COS7 cells *in-vitro*, after two hours of culture on the resonant grating. The colour scale in (a) shows the resonance wavelength (λ_R) in nm. Yellow dashed circles in (b) indicate the locations of some of the cells visible in the brightfield image.

6.4.1 Extracting spectral information

The resonance map contains much more information than just a contrast mechanism to generate an image. Every pixel in the map contains resonance information, so by selecting a specific region of interest (ROI), statistical analysis becomes a powerful way to monitor changes to the resonance wavelength. Figure 6.7 shows this principle of extracting spectral information from different ROIs on the resonance map. The maps in the top row show a single B104 cell after a short period of culture on the grating surface. The bottom row shows histograms of the resonance wavelength, i.e. the number of pixels having a particular resonance wavelength. B104 cells typically do not adhere strongly to substrates, and they tend to remain quite rounded instead of flattening out over the surface on which they are cultured. This is evident from the fact that the edges of the cell in the resonance images here are not very well-defined in comparison to those shown in figure 6.6. The SEM images shown in figure 6.5 also indicate that the cells sit proud of the grating surface. In contrast, COS7 kidney cells exhibit a strong attachment to the surface, causing them to spread out and become quite flat.

These histograms are useful not only for revealing the average size of the resonance shift caused by the cell (~ 1.7 nm here), but the shape of the histogram can reveal information about size of the cell, contact area, etc. For example, when a large area is monitored

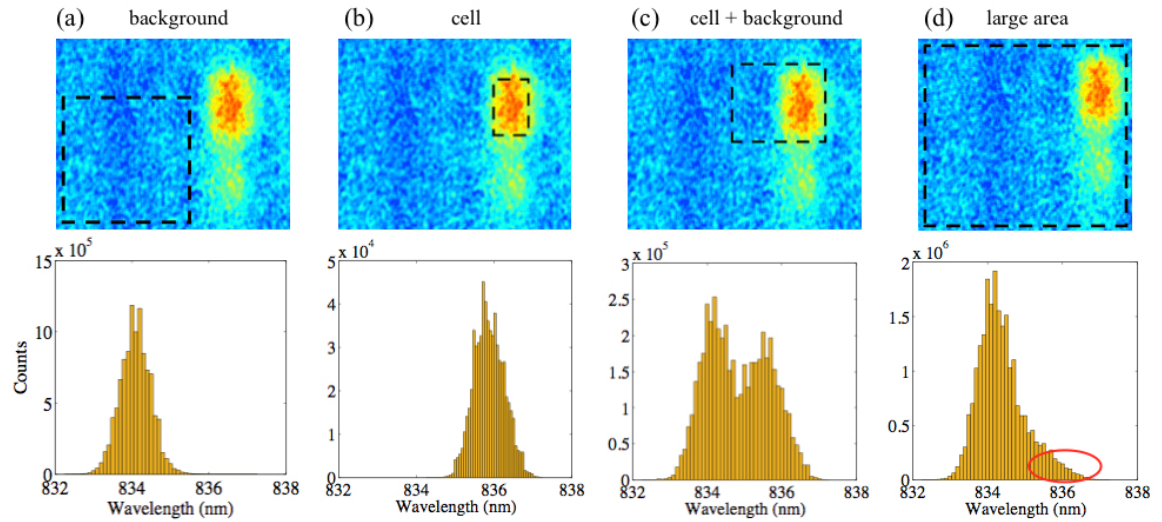


FIGURE 6.7: Resonance maps (top row) and histograms (bottom row) showing resonance wavelength statistics within each ROI indicated on the maps. (a) background only; (b) cell body only; (c) $\sim 50:50$ combination of cell and background; (d) a large area. The red ellipse indicates the longer "tail" on the histogram caused by the presence of the single cell.

(figure 6.7(d)), the dominant resonance wavelength is that of the background, but the tail of the histogram (indicated by the red ellipse) is more prominent due to the presence of the cell within the field of view. Monitoring this statistical data over time could be an invaluable tool for measuring cellular response to drugs, cell movement, or cell attachment, for instance.

6.4.2 Cell detachment

In order to investigate the importance of the incubation system when performing resonance imaging of cells, I imaged healthy cells over a time period of approximately 4 hours after the incubation system was turned off. Thus, the media gradually cools down from 37°C to ambient temperature ($\sim 20^\circ\text{C}$). During this time, the cells undergo necrosis (cell death), and they are no longer capable of adhering to the sensor surface. Figure 6.8 shows a series of resonance maps (top row) and the corresponding brightfield images (bottom row) as the media temperature cools with time. The cells used here are again B104 neuroblastoma cells. In the brightfield images, it is clear that the shape changes, and the neurite-like processes are contracted. There is also evidence of so-called "blebbing", whereby the internal structure of the cell (the cytoskeleton) is broken down and the cell begins to break up into separate pockets. This shape change is also revealed in the resonance images, but they also clearly show that the cell has detached from the sensor surface - an observation that is impossible to ascertain from the brightfield images. This exemplifies the wealth of information that is accessible by combining the resonance information with standard microscopy.

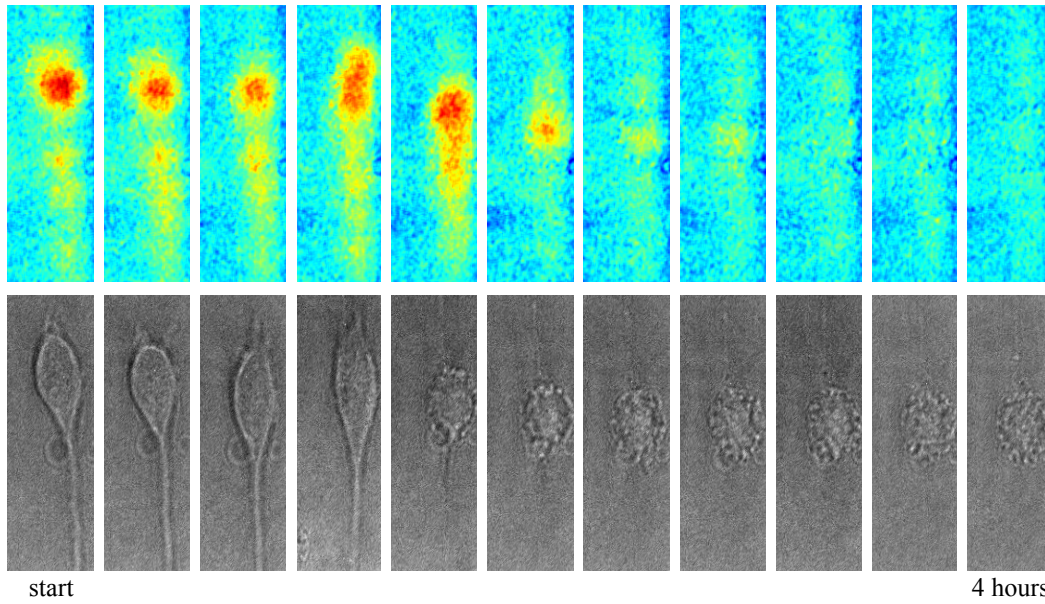


FIGURE 6.8: Time-lapse resonance maps and corresponding brightfield images during cell detachment after turning off the incubation system.

6.5 Imaging cellular secretion

6.5.1 Motivation

The final biosensing application I present in this chapter fully exploits the sensing and imaging aspects of the sensor to realise a potentially groundbreaking technique: to *image* the cellular secretion of a specific biomolecule, *in-vitro*, label-free, and in real-time. The resonant grating sensor is an ideal tool for achieving this, and with future refinements it could become a powerful way for cell biologists to gain a wealth of information about cell secretion and signalling processes throughout many research areas. So far, I have demonstrated the ability of the sensor to detect a biomolecule (chapter 4), and I have shown that imaging cells, *in-vitro*, and with a high degree of spatial resolution (a few μm) is feasible, providing a good incubation system is in place. It is the combination of high sensitivity to surface-binding with the ability to form images from this information that makes the resonant grating so promising for imaging cellular secretions. While there exist other methods to measure the cellular release of a particular biomolecule, they are often compromised by one of two caveats: To realise imaging, a fluorescent label must be applied to the antigen in order to detect it, potentially changing the cell behaviour or interfering with biochemical signalling pathways, or requiring a level of optical excitation that is harmful to living cells; or alternatively, the culture media (supernatant) must be removed from the cells and analysed using a separate experiment such as an ELISA, in which case all spatial information is lost; the result from this only quantifies the combined secretion from all of the cells.

These drawbacks can be avoided with the resonant grating. Not only can individual cells

be imaged, but the resonance shift due to the binding of a secreted target molecule also shows up in the image. Hence, a spatially-resolved measurement of localised binding after cellular secretion is possible, without fluorescent labels, and near real-time. Such a measurement would extend the applicability of resonant gratings as a biosensing tool, and would open the door to innumerable avenues of biomedical research. Examples might include studies to understand the dynamics of wound healing, where immune system cells secrete signalling molecules such as growth factors to regulate the healing process [154]. Another exciting application could be the measurement of neurotransmitter release at a neuronal synapse. Neurotransmitters are molecules that underpin fundamental brain functions such as emotions, cognition and motor control, while psychological disorders like addiction and schizophrenia, and neurodegenerative diseases like Parkinson's are also intimately related to the levels of neurotransmitter release and uptake in the human brain. For instance, serotonin levels have been linked to stress and depression [12], while glutamate plays a key role in the formation of memories and learning through a process known as synaptic plasticity [155, 13]. It is a major challenge to quantify neurotransmitter release after synapse activation, but success would enhance our understanding of the brain and disorders related to neurotransmitter deficiencies.

As a model system for measuring cellular secretion, I chose a hybridoma cell line. The name "hybridoma" is derived from the fact this it is a hybrid cell line, resulting from the fusion of lymphocytes (antibody-producing cells) with myeloma (tumor) cells. The "hybridoma technique" [156], established in the 1970s, is used to create a cell line that lasts indefinitely during cell culture (like tumor cells) while retaining the ability to produce monoclonal antibodies against nearly any antigen, and has since revolutionised research and therapy in biology and medicine [157]. In brief, the technique begins by exposing a mouse to a desired antigen, thus triggering an immune response and the generation of B-cells in the spleen, which are in turn capable of producing the correct antibody to the chosen antigen. Extracting a sample of B-cells from the spleen and fusing them with tumor cells results in a stable cell line that produces monoclonal antibodies for the desired antigen [158]. The particular cell line used here was obtained from Dr. M. Kullberg (Biology Dept, University of York) and produces rat-derived IgG antibodies at an expected concentration of 1-10 $\mu\text{g/mL}$.

6.5.2 Control experiments

To accomplish imaging of cellular secretion from the hybridoma cells, it was crucial to first carry out control experiments to determine the following:

1. That the cell culture medium alone does not contain any substance (including IgG) that may bind to the functionalised sensor and cause a false signal.

2. That the cultured cells do release IgG as expected, in a concentration high enough to be detected with my sensor.
3. That the sensor can be used successfully in "imaging mode" to make a spatially-resolved measurement of the resonance shift caused by IgG binding at a relevant concentration.

The following subsections present the results from two control experiments designed to address the points above.

6.5.2.1 Control experiment 1

The first control experiment is a case of repeating the assay shown in chapter 4 (figure 4.7), where IgG binding was measured directly from the spectral shift using a spectrometer. Here, however, instead of using PBS, culture medium is used as the "blank" solution before introducing the solutions containing IgG. In principle, proper functionalisation and blocking should prevent any non-specific binding from components in the media, but it is important to establish whether this is true. The media contains a large range of ingredients, including IgG, however, this is bovine-derived IgG that should not bind to the anti-rat IgG antibodies on the surface, according to the product specification. Nevertheless, it is sensible to test this, thereby addressing the first point in the list above. For the second point - to estimate the concentration of IgG being produced by the hybridoma cells - the supernatant is removed from the cell culture dish and this is used as the analyte containing IgG. Thus, no stock solutions of IgG are used in this experiment. By comparing the size of the binding shift here to that caused by the stock IgG solutions used in chapter 4, an estimation of the IgG concentration from the cells can be made, albeit a bulk measurement that includes secretion from all the cells in the petri dish. Figure 6.9 depicts an illustration and the results of control experiment 1.

It can be seen that the supernatant causes a significant resonance shift, over a timeframe of some 5 minutes. If the binding response is assumed to be similar to that shown in figure 4.7 of chapter 4, comparing the size of the shift during IgG binding here (~ 0.18 nm), with that for the $5 \mu\text{g/mL}$ IgG solution measured previously, gives a very crude estimation of the concentration of IgG in the supernatant to be $\sim 7 \mu\text{g/mL}$. This value agrees with the estimation of $1\text{--}10 \mu\text{g/mL}$ made by the biology laboratory in which the cells were produced, and it falls comfortably within the detection limits of the sensor, however, the shift here is likely to include non-specific binding from other parts in the media, and it is also not from the same grating, so the sensitivity may differ. Furthermore, since this is a measurement of the IgG secreted into the media from all cells, it is expected that the local concentration of IgG around individual cells will be higher than this value, depending on diffusion rates of IgG in the media, and, importantly, the rate of IgG production is not known at this point.

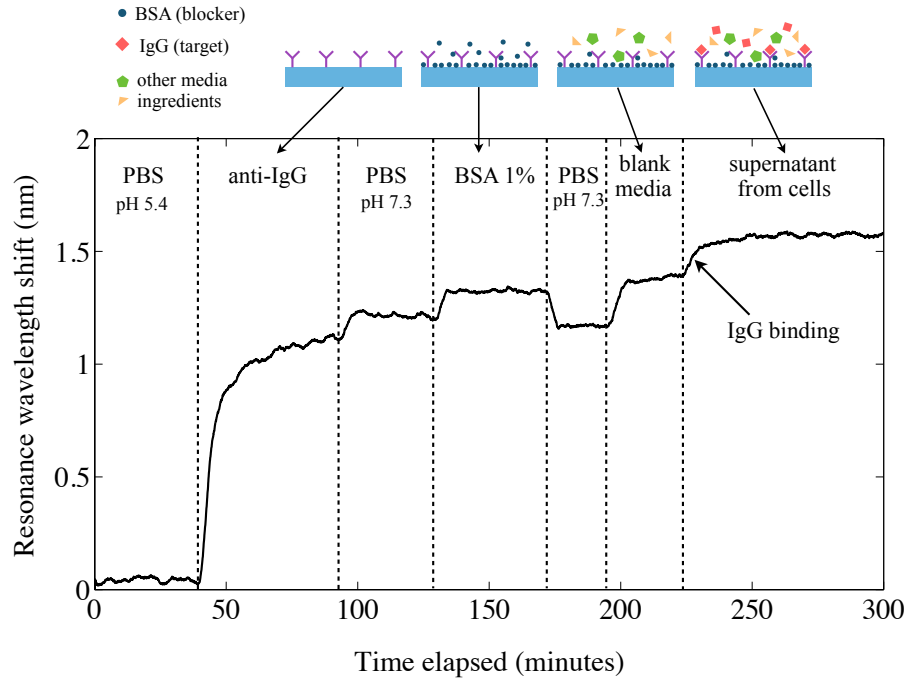


FIGURE 6.9: Resonance wavelength shift measured from the spectrometer during control experiment 1. Here, the concentration of IgG produced by the hybridoma cells is estimated by measuring the supernatant from the cell culture. The "blank" solution used here is fresh culture medium, exactly the same as that used for the cells. The curve is smoothed using a window of 3.75 minutes.

Also noteworthy is the small shift caused by the blank media. This indicates that there is non-specific binding due to components in the media.

6.5.2.2 Control experiment 2

The second control experiment is also essentially a repeat of the IgG binding assay shown in chapter 4, except the resonance shift is now measured by monitoring resonance images in real time instead of collecting spectra directly from the spectrometer, thereby addressing the third point in the list. A valuable inclusion here is a reference region on the sensor, which is positioned within the ROI used in the resonance imaging. To realise this, a piece of PDMS was placed (not bonded) over a portion of the grating to shield it during functionalisation. Thus, there are no antibodies immobilised on this region. The PDMS forms a reliable watertight seal, and is very easily peeled off after antibody immobilisation is complete, and before the rest of the assay proceeds. However, the PDMS does begin to chemically bind to the sensor if it is left in situ overnight, leaving behind a patchy film when it is peeled off. Therefore, it is important to minimise the time for which the PDMS is in contact with the grating. Figure 6.10 depicts an illustration and results of control experiment 2.

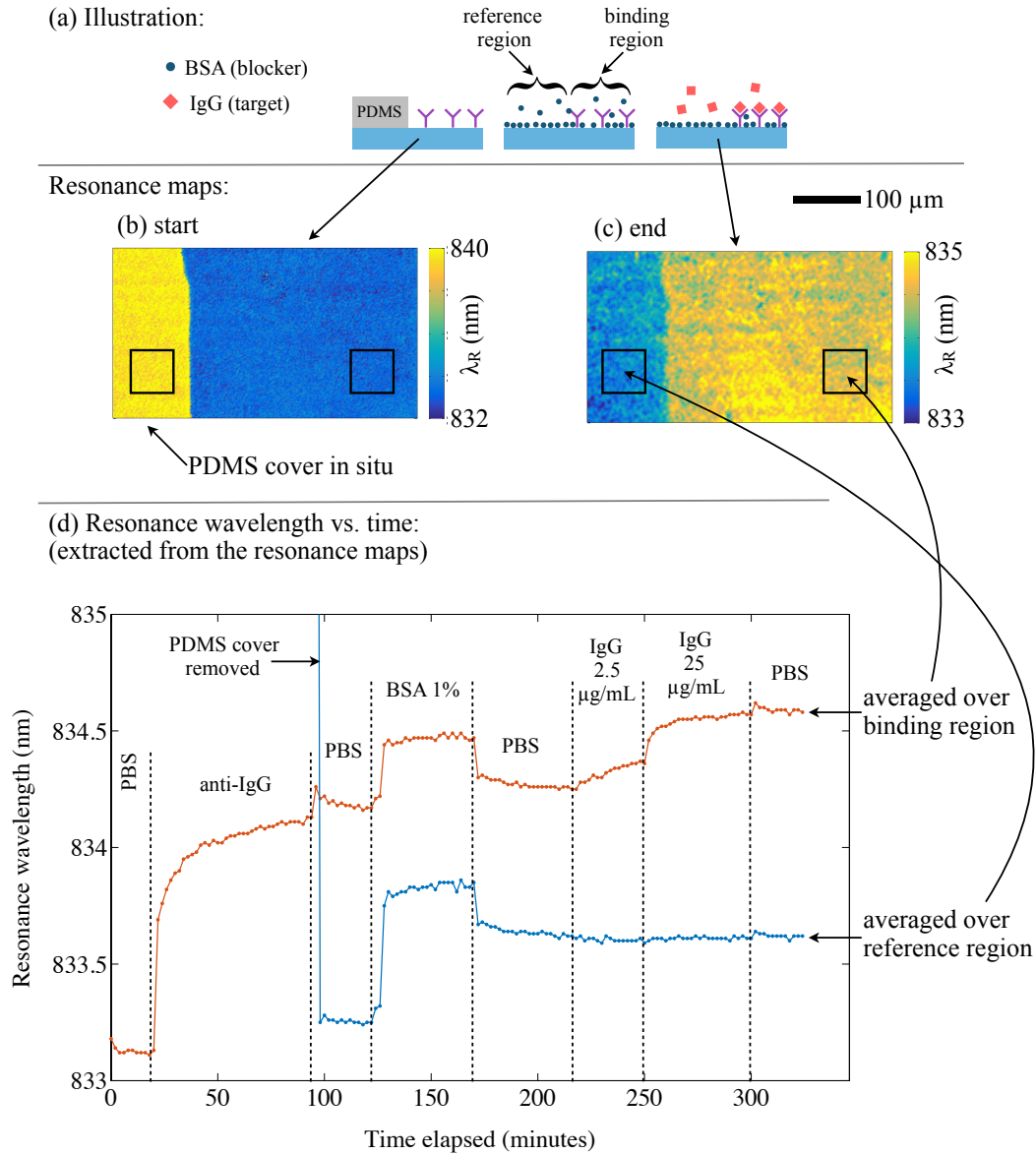


FIGURE 6.10: (a) Illustration of control experiment 2, showing the creation of a reference region by preventing antibody binding with a PDMS shield; (b) Resonance map obtained at the start of the assay, with PDMS still in place at the left hand side, causing a large shift in λ_R ; (c) Resonance map obtained at the end of the assay, showing the right hand side with an increased λ_R due to IgG binding. Note the smaller range of the colour bar compared to that in (b); (d) Plot of λ_R versus elapsed time, where the data is averaged over each ROI indicated in the resonance maps. A resonance map (and thus one data point on each curve) has been obtained every 2 minutes, with the blue curve corresponding to the reference region (i.e. covered during antibody immobilisation), and the red curve corresponding to the binding region.

The data extracted from the resonance maps shown in figure 6.10(d) shows a rich picture of what is happening at specific locations on the sensor surface. During the first ~ 100 minutes, the PDMS cover is kept in place on the left side of the sensor to create the reference region (blue curve) while antibody immobilisation occurs on the right side (red curve). As seen from the blue curve, the high refractive index of the PDMS causes λ_R to exceed the y-limit of the graph, but once it is removed λ_R returns to a value close to the starting point

of the red curve. The reason for not returning to exactly the same value as the red curve stems from the fact that each ROI has a slightly different resonance wavelength to begin with due to fabrication variation. After washing with PBS, the blocking step is carried out, again using 1% BSA in PBS. Both regions exhibit a significant shift due to the higher refractive index of the BSA solution, and after washing again with PBS it is evident that blocking has been successful. In particular, there is a much larger shift caused by BSA on the reference region because the free binding sites here are not occupied by antibodies; comparing the size of the shifts, there are ~ 4 times more non-specific binding sites on the reference region. After the blocking and establishing a stable baseline with PBS, the IgG solutions are introduced: first $2.5 \mu\text{g/mL}$, followed by $25 \mu\text{g/mL}$. Both concentrations are easily detected on the functionalised region (red curve), with the $2.5 \mu\text{g/mL}$ concentration being more relevant to the concentration released by the hybridoma cells. As expected, there is no detection on the reference region (blue curve), highlighting that the IgG binds only to the antibodies, and that the blocking has been very effective. A final wash with PBS confirms that binding has been successful, since the resonance wavelength remains constant.

6.5.3 Main results: cellular secretion

Having now demonstrated the control experiments, I turn to the real measurement of cellular secretion of IgG directly from the cells, *in-vitro*, using the sensor as an imaging tool. I used the same assay as that shown in control experiment 2 above, but after blocking, instead of adding stock IgG solutions, the cells are added to the petri dish and allowed to settle down to the sensor surface. Figure 6.11 shows the results of the experiment.

6.5.4 Discussion

There is much information to digest from the results shown in figure 6.11, as well as from both control experiments shown previously. Firstly, there is clear evidence of a larger shift on the right hand side (the binding region) of the resonance map in figure 6.11(b). This suggests that there is some specific binding to the antibodies here, as any non-specific binding would be expected to also appear on the reference region at the left. There is, however, some evidence of a small resonance shift on the reference region. It is also clear that the resonance increase across the binding region is highly heterogeneous. This suggests that the binding is not due to IgG in the media, as this would be expected to lead to an isotropic shift across the whole binding region. Furthermore, by comparing the highest resonance shifts measured here ($\sim 0.6 \text{ nm}$, the red/orange regions in the map) to those measured for the stock IgG solutions in chapter 4 (again assuming the same sensor and binding response) I roughly estimate *local* IgG concentrations of up to $\sim 24 \mu\text{g/mL}$. This is consistent with the lower value of $\sim 7 \mu\text{g/mL}$, estimated in control experiment 1, where the "bulk" concentration of IgG was measured from all the cells. The localised resonance shifts are consistent

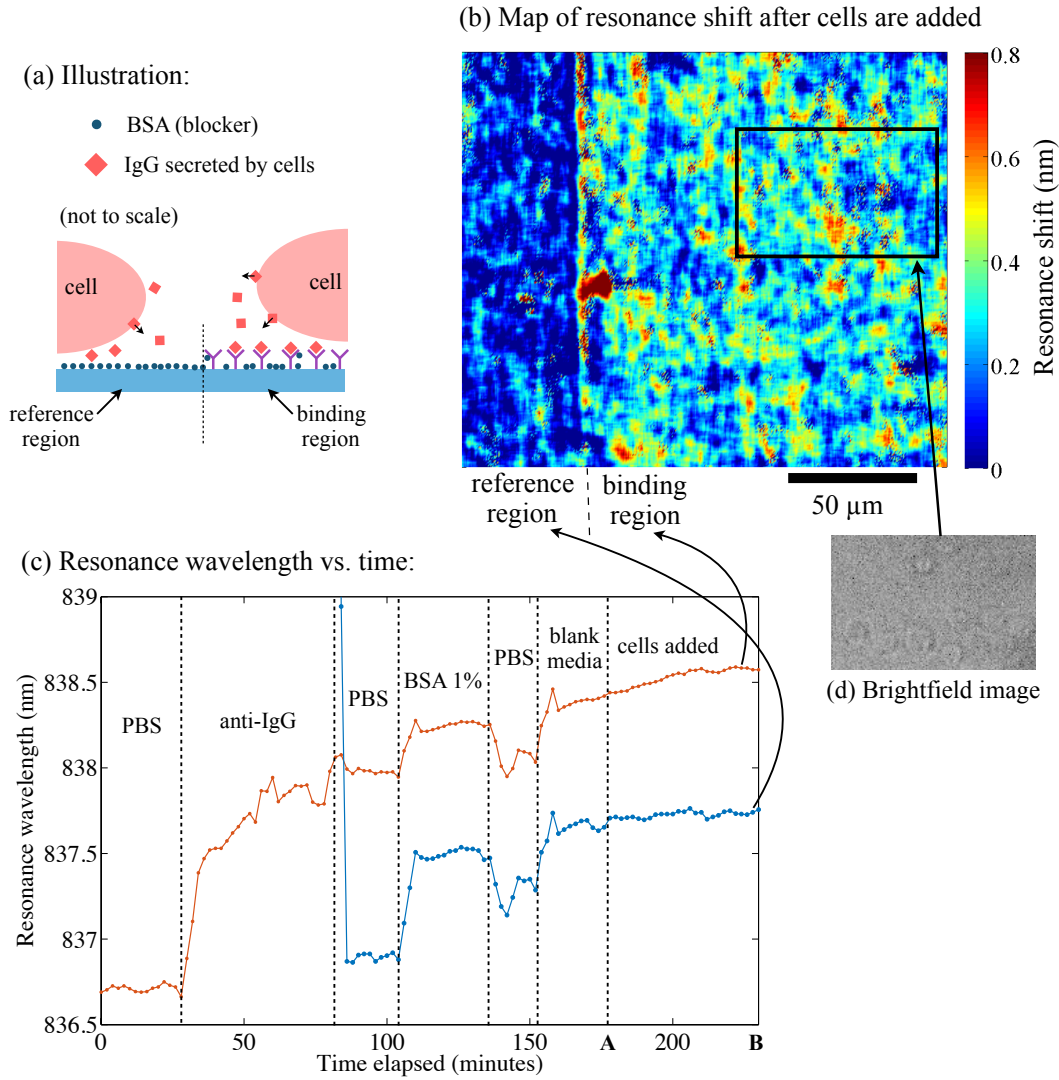


FIGURE 6.11: (a) Illustration of the cellular secretion experiment (not to scale), showing cells situated on the "reference" and "binding" regions; (b) Resonance map showing the *shift* in λ_R after the cells have been introduced to the sensor. Specifically, this map shows the difference between the final image (B) and the time when the cells are added, indicated by points B and A, respectively, in the graph of (c). A noise filter has been applied to this resonance map, using a window of 7x7 pixels. (c) Graph showing resonance wavelength, averaged over the reference region (blue curve) and the binding region (red curve). These curves have been smoothed using a window of 6 minutes in order to reduce experimental noise; (d) Brightfield image corresponding to the indicated region on the resonance map, with cells (just) visible.

The scale bar is relevant to both the resonance map (b) and the brightfield image (d).

with the presence of higher concentrations of IgG in the vicinity of the cells, but whether this shift is directly due to the binding of secreted IgG is still debatable. The hybridoma cells used here are cultured in suspension - they do not readily adhere to the substrate, unlike the COS7 and B104 cells shown previously. Instead, they settle under gravity to the bottom surface of the petri dish without fixing down. For this reason, it is difficult to discern any resonance shift due to the cells in the map. In contrast, for the case of strongly adherent cells, such as those shown in figure 6.6(a), the cells were easily seen in the resonance map. Still, it is possible that the hybridoma cells exhibit IgG molecules that are

bound to their surface, and these are perhaps linking the cells to the functionalised sensor, causing a localised shift in the binding region. Unfortunately, the correlation between the brightfield image (figure 6.11(d)) and the resonance map is not very clear. Although some cells can be seen in the brightfield image, they do not directly correspond to the resonance shifts seen in the map. This could be due to cell movements, irregular attachment of cells to the binding region, or even due to anisotropic secretion of IgG from the cells. By analysing sequential brightfield images, it can be seen that the majority of cells remain in the same location for the duration of my experiment (~ 1 hour), however there are some "loose" cells that drift across the field of view. These cells may also contribute to the anisotropy of the resonance map.

With regard to the future directions of this experiment, there are certainly opportunities for improvements. With hindsight, it would be useful to label the cells with a fluorescent tag. Although this goes against the label-free ethos of my work, it would enable the locations (and thus movements) of the cells to be determined much more clearly. Nearly any fluorescent label could be used, since the excitation and emission wavelengths would likely be much lower than the 840 nm light used for the resonance imaging. Alternatively, a phase-contrast system could be employed to capture more detailed images of the cells, if it is desirable to remain label-free. If cell movement does prove to be an issue, encasing them in a permeable gel such as agar could be an alternative. This would hold the cells in place while allowing secreted molecules to access the binding sites on the sensor. Another approach would be to introduce optical tweezers as a method to physically trap the cells at a single location. Because the setup required for resonance imaging is relatively simple (especially the reflection-based setup), the space above the resonant surface is completely unrestricted. Therefore, an optical trap could very plausibly be added, in a similar fashion to a Raman spectroscopy setup with combined optical trap [159]. Along these lines, it may also be feasible to marry the resonance imaging technique with other forms of microscopy, such as light sheet imaging (SPIM), for instance. As mentioned previously, the excitation and emission wavelengths associated with fluorescence microscopy do not interfere with the resonance imaging wavelength, so these measurements could be performed simultaneously.

6.6 Summary

This chapter has showcased the performance of the resonant grating sensor by applying it to measure real biological systems. In particular, information about the growth of a biofilm has been studied, giving insight into biofilm behaviour and potential providing a new testing ground for antimicrobial treatments that could benefit many healthcare, environmental and industrial areas. Also, extensive demonstrations of cell measurements have been presented, highlighting the greater contrast available without the use of fluorescent markers, and the ability to provide sensitive information on cell attachment. Finally, the

ability to image the binding of a biomolecule after it has been secreted from cells has been thoroughly explored, potentially opening up this sensing technology to a many areas in cell biology, drug development, immunology and more.

Chapter 7

The chirped grating biosensor

7.1 Introduction

Optical biosensors already make up a rich and valuable toolkit for biomedical diagnostics. The advantages of being label-free and exquisitely sensitive are key to this success, while the mass-manufacturability of photonic structures is economically very attractive. Notable commercial examples are the Maverick[™] system from Genalyte [4], based on multiplexed microring resonators, and the Biacore[™] system from General Electric [2], based on surface plasmon resonance (SPR). Other high performance devices include photonic crystals [6], fibre Bragg gratings [160] and resonant gratings such as those presented in this thesis. All of these sensors operate by monitoring a narrow spectral resonance as the refractive index is altered by biomolecular binding. Hence, accurate readout of the spectral shift normally requires some external tool such as a monochromator or spectrometer. This adds significantly to the size, complexity, and cost of the sensor system and can confine its use to a laboratory with trained users: the so-called “chip-in-a-lab”. The challenge, therefore, is to develop a biosensor that is truly stand-alone, robust, low cost and that can be used in the field with minimal training.

A number of solutions have been developed to tackle this challenge in an effort to push towards a true lab-on-a-chip technology. For a comprehensive review of different lab-on-a-chip technologies based on integrated optics, I refer to Estevez et. al. [20]. More recently, many authors have also aimed to interface a photonic sensor with a smartphone [161, 162, 163, 21, 164, 165]. In this case, the spectral readout can be accomplished via a prism or a grating, to disperse the information onto the camera, thereby simplifying operation and removing the need for an external instrument. However, to achieve sufficient spectral resolution, long optical path lengths are required, leading to bulky attachments. While there are certainly advantages to making use of the built-in camera and light source of a smartphone, the issue here is the cost of manufacturing a bespoke cradle, especially since high performance CMOS cameras can be purchased for a few US\$. Moreover, since

optical alignment is critical for the instrument readout, there remains the potential for user error and mis-alignment, especially if the device is to be used in the field.

My research on resonant gratings has led directly to the development of a compact, low-cost, fully stand-alone sensor with the ability to detect biomarkers at concentrations down to ng/mL. Although there are recent examples of stand-alone battery-operated photonic sensors [165, 166], the key feature here is a chirped grating element that not only generates the resonance signal but also translates the spectral information into spatial information using the same chip, thus removing any need for dispersion or wavelength scanning. Read-out is done simply by recording the pixel intensity and position using a basic camera and a monochromatic light source. A similar chirp idea has been presented by Kunz et al. [167, 49], where two chirped grating couplers are positioned side-by-side at either end of a waveguide layer. Here, a change in refractive index causes a change in position of the output beam from the final coupler, that goes on to illuminate a detector array. This chirping concept is applied to a resonant grating for the first time here, resulting in a chip that requires only direct illumination and collection, both at normal incidence. Moreover, the chip can be easily mass-produced on a large scale, and the remaining parts are basic optical components, allowing the whole device to be constructed very economically. The simple optical layout required results in a sensor that is very compact and rugged, requires no user alignment, and is simple to use.

This chapter begins with the details of the chirped grating, before moving on to the details of the construction of the sensor as a whole. Its sensing performance is demonstrated by measuring the response to glucose solutions, followed by a successful assay to detect the binding of a biomarker to the functionalised sensor. Finally, I discuss the potential of the chirped grating idea to realise high-speed resonance imaging.

7.2 Design and fabrication details

The fabrication details of the chirped grating are, for the most part, identical to those covered in chapter 3, where I explained the steps involved in fabricating a basic grating in a 150nm thick silicon nitride layer. The starting structure for the chirped grating presented here is also the same as before, namely a period of $a = 560$ nm and a filling factor of $FF = 70\%$. As shown previously, this structure supports a narrow guided mode resonance when excited with TM polarisation, at a wavelength (for water) of approximately 840 nm. At resonance, the large mode overlap into the region surrounding the grating causes the resonance wavelength to shift upon a refractive index change. Usually, this spectral shift is measured by tracking the resonance wavelength via a tuneable source or a broadband source with a spectrometer. Here, however, the spectral information is obtained by chirping

the grating, i.e. by changing the resonance wavelength as a function of position on the chip.

In order to chirp the resonance wavelength (λ_R), changing the grating period is the most obvious parameter, since the period is directly proportional to λ_R (as seen in figure 2.5(a) of chapter 2). However, this approach is limited by the finite step size of the exposure grid of our electron-beam lithography system. By using the smallest grid size (1.0 nm), λ_R can be tuned in steps no smaller than $\Delta\lambda_R = 1.25$ nm. This value is obtained by analysis of the resonance map from a period-chirped grating and confirmed using RCWA simulations, and is discussed in detail in the next section (7.2.1).

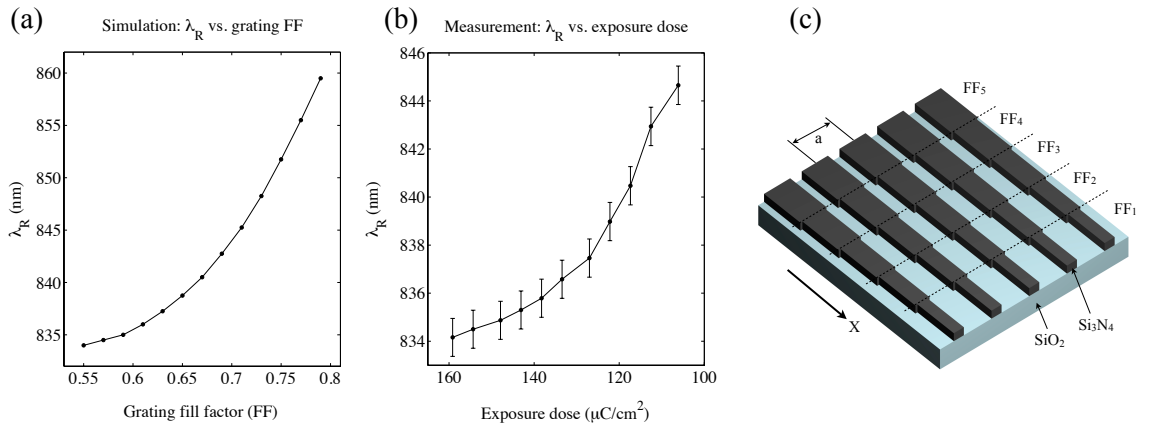


FIGURE 7.1: (a) RCWA simulation showing resonance wavelength dependence on grating FF; (b) measured dependence of resonance wavelength on electron exposure dose. Error bars indicate the spectral resolution of the spectrometer used for the measurement. (c) Chirped grating design. Each strip has a different FF in order to chirp the resonance wavelength as a function of position in X (not to scale).

Instead, I tune λ_R by altering the fill-factor (FF) of the grating via electron exposure dose. This lithographic tuning technique, not being constrained by the exposure grid, affords much finer tuning down to steps as small as $\Delta\lambda_R = 55$ pm (also discussed in section 7.2.1). Figure 7.1(a) shows the simulated dependence of λ_R on grating FF, obtained using RCWA simulations, while 7.1(b) shows the measured dependence of λ_R on exposure dose for several real gratings. Exposure dose and grating fill factor are inversely proportional: a higher dose causes more electron scattering, effectively causing a larger area to be exposed, resulting in a smaller FF. For this reason, the x-axis in figure 7.1(b) is reversed to aid comparison to figure 7.1(a). The simulated and measured data show excellent agreement in terms of the shape of the curve, with both closely following a non-linear relationship. The physical origin of this non-linear behaviour between λ_R and FF is due to the non-linear dependence on the effective index of the grating layer (n_{eff}), and can be seen in figure 1.5(b) of chapter 2 for values of FF > 60%.

The chirped grating itself is then composed of individual grating strips, each with a different FF, and thus λ_R , as illustrated in figure 7.1(c). The gratings are stacked in the X-direction, i.e. perpendicular to the grating vector, which is oriented in the Y-direction. This arrangement affords tighter stacking and less cross-talk between grating strips, because the resonant mode oscillates only in the Y-direction and not in X [129], as was discussed extensively in chapter 5. The chirped grating presented here was fabricated with each strip having a width of $6 \mu\text{m}$ (X) and a height of $500 \mu\text{m}$ (Y), although they could be made significantly smaller in the Y dimension to allow further miniaturisation if desired. Furthermore, the grating could even be chirped along both X *and* Y to provide an additional degree of information.

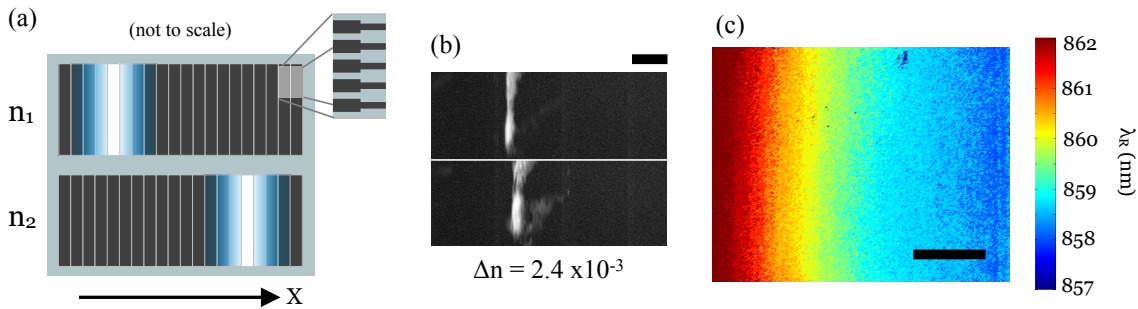


FIGURE 7.2: (a) illustration and (b) experimental example of the resonance shift upon refractive index shift. Scale bar = $100 \mu\text{m}$; (c) resonance wavelength map of the grating (water is the surrounding liquid). Scale bar = $100 \mu\text{m}$.

The response of the grating to different refractive indices is illustrated in figure 7.2(a). For a given refractive index n_1 (or biomarker concentration c_1), the resonance is located at position X_1 , while for n_2 (or c_2) it occurs at X_2 , and so on, as long as the illumination wavelength is kept constant. Figure 7.2(b) shows an experimental example of this, where a detectable shift is seen for a refractive index change of 2.4×10^{-3} RIU. Here, the illumination source is a VCSEL operating at 854.2 nm .

In order to characterise the chirped grating after fabrication, a resonance map can be measured as shown in figure 7.2(c). This is obtained in the usual way as discussed in previous chapters: sweeping the illumination wavelength while collecting brightfield images to acquire the spectral response of each pixel. Analysis of this map allows every position on the sensor to be correlated with a resonance wavelength in nm (for a given refractive index).

7.2.1 Comparison and limits of tuning methods

Before moving on to experimental results from the chirped grating, I first study the tuning methods in detail. To fully investigate the capability of tuning λ_R via the exposure dose, and to compare this with tuning via the grating period, I analyse three chirped gratings: a

period-chirped grating and two dose-chirped gratings; one with 0.5% dose steps and another with 0.1% dose steps. Resonance maps are measured for each grating and are presented as insets in figure 7.3.

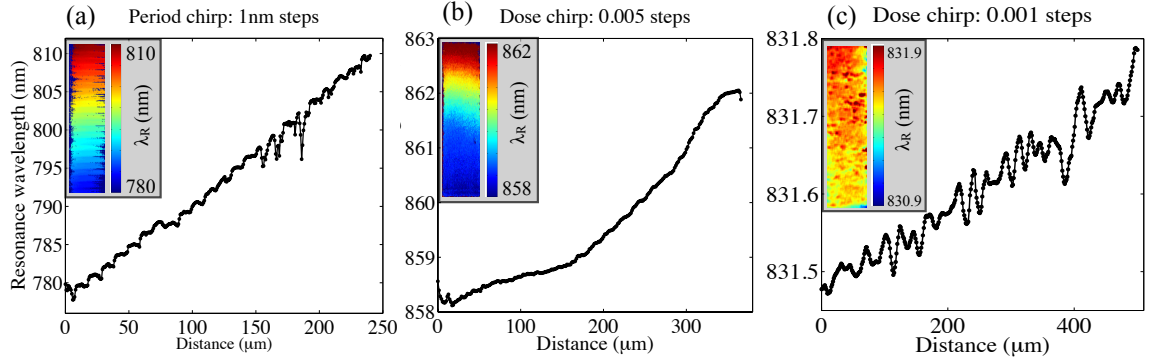


FIGURE 7.3: Resonance maps and graphs of chirped gratings for (a) period tuning and (b,c) dose tuning.

The grating in figure 7.3(a) is composed of 24 individual strips, with the period ranging from 500 nm to 523 nm in steps of 1 nm (the smallest available with our system). The total resonance shift is 30 nm, meaning the smallest possible step size I can achieve with period-tuning is $\Delta\lambda_R = 1.25$ nm. To confirm this experimental value, I used RCWA simulations to generate the dependence of λ_R on grating period, a , finding the linear relationship: $\lambda_{R,sim}(a) = 1.40a + 80\text{nm}$. The slope of this curve is similar to the measured value of λ_R . Although the grating strips are designed without gaps, there are clear dislocations in the resonance map. I suggest that these are caused by the fact that the period is changed discretely, not smoothly, resulting in dislocations between the grating ridges that are a significant perturbation to the resonance wavelength.

Figure 7.3(b) shows a dose-chirped grating composed of 61 strips where the exposure dose ranges from 90% to 120% in steps of 0.5%. The total shift in resonance here is 3.8 nm yielding a much smaller step in resonance wavelength of $\Delta\lambda_R = 129$ pm (average). Changing the exposure dose to this extent clearly causes a non-linear change in resonance wavelength. I propose that this is predominantly due to the non-linear relationship seen in figure 7.1(b), but may also include the influence of proximity error. Proximity error is not present in figure 7.1(b) because the gratings are completely separate, but for the device shown in figure 7.3(b) each grating is immediately next to its neighbour and therefore receives a dose increase from the scattered electrons during the exposure of nearby gratings. Thus the actual delivered electron dose increases non-linearly even though the target dose is set to increase linearly. It is worth noting here that the non-linear change in λ_R could easily be cancelled out by designing the dose to compensate for the curve in figure 7.1(b), and also by including proximity error correction.

The limit of dose-tuning depends on the physical limitations of the column in the electron beam lithography system. The parameters of importance here are the beam current, which is controlled in our system by setting different beam aperture sizes, and the beam dwell time, which specifies how long the beam exposes each point in a pattern. These parameters determine the number of electrons (i.e. the electron dose) that is applied during the exposure, and it is at a minimum when the beam current and dwell time are as small as possible. The current is limited to the smallest beam aperture we have, while the dwell time is limited by the speed of the computer (more specifically, the DAC card) that controls the beam movements and the beam blander, and is 5 ns for our system. With our column set to the smallest beam aperture (30 μm), the beam current is low enough (~ 96 pA) to permit a change in dose of just 0.1% without reaching the dwell time limit. Figure 7.3(c) shows a grating made of 49 strips using such a 0.1% dose change. The total resonance shift is 316 pm, giving a theoretical step of $\Delta\lambda_R = 6.4$ pm. This is impressive, but the noise becomes clearly noticeable at this scale. I therefore estimate the limit of $\Delta\lambda_R$ to be 3 times the standard deviation from a fitted line through the data shown in figure 7.3(c). The standard deviation from this line is measured to be 18.2 pm, so the smallest possible resonance wavelength step when using exposure dose as the tuning parameter is $\Delta\lambda_R \approx 55$ pm.

Finally, to compare the different tuning methods, figure 7.4(a) shows a plot of the resonance shift versus distance along the grating for all three methods (period and dose at 0.5% and 0.1% steps). The slope of these lines is clearly very different depending on the tuning method, and to show this more clearly, figure 7.4(b) shows the same data on a log scale. This reveals that the different methods have approximately one order of magnitude difference in their tuning "sensitivity", thereby unlocking three different tuning ranges: $10^2 \rightarrow 10^0$ nm, $10^0 \rightarrow 10^{-1}$ nm, and $10^{-1} \rightarrow 10^{-2}$ nm.

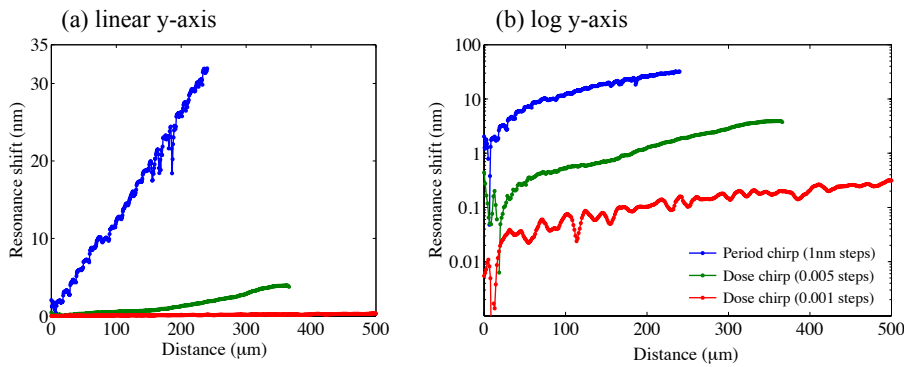


FIGURE 7.4: (a) plot of resonance wavelength shift versus distance along the chirped grating for the three different tuning methods: period (blue), dose at 0.5% steps (green) and dose at 0.1% steps (red). (b) shows the same data with a log scale on the y-axis.

7.2.2 The completed sensor

So far, I have concentrated on the fabrication and performance of the chirped grating element itself. While this is the most important component of the sensor, it is important to consider how it can be packaged with simple optical components in order to provide a fully stand-alone biosensor capable of operating in the field. Although the following details show the first-generation prototype, it is already compact enough to fit into a small plastic container (10 x 10 x 20 cm) and can be fully controlled remotely using a micro-PC. There are still many aspects that could be further miniaturised, taking inspiration from the optics in a CD-ROM drive, for example.

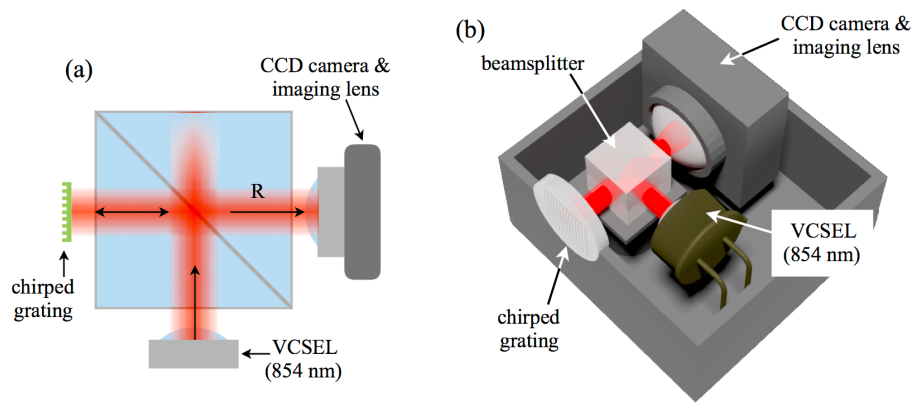


FIGURE 7.5: (a) Schematic of the sensor configuration; (b) Illustration of the stand-alone sensor contained within a small box. Picture credit: Dr. C.P. Reardon, Physics Department, University of York.

The beauty of the chirped grating approach is that the resonance measurement only requires a monochromatic light source and a camera. No dispersive elements or spectrometer are needed, nor is a tailored interface to a smartphone. This means that no critical optical alignment is required, particularly since the boundaries of the grating can be used to calibrate the position of the resonance. The simple optical layout shown in figure 7.5(a) places the grating, source and camera at the sides of a beamsplitter cube, making it very small, robust and rugged. For the light source, a VCSEL (vertical cavity surface emitting laser) is an ideal choice for minimising size and power consumption. The choice of camera is practically unlimited, with small USB devices providing the smallest footprint and not requiring a dedicated power supply. An advantage of keeping the resonance wavelength fixed is the flexibility in choosing the operating wavelength to best match the camera sensitivity, thereby increasing the signal-to-noise ratio. Both the camera and the light source are controlled by a Raspberry Pi micro-PC, connected to a 5V battery pack, which supplies power to all components.

A further advantage of the chirped grating sensor is the unrestricted space for attaching a microfluidic flow channel. Because the reflected signal is measured from the grating (and

not the transmitted signal), the region above it (the sensing region) may be interfaced to any type of microfluidic platform or liquid delivery system. One such system might be based on paper microfluidics [168, 169], a very cost-effective and user-friendly solution. The position of the grating chip on the outside of the sensor also makes replacement simple, although, owing to the hardness and chemical resistance of silicon nitride, the chip can withstand multiple uses and cleanings before replacement is necessary.

For the proof-of-concept experiments shown in the coming sections, I measured the chirped grating resonance using the reflection setup, in combination with my tuneable monochromatic source, both detailed in chapter 3. This provided some flexibility in selecting the exact illumination wavelength to match the fabricated gratings. The microfluidic chamber used was that described on the left side of the table in figure 3.1 (chapter 3).

7.3 Sensitivity measurement using glucose solutions

To investigate the sensitivity of the chirped grating biosensor, I measured the response to glucose solutions of different concentrations. A glucose concentration range from 0% w/v to 10% w/v yields a refractive index range of 1.333 to 1.345 [101]. The results are presented in figure 7.6.

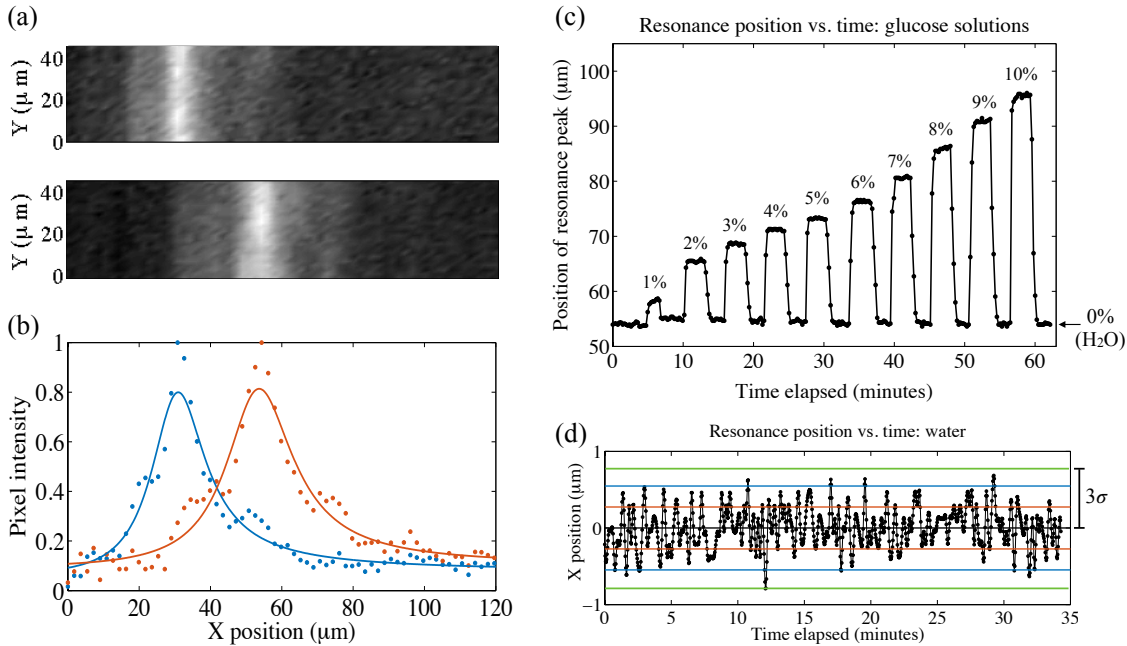


FIGURE 7.6: (a) brightfield images of the resonance for two different glucose solutions; (b) averaged pixel intensity profiles from the images in (a), and fitted Fano curves; (c) evolution of peak position as different glucose solutions are pumped in; (d) peak position versus time for the 0% solution, centred about the mean. Red, blue and green dashed lines show \pm one, two and three standard deviations, respectively.

As the sugar solutions are introduced, brightfield images are collected from the camera, showing the resonant strip (figure 7.6(a)). In particular, an image was taken every 5 seconds while glucose solutions were pumped into the fluidic chamber in concentration increments of 1% w/v, although image acquisition rate is limited only by the camera/PC speed, and can therefore be carried out at much higher speeds than the resonance imaging shown in the previous chapters. The X-profile of the image is averaged vertically before a Fano curve is fitted to the data in order to extract the peak position. Figures 7.6(a,b) show the images and profiles with fitted curves for two different glucose concentrations. Monitoring this peak position over time produces the graph shown in figure 7.6(c). Water was introduced between each glucose solution to verify that it returns to a constant baseline.

From the data in figure 7.6(c), the average *positional* shift per RIU is $3469 \mu\text{m}/\text{RIU}$. This value should not be compared with the more conventional nm/RIU sensitivity since this is a measurement of position and not resonance wavelength. Indeed, the wavelength remains fixed here so the usual figure of merit is inappropriate. Nevertheless, I have already measured the sensitivity of identical gratings (not chirped) with glucose solutions (chapter 4), resulting in a value of $137 \text{ nm}/\text{RIU}$ for this resonance (the TE mode). It is a sensible assumption that the sensitivity is approximately the same across the entire chirped grating, and this has been verified using RCWA simulations where the difference in nm/RIU between gratings with fill factors 65% and 85% is just 1.3%.

To estimate the detection limit, I postulate that the smallest observable positional shift is 3 times the standard deviation in position for a constant refractive index solution flowing at the same rate as that used in the experiment. This was measured over ~ 35 minutes for 0% (water) to be $0.821 \mu\text{m}$, and the data is shown in figure 7.6(d). Dividing this by the average positional sensitivity ($3469 \mu\text{m}/\text{RIU}$) gives a limit-of-detection of $\text{LOD} = 2.37 \times 10^{-4} \text{ RIU}$. The noise that sets this limit is probably due to mechanical vibrations of the measurement setup, originating from various sources including the fluid flowing over the sensor, and there are various ways to reduce this and improve the LOD. Further improvements would come from using a narrower source linewidth or by chirping the grating with an even finer dose variation. Nevertheless, this value compares well to other photonic crystal biosensors in the literature, and is sufficient to detect ng/mL concentrations of biomarker binding, as shown next.

7.4 Demonstration of IgG binding

Having demonstrated the sensitivity of the chirped grating to refractive index changes using glucose solutions, I now show the capability of detecting the binding of a target antigen;

here we use immunoglobulin G (IgG), as was shown previously for a normal resonant grating. The detection assay shown here may be adapted, as usual, to enable the detection of any antigen for which there is an available antibody - it is not specific to IgG detection. The protocol used for functionalising the grating with antibodies specific to the target molecule is the same as discussed in section 4.5 of chapter 4, but any type of immobilisation protocol may be used. I recap the procedure briefly now: Firstly, the Si_3N_4 grating is cleaned and hydroxylated in piranha solution. Next, a surface silanisation step is done using APTES ((3-Aminopropyl)triethoxysilane), leaving free amine groups to which antibodies are cross-linked using the NHS-EDC chemistry (chapter 4). The chip is then encapsulated in the PDMS flow channel to allow the antibody binding process to be observed in real time before monitoring the subsequent binding of IgG at different concentrations. The antibody immobilisation could easily be carried out in a separate step without monitoring (overnight for example) to maximise the number of binding sites.

The binding curve is shown in figure 7.7, and was measured in the same way as that in figure 7.6(c) for the glucose solutions where the y-axis shows the position of the resonance peak. An initial baseline was established using PBS at a pH of 5.4 before the introduction of anti-IgG combined with NHS-EDC. There is a clear shift during the antibody binding phase, with saturation after ~ 2 -3 hours. Next, a blank PBS solution at pH 7.3 was flushed through to establish a baseline before introducing the IgG solutions, which were prepared using the same PBS (pH 7.3). The final two concentrations are clearly detected, however it is debatable whether the 250 ng/mL concentration falls within the detection limit of the sensor. The 250 ng/mL curve (inset) shows a rapid 2 μm increase in position at the start (which may be a pressure change caused during changeover of fluids in the syringe pump), but this is followed by a steady increase, indicating binding, however it is below the 3σ noise level demonstrated previously. In contrast, the 2.5 $\mu\text{g}/\text{mL}$ solution shows a much larger shift with some saturation; and the 25 $\mu\text{g}/\text{mL}$ solution shows a clear shift with significant saturation as the binding sites become occupied.

7.5 Potential for video-rate resonance imaging

So far in this chapter, I have emphasised the low cost, small footprint and simplicity of the chirped grating biosensor, showing that it still provides highly sensitive label-free antigen detection and a low LOD. But the chirped grating idea has another exciting application that I introduce briefly now: the possibility of realising video-rate resonance imaging.

By fabricating several small "sub-gratings", each with a different resonance wavelength, and then grouping them together, a larger pixel can be made (figure 7.8(a)) within which

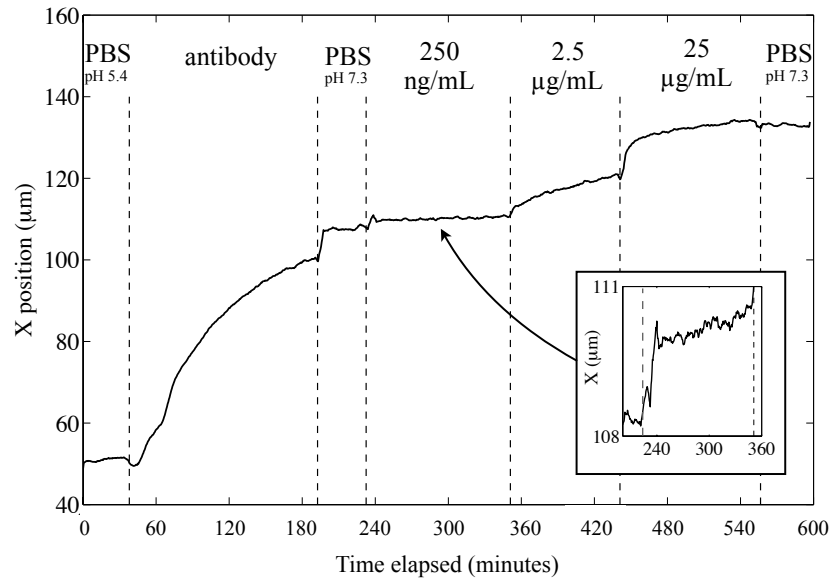


FIGURE 7.7: X position of the resonance on the chirped grating as the IgG binding assay proceeds.

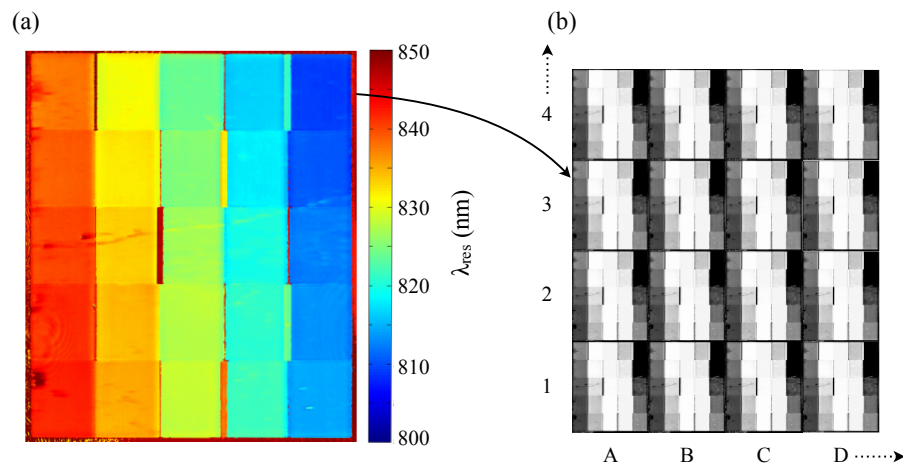


FIGURE 7.8: (a) Resonance map showing one pixel made up of individual sub-gratings, each with a different resonance wavelength. Each sub-grating is $100\mu\text{m}^2$. This is a large-scale test pixel that could be miniaturised then arrayed to form the final sensor, as shown in (b) (illustration only). Resonance information for each pixel (A1, A2, etc.) would be read off as the position of the brightest sub-grating within that pixel, when illuminated with monochromatic light.

the resonance wavelength is read off as a position. Arraying these pixels to form the sensor surface (figure 7.8(b)) allows a resonance image to be obtained solely from a single brightfield image taken with monochromatic illumination. This contrasts with the resonance images demonstrated up until now, where it was necessary to scan the illumination wavelength in order to identify the resonance at each pixel, resulting in an acquisition time of ~ 20 seconds. This is not an issue during the imaging of, for example, cell movement, secretion (from certain cells), or molecular binding as these events typically take place on a timescale of minutes. But there are a great number of biological processes that take

place on much shorter timescales. For example, the electrochemical secretion of neurotransmitters at a neuronal synapse occurs on a timescale of milliseconds [170]. While it is possible to perform a "before and after" measurement, studying such changes in real time requires much higher temporal resolution and can only be done if a faster acquisition time is achieved. With the arrayed chirped grating described here, resonance imaging could be realised at video rate, potentially opening up resonance imaging technology to the measurement of many high-speed biological events. This would be a powerful and novel development in the community, where all the systems demonstrated so far have involved sweeping illumination wavelength or angle, or by line-scanning spatially across the grating using an imaging spectrometer, with typical acquisition times of at least a few seconds. I believe my research into the use of chirped gratings for imaging has laid the foundations for much faster acquisition rates to be realised in the near future.

The trade-off for the speedup in image acquisition time is a larger pixel size and therefore larger spatial resolution, although the resolution could still be kept in the range of tens of μm . The main limiting factor for pixel size is the number of grating periods required to support a resonance. For the best resolution, the sub-grating size must be made as small as possible while still being resonant, allowing the overall pixel size to be minimised. To this end, I have carried out basic FDTD modelling to investigate the spectral dependence of the resonance on the size of the grating (i.e. the number of periods), with results shown in figure 7.9(a). As expected, the resonance Q-factor increases as more periods are included, until the propagation length of the resonant mode is no longer being restricted by the finite grating size. I employed MEEP for the modelling reported here, using a model similar to that shown in section 5.4.3 of chapter 5 on spatial resolution modelling.

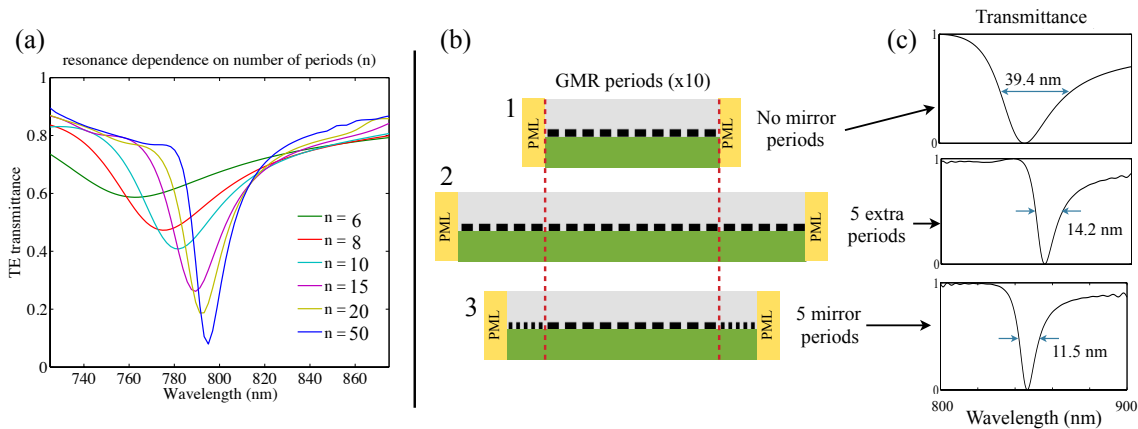


FIGURE 7.9: (a) Transmission spectra showing dependence of the resonance on number of periods included in the grating; (b) Drawings of the gratings used in the modelling; (c) the resulting transmission spectra. Structure details: (1) 10 periods of the standard GMR grating; (2) 5 additional ridges either side of the central region, with the same period as that of the main grating; (3) 5 additional "mirror" ridges with an optimised period and FF. Spectra in (c) also show the FWHM of the resonance.

There are also opportunities to improve the spatial resolution through clever design of the sub-grating boundaries. By tailoring the period and FF at the edges of the resonant grating, it is possible to enhance the in-plane reflection of the resonant mode. A similar idea for confining the propagation of a resonant mode has been reported by Mizutani et. al. [171], using doubly-periodic gratings. Again, I studied this with modelling and observed promising results that are presented in figure 7.9(b,c). The mirror regions here (figure (7.9(b,3))) effectively "fold" the propagation back into the central region, enabling the same resonance linewidth to be supported with fewer grating periods. In fact, the FWHM of the resonance in figure 7.9(c,3) is smaller than that in figure 7.9(c,2), even though the mode is more spatially confined. The mirror region has a period of 280 nm, and the FF is 55%. I note that the transmission/reflection efficiency of the resonance is reduced by the addition of the mirror regions. This is because the mirror regions do not effectively couple incident light into the guided mode, since they are not optimised for this role; instead, they are optimised in-plane mirrors. In the figure, I plot the normalised transmission efficiency to compare the resonance linewidths, but the efficiency drops from 67% to 47% from spectra (c,2) to (c,3). The efficiency of structure (c,1) is significantly less at 31%, although the resonance peak can still easily be distinguished from the background.

7.6 Summary

In this chapter, I have presented the development of the chirped grating biosensor. The novel idea to chirp the resonance wavelength as a function of position on the grating allows a spectral measurement to be done using just a monochromatic source and a simple camera. Spectral information is read out as a position on the chirped grating, enabling the construction of a low-cost, stand-alone biosensor that is compact, robust, and requires no user alignment. The fabrication details of the chirped grating have been detailed, including a study into the limits of lithographic resonance wavelength tuning. Despite the inherent simplicity of the sensor, the performance has not been compromised. In particular, a "positional" sensitivity of $3469 \mu\text{m}/\text{RIU}$ has been measured using glucose solutions, along with a detection limit of 2.37×10^{-4} RIU. This value could certainly be further improved down towards $\text{LOD} = 10^{-5}$ RIU by using a light source with a narrower bandwidth, a finer resonance chirp, and by addressing sources of noise in the experiment. The applicability of the sensor for biomedical diagnostics and healthcare has been demonstrated with the detection of the binding of IgG down to low $\mu\text{g}/\text{mL}$ concentrations, and this could plausibly be improved into the ng/mL range. Lastly, the potential role of chirped gratings in achieving high-speed resonance imaging was introduced.

Chapter 8

Conclusions & outlook

To conclude this thesis, the following section provides a summary of the results and findings, what can be learned from these, and discussions on how they could contribute to future work.

In summary, a biosensor is presented based on a silicon nitride grating that exhibits guided-mode resonance at a wavelength of ~ 840 nm. For this grating, there are two distinct resonances for TE and TM polarisations, each having significantly different linewidths and electric field profiles. The sensitivity of the grating resonances to refractive index has been measured using glucose solutions to be 143 ± 3 and 137 ± 3 nm/RIU for the TE and TM modes, respectively. Using these measurements, the limit-of-detection is deemed to be 2.36×10^{-4} RIU, in good competition with other grating-based biosensors found in the literature. This LOD could potentially be improved, down into the 10^{-5} regime, by addressing sources of noise in the experimental setup, or by fabricating the grating layer on a low-index substrate (discussed below). Additionally, in a simple experiment using glass lenses, the penetration depth of the evanescent field has been measured to be 183 ± 14 nm for the TE mode, and 220 ± 13 nm for the TM mode. These measurements are in excellent agreement with simulated models, electric field distributions, and analytical predictions. The in-depth characterisation of the grating was then continued by fabricating a resolution test pattern on top of the resonant grating. This was used to measure the spatial resolution of the grating in terms of resonance imaging, and results showed resolutions of $2\mu\text{m}$ parallel to, and $6\mu\text{m}$ perpendicular to the grating ridges. This asymmetry in spatial resolution is due to the lateral propagation of the guided modes in the grating layer, and is ultimately due to the inherent asymmetry of a 1D grating. The use of a 2D grating, on the other hand, results in symmetric spatial resolution, as is expected, but only if the incident light is unpolarised; for polarised light, the resolution returns to being asymmetric. This is perhaps a surprising result - photonic crystal performance typically scales with dimensionality, but this is not the case here. These ideas are confirmed experimentally with a 2D grating in

the form of a square array of holes. Furthermore, this approach has also enabled an investigation into the dependence of resolution on refractive index contrast, where it is found to decrease at lower contrasts - a result that is again backed up with a simulated model.

In terms of employing the resonant grating as a biosensor, an initial assay was performed to measure the binding of IgG molecules. Using the EDC-NHS method to immobilise anti-IgG antibodies to the sensor, the resonance wavelength is tracked over time, and IgG binding is detected down to a concentration of 500 ng/mL. This is approaching the lowest detectable limit for this sensor, but it is not at the limit. Although the LOD has been measured here in terms of refractive index units (RIU), an important future experiment would be to obtain a concentration curve in order to accurately establish the lowest molecular concentration that can be detected. Another valuable experiment would be to establish the quality of the silanisation process, which is employed to create free amine groups on the sensor surface. As discussed in section 4.5.1 in chapter 4, an amine-reactive fluorescent marker could be applied to the sensor after silanisation, and the fluorescence signal used as a figure of merit to determine the quality of the amine coverage. Furthermore, a grating resonance could be engineered to overlap with the excitation wavelength, boosting the signal-to-noise ratio of this measurement. Using this, the silanisation stage could be optimised. In addition to improvements of the silanisation step, the other stages involved in the EDC-NHS protocol should also be examined in an effort to improve the efficiency of antibody immobilisation.

After thoroughly analysing the performance of the grating biosensor separately in terms of bulk sensing, then in terms of imaging resolution and penetration depth, chapter 6 turned to applying the sensor as a tool for monitoring different biological systems. It was seen that the sensor is particularly suited for analysis of biofilm development, and it would be interesting to take this further by testing the efficacy of antimicrobial treatments that could be applied to the sensor surface prior to any biofilm growth, or applied to mature biofilms. A microfluidic chamber could be fabricated that comprises two separate channels, one receiving the antimicrobial treatment and one as a reference, and resonance images captured showing both regions. This has already been demonstrated in chapter 6 for the binding of IgG molecules to the grating sensor, where a reference region is first created by preventing the immobilisation of antibodies in a specific area. Very promising results came from these experiments, where clear differences between the reference and binding areas can be seen in the resonance images. The *in-vitro* imaging of cells has also been presented, again with conclusive results that show improved imaging contrast, and information about cell adhesion to the surface that is not gained when using conventional microscopic techniques. After having firmly established the sensor as a live-cell imaging tool, the resonance imaging of cellular secretion of IgG was then studied, with a clear indication of binding

onto the sensor equivalent to a concentration of $\sim 24\mu\text{g/mL}$. However, more work is needed to confirm that the measured resonance shifts are indeed from secreted molecules. A first step would be to repeat the experiments reported here. Additionally, a fluorescent label could be applied either to the cells or the target secreted molecules. Although the resonance imaging is label-free, this would be a sensible way to verify that the binding signal is due to secreted molecules from the cells, and it would also enable the exact locations of the cells to be determined. A simple improvement to aid future work on cell-based experiments would be the inclusion of a CO_2 system on the stage incubator. This would allow long-term incubation of cells using standard culture medium. Currently, the incubation stage (shown in figure 6.4) only incorporates heating pads to ensure the sample is kept at 37° , and HEPES-buffered culture medium is required for the experiments. This is possibly detrimental to the health of the cells, but a bigger issue is that they must be transferred from a standard incubator to my stage incubator prior to imaging, and this may shock the cells thermally and in terms of CO_2 levels. Additionally, future experiments should be performed using higher image magnification, if possible, similar to that shown in figure 6.6.

The majority of the experiments presented in this thesis have been undertaken using dedicated optical setups, and a bespoke tuneable monochromatic light source for sweeping illumination wavelength. In an effort to make a miniaturised version of the sensor, a fundamentally different approach was presented in 7. The chirped grating biosensor is a design whereby the resonance wavelength is tuned as a function of position on the chip. To achieve extremely fine tuning across the chip, the electron beam dose was varied slowly, altering the grating filling factor and thus the resonance wavelength. Using this novel fabrication method, the spectral information is encoded spatially on the chip, so there is no need to sweep incidence wavelength to access resonance information. Instead, the resonance is read out as a position that changes with refractive index, requiring only an inexpensive monochromatic light source and a basic CCD camera. This allows the whole device to be packaged very compactly, using just a basic beamsplitter and an imaging lens. Despite its simplicity, the sensor was shown to have excellent sensitivity to refractive index changes with a "positional sensitivity" of $3469\text{ }\mu\text{m/RIU}$, a LOD of $2.37\times 10^{-4}\text{ RIU}$, and it is able to detect the presence of IgG down to low $\mu\text{g/mL}$ concentrations. Now that the chirped biosensor has undergone initial testing, future work should be focused on both applying it in the field and improving the performance. The latter should begin by fabricating a grating with a "finer" chirp, perhaps by performing the lithography with a lower electron beam dosage, as discussed in chapter 7. A promising application for the sensor would be to apply it to the detection of biofilm growth in a real environmental setting such as a water course or pipeline. Alternatively, the sensor could be functionalised to detect specific pollutants or toxins present in the environment. This would require the full encapsulation of the device to ensure it is watertight, but not much further development would be necessary - the

sensor has already been tested under battery power, and used remotely with a Raspberry Pi microcomputer. Detection of biofilm development, toxins, or pollutants could be carried out over a timescale of days, depending on battery lifetime. A sensible addition would be the inclusion of a reference chirped grating alongside the measurement grating, thereby allowing any thermal drift or noise to be cancelled out. With further miniaturisation, the device can be envisaged in healthcare, potentially as an implanted device to detect the presence of disease or infection biomarkers.

A further development for the chirped grating sensor is its potential use in high-speed resonance imaging, where arrays of chirped gratings are used to generate an image. As discussed in chapter 7, the trade-off for fast acquisition time would be a reduction in the spatial resolution, although it could still remain on a scale of 10s of μm . A potential application could be the real-time monitoring of wound healing processes, especially since the sensor could be functionalised with antibodies specific to cell signalling molecules involved with the healing process. It would be extremely valuable to monitor the transportation of such molecules, and also cells, across a wound. This could be performed *in-vitro* initially, but in the future it is plausible that it could be a wearable device to monitor a real wound. On a more fundamental design level, the spatial resolution of the array could be improved by tailoring the boundaries between individual gratings. Also, by chirping the grating along two dimensions instead of just one, a greater level of information could be obtained. Moreover, a cavity-based resonance could be employed, as was shown briefly in chapter 2, which may further enhance the possible spatial resolution.

Lastly, our group has recently established a sputtering system for silicon nitride, so an investigation into the use of different substrates would potentially be very insightful. In particular, a low refractive index substrate such as magnesium fluoride ($n \approx 1.37$) could increase the sensitivity of the grating resonance. Referring to the electric field profiles shown in figure 4.2 (chapter 4), it is clear that the field resides preferentially in the glass substrate, rather than in the sensing region. By lowering the refractive index of the substrate, this field would overlap more into the sensing region, thereby increasing the sensitivity. Further improvements to the sensitivity of the resonance might also be made by considering a 2D grating. Additionally, there is the possibility to investigate deposition of Si_3N_4 onto a flexible substrate. This could open up applications in vibration and temperature sensing, where resonance wavelength shifts are caused by the grating deforming or flexing. A similar effect could be achieved by fabricating the grating on a membrane that is suspended above an air gap in the substrate, as is commonly seen for in conventional photonic crystals.

Bibliography

- [1] J. Homola, S. Yee, and G. Gauglitz, “Surface plasmon resonance sensors: review,” *Sensors Actuators B Chem.*, vol. 54, no. 1-2, pp. 3–15, 1999.
- [2] GE Healthcare, “Biacore Life Sciences,” <https://www.biacore.com/lifesciences/index.html>. Accessed: 2016-02-09.
- [3] X. Fan, I. M. White, S. I. Shopova, H. Zhu, J. D. Suter, and Y. Sun, “Sensitive optical biosensors for unlabeled targets: a review.,” *Anal. Chim. Acta*, vol. 620, no. 1-2, pp. 8–26, 2008.
- [4] Genalyte, “Maverick Detection System,” <http://www.genalyte.com/download/1547/>. Accessed: 2016-02-09.
- [5] J. J. Colás, “(Poster presentation) Electrochemically controlled functionalisation of silicon biosensors,” *Biophotonics 2015 Summer Sch. Sweden*, 2015.
- [6] M. G. Scullion, A. Di Falco, and T. F. Krauss, “Slotted photonic crystal cavities with integrated microfluidics for biosensing applications.,” *Biosens. Bioelectron.*, vol. 27, no. 1, pp. 101–5, 2011.
- [7] L. H. Kuller, R. Tracy, W. Belloso, S. De Wit, F. Drummond, H. C. Lane, B. Ledergerber, J. Lundgren, J. Neuhaus, D. Nixon, N. I. Paton, and J. D. Neaton, “Inflammatory and coagulation biomarkers and mortality in patients with HIV infection,” *PLoS Med.*, vol. 5, no. 10, pp. 1496–1508, 2008.
- [8] M. S. Pepe, R. Etzioni, Z. Feng, J. D. Potter, M. Lou, M. Thornquist, M. Winget, Y. Yasui, and I. Ntroduction, “Phases of Biomarker Development for Early Detection of Cancer,” *Cancer*, vol. 93, no. 14, pp. 1054–1061, 2001.
- [9] J. Cummings, T. H. Ward, and C. Dive, “Fit-for-purpose biomarker method validation in anticancer drug development,” *Drug Discov. Today*, vol. 15, no. 19-20, pp. 816–825, 2010.
- [10] Y. Fang, “Label-free cell-based assays with optical biosensors in drug discovery.,” *Assay Drug Dev. Technol.*, vol. 4, no. 5, pp. 583–595, 2006.

- [11] C. A. Arias and B. E. Murray, "Antibiotic-Resistant Bugs in the 21st Century - A Clinical Super-Challenge," *N. Engl. J. Med.*, vol. 360, no. 5, pp. 439–443, 2009.
- [12] T. Z. Baram and M. Joels, "The neuro-symphony of stress," *Nat. Rev. Neurosci.*, vol. 10, no. 6, pp. 459–466, 2009.
- [13] M. A. Cousin and G. J. O. Evans, "Activation of silent and weak synapses by cAMP-dependent protein kinase in cultured cerebellar granule neurons.," *J. Physiol.*, vol. 589, no. Pt 8, pp. 1943–55, 2011.
- [14] P. Leonard, S. Hearty, J. Brennan, L. Dunne, J. Quinn, T. Chakraborty, and R. O'Kennedy, "Advances in biosensors for detection of pathogens in food and water," *Enzyme Microb. Technol.*, vol. 32, no. 1, pp. 3–13, 2003.
- [15] M. Campas, B. Prieto-Simon, and J. L. Marty, "Biosensors to detect marine toxins: Assessing seafood safety," *Talanta*, vol. 72, no. 3, pp. 884–895, 2007.
- [16] S. Kröger, S. Piletsky, and A. P. F. Turner, "Biosensors for marine pollution research, monitoring and control.," *Mar. Pollut. Bull.*, vol. 45, no. 1-12, pp. 24–34, 2002.
- [17] M. Fischer, G. J. Triggs, and T. F. Krauss, "Optical sensors for sensing microbial life on a surface," *Appl. Environ. Microbiol.*, pp. AEM.03001–15, 2015.
- [18] J. W. Costerton, P. S. Stewart, and E. P. Greenberg, "Bacterial biofilms: a common cause of persistent infections.," *Science (80-.)*, vol. 284, no. 5418, pp. 1318–1322, 1999.
- [19] Thomson Reuters, "Web of Science," *www.webofknowledge.com* Accessed: 2016-04-20.
- [20] M. C. Estevez, M. Alvarez, and L. M. Lechuga, "Integrated optical devices for lab-on-a-chip biosensing applications," *Laser Photon. Rev.*, vol. 6, no. 4, pp. 463–487, 2012.
- [21] D. Zhang and Q. Liu, "Biosensors and bioelectronics on smartphone for portable biochemical detection," *Biosens. Bioelectron.*, vol. 75, pp. 273–284, 2016.
- [22] Reuters, "Research and Markets: Biosensors Market Analysis 2015 By Application, By Technology And Segment - Forecasts to 2020 for the \$21 Billion Industry," *http://uk.reuters.com/article/research-and-markets-idUKnBw025712a+100+BSW20151102*. Accessed: 2016-04-20, 2015.
- [23] B. Lin, J. Qiu, J. Gerstenmeier, P. Li, H. Pien, J. Pepper, and B. Cunningham, "A label-free optical technique for detecting small molecule interactions.," *Biosens. Bioelectron.*, vol. 17, no. 9, pp. 827–34, 2002.

- [24] B. Cunningham, P. Li, B. Lin, and J. Pepper, "Colorimetric resonant reflection as a direct biochemical assay technique," *Sensors Actuators B Chem.*, vol. 81, pp. 316–328, 2002.
- [25] B. Cunningham, B. Lin, J. Qiu, P. Li, J. Pepper, and B. Hugh, "A plastic colorimetric resonant optical biosensor for multiparallel detection of label-free biochemical interactions," *Sensors Actuators B Chem.*, vol. 85, no. 3, pp. 219–226, 2002.
- [26] B. T. Cunningham, P. Li, S. Schulz, B. Lin, C. Baird, J. Gerstenmaier, C. Genick, F. Wang, E. Fine, and L. Laing, "Label-free assays on the BIND system," *J. Biomol. Screen.*, vol. 9, no. 6, pp. 481–90, 2004.
- [27] Y. Fang, "Non-invasive Optical Biosensor for Probing Cell Signaling," *Sensors*, vol. 7, no. 10, pp. 2316–2329, 2007.
- [28] Y. Fang, A. M. Ferrie, N. H. Fontaine, J. Mauro, and J. Balakrishnan, "Resonant waveguide grating biosensor for living cell sensing," *Biophys. J.*, vol. 91, no. 5, pp. 1925–40, 2006.
- [29] Y. Fang, G. Li, and A. M. Ferrie, "Non-invasive optical biosensor for assaying endogenous G protein-coupled receptors in adherent cells," *J. Pharmacol. Toxicol. Methods*, vol. 55, no. 3, pp. 314–322, 2007.
- [30] C. Vannahme, M. Dufva, and A. Kristensen, "High frame rate multi-resonance imaging refractometry with distributed feedback dye laser sensor," *Light Sci. Appl.*, vol. 4, no. 4, p. e269, 2015.
- [31] P. G. Hermannsson, C. Vannahme, C. L. C. Smith, K. T. Sørensen, and A. Kristensen, "Refractive index dispersion sensing using an array of photonic crystal resonant reflectors," *Appl. Phys. Lett.*, vol. 107, no. 6, p. 061101, 2015.
- [32] C. Ge, M. Lu, S. George, C. J. Wagner, J. Zheng, A. Pokhriyal, J. G. Eden, and B. T. Cunningham, "External cavity laser biosensor," *2012 IEEE Photonics Conf. IPC 2012*, vol. 13, no. 7, pp. 151–152, 2012.
- [33] M. Zhang, C. Ge, M. Lu, Z. Zhang, and B. T. Cunningham, "A self-referencing biosensor based upon a dual-mode external cavity laser," *Appl. Phys. Lett.*, vol. 102, no. 21, pp. 1–5, 2013.
- [34] P. Y. Li, B. Lin, J. Gerstenmaier, and B. T. Cunningham, "A new method for label-free imaging of biomolecular interactions," *Sensors Actuators, B Chem.*, vol. 99, no. 1, pp. 6–13, 2004.
- [35] B. Lin, P. Li, and B. T. Cunningham, "A label-free biosensor-based cell attachment assay for characterization of cell surface molecules," *Sensors Actuators, B Chem.*, vol. 114, no. 2, pp. 559–564, 2006.

- [36] E. a. Lidstone, V. Chaudhery, A. Kohl, V. Chan, T. Wolf-Jensen, L. B. Schook, R. Bashir, and B. T. Cunningham, "Label-free imaging of cell attachment with photonic crystal enhanced microscopy," *Analyst*, vol. 136, no. 18, pp. 3608–15, 2011.
- [37] W. Chen, K. D. Long, M. Lu, V. Chaudhery, H. Yu, J. S. Choi, J. Polans, Y. Zhuo, B. A. C. Harley, and B. T. Cunningham, "Photonic crystal enhanced microscopy for imaging of live cell adhesion," *Analyst*, vol. 138, no. 20, pp. 5886–94, 2013.
- [38] W. Chen, K. D. Long, H. Yu, Y. Tan, J. S. Choi, B. A. Harley, and B. T. Cunningham, "Enhanced live cell imaging via photonic crystal enhanced fluorescence microscopy," *Analyst*, vol. 139, no. 22, pp. 5954–63, 2014.
- [39] A. Ferrie, O. Deichmann, and F. Ye, "High resolution resonant waveguide grating imager for cell cluster analysis under physiological condition," *Appl. Phys. Lett.*, vol. 100, no. 22, p. 223701, 2012.
- [40] Y. Nazirizadeh, J. Reverey, U. Geyer, U. Lemmer, C. Selhuber-Unkel, and M. Gerken, "Material-based three-dimensional imaging with nanostructured surfaces," *Appl. Phys. Lett.*, vol. 102, no. 1, 2013.
- [41] P. C. Mathias, N. Ganesh, L. L. Chan, and B. T. Cunningham, "Combined enhanced fluorescence and label-free biomolecular detection with a photonic crystal surface," *Appl. Opt.*, vol. 46, no. 12, pp. 2351–60, 2007.
- [42] I. D. Block, P. C. Mathias, N. Ganesh, S. I. Jones, B. R. Dorvel, V. Chaudhery, L. O. Vodkin, R. Bashir, and B. T. Cunningham, "A detection instrument for enhanced-fluorescence and label-free imaging on photonic crystal surfaces," *Opt. Express*, vol. 17, no. 15, pp. 13222–13235, 2009.
- [43] N. Ganesh, I. D. Block, P. C. Mathias, W. Zhang, E. Chow, V. Malyarchuk, and B. T. Cunningham, "Leaky-mode assisted fluorescence extraction: application to fluorescence enhancement biosensors," *Opt. Express*, vol. 16, no. 26, pp. 21626–40, 2008.
- [44] B. Cunningham, J. Qiu, P. Li, and B. Lin, "Enhancing the surface sensitivity of colorimetric resonant optical biosensors," *Sensors Actuators B Chem.*, vol. 87, no. 2, pp. 365–370, 2002.
- [45] I. D. Block, L. L. Chan, and B. T. Cunningham, "Photonic crystal optical biosensor incorporating structured low-index porous dielectric," *Proc. IEEE Sensors*, vol. 2005, pp. 742–745, 2005.
- [46] W. Zhang, N. Ganesh, I. D. Block, and B. T. Cunningham, "High sensitivity photonic crystal biosensor incorporating nanorod structures for enhanced surface area," *Sensors Actuators B Chem.*, vol. 131, no. 1, pp. 279–284, 2008.

- [47] I. D. Block, P. C. Mathias, S. I. Jones, L. O. Vodkin, and B. T. Cunningham, "Optimizing the spatial resolution of photonic crystal label-free imaging.," *Appl. Opt.*, vol. 48, no. 34, pp. 6567–74, 2009.
- [48] B. Cunningham, M. Zhang, Y. Zhuo, L. Kwon, and C. Race, "Review of Recent Advances in Biosensing with Photonic Crystal Surfaces," *IEEE Sens. J.*, vol. 16, no. 10, pp. 3349–3366, 2015.
- [49] R. E. Kunz and J. Dubendorfer, "Miniature integrated-optical wavelength analyzer chip.," *Opt. Lett.*, vol. 20, no. 22, p. 2300, 1995.
- [50] D. J. Griffiths, *Introduction to Electrodynamics*. Prentice-Hall International Inc., NJ 07458, 3rd ed., 1999.
- [51] C. Kittel, *Introduction to Solid State Physics*. Wiley, New York, 1996.
- [52] M. Born and E. Wolf, *Principles of Optics*. Cambridge University Press, Cambridge, 7th ed., 1999.
- [53] R. W. Wood, "On a remarkable case of uneven distribution of light in a diffraction grating spectrum," *Philos. Mag. Ser. 6*, no. October 1902, pp. 37–41, 1902.
- [54] U. Fano, "Effects of configuration interaction on intensities and phase shifts," *Phys. Rev.*, vol. 124, no. 6, pp. 1866–1878, 1961.
- [55] R. Magnusson and S. S. Wang, "New principle for optical filters," *Appl. Phys. Lett.*, vol. 61, no. 9, p. 1022, 1992.
- [56] A. Ricciardi, S. Campopiano, A. Cusano, T. F. Krauss, and L. O'Faolain, "Broadband Mirrors in the Near-Infrared Based on Subwavelength Gratings in SOI," *IEEE Photonics J.*, vol. 2, no. 5, pp. 696–702, 2010.
- [57] J.-S. Ye, Y. Kanamori, F.-R. Hu, and K. Hane, "Self-supported subwavelength gratings with a broad band of high reflectance analysed by the rigorous coupled-wave method," *J. Mod. Opt.*, vol. 53, no. 14, pp. 1995–2004, 2006.
- [58] M. Shokooh-Saremi and R. Magnusson, "Wideband leaky-mode resonance reflectors: influence of grating profile and sublayers.," *Opt. Express*, vol. 16, no. 22, pp. 18249–63, 2008.
- [59] Y. Ding and R. Magnusson, "Resonant leaky-mode spectral-band engineering and device applications.," *Opt. Express*, vol. 12, no. 23, pp. 5661–74, 2004.
- [60] M. Mutlu, A. E. Akosman, G. Kurt, M. Gokkavas, and E. Ozbay, "Experimental realization of a high-contrast grating based broadband quarter-wave plate.," *Opt. Express*, vol. 20, no. 25, pp. 27966–73, 2012.

- [61] C. J. Chang-Hasnain and W. Yang, “High-contrast gratings for integrated optoelectronics,” *Adv. Opt. Photonics*, vol. 4, no. 3, p. 379, 2012.
- [62] Y. Ding and R. Magnusson, “Band gaps and leaky-wave effects in resonant photonic-crystal waveguides,” *Opt. Express*, vol. 15, no. 2, pp. 680–94, 2007.
- [63] P. Lalanne, J. P. Hugonin, and P. Chavel, “Optical properties of deep lamellar gratings: A coupled bloch-mode insight,” *J. Light. Technol.*, vol. 24, no. 6, pp. 2442–2449, 2006.
- [64] D. L. Brundrett, E. N. Glytsis, T. K. Gaylord, and J. M. Bendickson, “Effects of modulation strength in guided-mode resonant subwavelength gratings at normal incidence,” vol. 17, no. 7, pp. 1221–1230, 2000.
- [65] J. Joannopoulos, *Photonic Crystals: Molding the Flow of Light*. Princeton & Oxford: Princeton University Press, second ed., 2008.
- [66] Y. Ding and R. Magnusson, “Use of nondegenerate resonant leaky modes to fashion diverse optical spectra,” *Opt. Express*, vol. 12, no. 9, pp. 1885–91, 2004.
- [67] E. Yablonovitch, T. Gmitter, R. Meade, A. Rappe, K. Brommer, and J. Joannopoulos, “Donor and acceptor modes in photonic band structure,” *Phys. Rev. Lett.*, vol. 67, no. 24, pp. 3380–3383, 1991.
- [68] S. Zanotto, G. Biasiol, L. Sorba, and A. Tredicucci, “Photonic bands and defect modes in metallo-dielectric photonic crystal slabs,” *J. Opt. Soc. Am. B*, vol. 31, no. 7, p. 1451, 2014.
- [69] G. Voskerician, M. S. Shive, R. S. Shawgo, H. Von Recum, J. M. Anderson, M. J. Cima, and R. Langer, “Biocompatibility and biofouling of MEMS drug delivery devices,” *Biomaterials*, vol. 24, no. 11, pp. 1959–1967, 2003.
- [70] M. Elwenspoek and R. J. Wiegerink, *Mechanical Microsensors*. Springer Science & Business Media, 2001.
- [71] J. Olofsson, T. M. Grehk, T. Berling, C. Persson, S. Jacobson, and H. Engqvist, “Evaluation of silicon nitride as a wear resistant and resorbable alternative for total hip joint replacement,” *Biomater*, vol. 2, no. 2, pp. 94–102, 2012.
- [72] M. Mazzocchi and A. Bellosi, “On the possibility of silicon nitride as a ceramic for structural orthopaedic implants . Part I : processing , microstructure , mechanical properties , cytotoxicity,” *J. Mater. Sci. Mater. Med.*, vol. 19, pp. 2881–2887, 2008.
- [73] JEOL, “ASEM dish (Membrane dish),” http://www.jeol.co.jp/en/Appl.sm_b012.00-e.pdf. Accessed 2016-01-05.

- [74] H. R. Philipp, "Optical properties of silicon nitride," *J. Electrochem. Soc.*, vol. 120, no. 2, pp. 295–300, 1973.
- [75] Filmetrics, "Refractive index of Si₃N₄," <https://www.filmetrics.com/refractive-index-database/Si3N4/SiN-SiON-Silicon-Nitride>. Accessed: 2016-01-05.
- [76] M. G. Moharam and T. K. Gaylord, "Rigorous coupled-wave analysis of planar-grating diffraction," *J. Opt. Soc. Am.*, vol. 71, no. 7, pp. 811–818, 1981.
- [77] M. G. Moharam, E. B. Grann, D. A. Pommet, and T. K. Gaylord, "Formulation for stable and efficient implementation of the rigorous coupled-wave analysis of binary gratings," *J. Opt. Soc. Am. A*, vol. 12, no. 5, pp. 1068–1076, 1995.
- [78] M. G. Moharam, D. A. Pommet, E. B. Grann, and T. K. Gaylord, "Stable implementation of the rigorous coupled-wave analysis for surface-relief gratings: enhanced transmittance matrix approach," *J. Opt. Soc. Am. A*, vol. 12, no. 5, pp. 1077–1086, 1995.
- [79] K. R. Harper, "Theory, design, and fabrication of diffractive grating coupler for slab waveguide," *All Theses Diss. Pap. 101.*, p. 193, 2003.
- [80] J. Kennedy and R. Eberhart, "Particle swarm optimization," *Neural Networks, 1995. Proceedings., IEEE Int. Conf.*, vol. 4, pp. 1942–1948 vol.4, 1995.
- [81] M. Shokooh-Saremi and R. Magnusson, "Particle swarm optimization and its application to the design of diffraction grating filters," *Opt. Lett.*, vol. 32, no. 8, pp. 894–6, 2007.
- [82] ALLRESIST, "Positive E-Beam Resists AR-P 6200," <http://www.allresist.com/wp-content/uploads/sites/2/2014/12/allresist-produktinfos-ar-p6200-englisch.pdf>. Accessed: 2016-01-06.
- [83] M. J. Madou, *Fundamentals of Microfabrication and Nanotechnology (Volume II): Manufacturing techniques for microfabrication and nanotechnology*. CRC Press, 3 ed., 2011.
- [84] K. Williams and R. Muller, "Etch rates for micromachining processing," *J. Microelectromechanical Syst.*, vol. 5, no. 4, pp. 256–269, 1996.
- [85] W. V. Gelder and V. E. Hauser, "The Etching of Silicon Nitride in Phosphoric Acid with Silicon Dioxide as a Mask," *J. Electrochem. Soc.*, vol. 114, no. 8, pp. 869–872, 1967.
- [86] K. R. Williams, K. Gupta, and M. Wasilik, "Etch Rates for Micromachining Processing - Part II," *J. Microelectromechanical Syst.*, vol. 12, no. 6, pp. 761–778, 2003.

- [87] F. F. Chen, *Introduction to Plasma Physics and Controlled Fusion: Volume 1: Plasma Physics*. Springer, 2 ed., 1984.
- [88] R. Legtenberg, H. Jansen, M. de Boer, and M. Elwenspoek, “Anisotropic reactive ion etching of silicon using SF₆/O₂/CHF₃ gas mixtures,” *J. Electrochem. Soc.*, vol. 142, no. 6, pp. 2020–2028, 1995.
- [89] P. H. Lissberger and W. L. Wilcock, “Properties of All-Dielectric Interference Filters. II. Filters in Parallel Beams of Light Incident Obliquely and in Convergent Beams,” *J. Opt. Soc. Am.*, vol. 49, no. 2, pp. 126–130, 1959.
- [90] P. S. Dittrich and A. Manz, “Lab-on-a-chip: microfluidics in drug discovery,” *Nat. Rev. Drug Discov.*, vol. 5, no. 3, pp. 210–218, 2006.
- [91] C. Rivet, H. Lee, A. Hirsch, S. Hamilton, and H. Lu, “Microfluidics for medical diagnostics and biosensors,” *Chem. Eng. Sci.*, vol. 66, no. 7, pp. 1490–1507, 2011.
- [92] A. Bange, H. B. Halsall, and W. R. Heineman, “Microfluidic immunosensor systems,” *Biosens. Bioelectron.*, vol. 20, no. 12, pp. 2488–2503, 2005.
- [93] D. C. Duffy, J. C. McDonald, O. J. a. Schueller, and G. M. Whitesides, “Rapid prototyping of microfluidic systems in poly(dimethylsiloxane),” *Anal. Chem.*, vol. 70, no. 23, pp. 4974–4984, 1998.
- [94] P. Abgrall and A. Gué, “Lab-on-chip technologies: making a microfluidic network and coupling it into a complete microsystem—a review,” *J. Micromechanics Microengineering*, vol. 17, pp. R15–R49, 2007.
- [95] S. Bhattacharya, A. Datta, J. M. Berg, and S. Gangopadhyay, “Studies on surface wettability of poly(dimethyl) siloxane (PDMS) and glass under oxygen-plasma treatment and correlation with bond strength,” *J. Microelectromechanical Syst.*, vol. 14, no. 3, pp. 590–597, 2005.
- [96] K. Haubert, T. Drier, and D. Beebe, “PDMS bonding by means of a portable, low-cost corona system,” *Lab Chip*, vol. 6, no. 12, pp. 1548–9, 2006.
- [97] M. A. Eddings, M. A. Johnson, and B. K. Gale, “Determining the optimal PDMS–PDMS bonding technique for microfluidic devices,” *J. Micromechanics Microengineering*, vol. 18, no. 6, p. 067001, 2008.
- [98] S. Satyanarayana, R. N. Karnik, and A. Majumdar, “Stamp-and-stick room-temperature bonding technique for microdevices,” *J. Microelectromechanical Syst.*, vol. 14, no. 2, pp. 392–399, 2005.

- [99] S. Weiss, G. Rong, and J. Lawrie, "Current status and outlook for silicon-based optical biosensors," *Phys. E Low-dimensional Syst. Nanostructures*, vol. 41, no. 6, pp. 1071–1075, 2009.
- [100] J. Homola, J. Ctyroky, M. Skalky, J. Hradiliva, and P. Kolarova, "A surface plasmon resonance based integrated optical sensor," *Sensors Actuators B Chem.*, vol. 38-39, pp. 286–290, 1997.
- [101] W. M. Bin Mat Yunus and A. Bin Abdul Rahman, "Refractive index of solutions at high concentrations," *Appl. Opt.*, vol. 28, no. 13, p. 2465, 1989.
- [102] I. Block and N. Ganesh, "A sensitivity model for predicting photonic crystal biosensor performance," *Sensors J.*, vol. 8, no. 3, pp. 274–280, 2008.
- [103] I. D. Block, L. L. Chan, and B. T. Cunningham, "Photonic crystal optical biosensor incorporating structured low-index porous dielectric," *Proc. IEEE Sensors*, vol. 2005, no. March 2016, pp. 742–745, 2005.
- [104] S. Grego, K. H. Gilchrist, J. B. Carlson, and B. R. Stoner, "A compact and multi-channel optical biosensor based on a wavelength interrogated input grating coupler," *Sensors Actuators, B Chem.*, vol. 161, no. 1, pp. 721–727, 2012.
- [105] J. H. Schmid, W. Sinclair, J. García, S. Janz, J. Lapointe, D. Poitras, and Y. Li, "Silicon-on-insulator guided mode resonant grating for evanescent field molecular sensing," *Opt. Express*, vol. 17, no. 20, pp. 18371–18380, 2009.
- [106] S. Mandal and D. Erickson, "Nanoscale optofluidic sensor arrays," *Opt. Express*, vol. 16, no. 3, pp. 1623–1631, 2008.
- [107] A. Di Falco, L. O’Faolain, and T. F. Krauss, "Chemical sensing in slotted photonic crystal heterostructure cavities," *Appl. Phys. Lett.*, vol. 94, no. 6, pp. 1–4, 2009.
- [108] J. Jágerská, H. Zhang, Z. Diao, N. Le Thomas, and R. Houdré, "Refractive index sensing with an air-slot photonic crystal nanocavity," *Opt. Lett.*, vol. 35, no. 15, pp. 2523–2525, 2010.
- [109] K. De Vos, I. Bartolozzi, E. Schacht, P. Bienstman, and R. Baets, "Silicon-on-Insulator microring resonator for sensitive and label-free biosensing," *Opt. Express*, vol. 15, no. 12, pp. 7610–7615, 2007.
- [110] A. Yalçın, K. C. Popat, J. C. Aldridge, T. A. Desai, J. Hryniewicz, N. Chbouki, B. E. Little, O. King, V. Van, S. Chu, D. Gill, M. Anthes-Washburn, M. S. Ünlü, and B. B. Goldberg, "Optical sensing of biomolecules using microring resonators," *IEEE J. Sel. Top. Quantum Electron.*, vol. 12, no. 1, pp. 148–154, 2006.

- [111] T. Claes, J. G. Molera, K. De Vos, E. Schacht, R. Baets, and P. Bienstman, “Label-free biosensing with a slot-waveguide-based ring resonator in silicon on insulator,” *IEEE Photonics J.*, vol. 1, no. 3, pp. 197–204, 2009.
- [112] C. Carlborg, K. Gylfason, A. Kazmierczak, F. Dortu, M. Banuls Polo, A. Maquieira Catala, G. Kresbach, H. Sohlström, T. Moh, L. Vivien, J. Popplewell, G. Ronan, C. A. Barrios, G. Stemme, and W. van der Wijngaart, “A packaged optical slot-waveguide ring resonator sensor array for multiplex label-free assays in labs-on-chips,” *Lab Chip*, vol. 10, no. 3, pp. 281–290, 2010.
- [113] C. A. Barrios, K. B. Gylfason, B. Sánchez, A. Griol, H. Sohlström, M. Holgado, and R. Casquel, “Slot-waveguide biochemical sensor,” *Opt. Lett.*, vol. 32, no. 21, pp. 3080–3082, 2007.
- [114] M. Scullion, M. Fischer, and T. Krauss, “Fibre Coupled Photonic Crystal Cavity Arrays on Transparent Substrates for Spatially Resolved Sensing,” *Photonics*, vol. 1, no. 4, pp. 412–420, 2014.
- [115] J. Murray, D. Nowak, L. Pukenas, R. Azhar, M. Guillerit, C. Wälti, K. Critchley, S. Johnson, and R. S. Bon, “Solid phase synthesis of functionalised SAM-forming alkanethiol-oligoethyleneglycols,” *J. Mater. Chem. B*, vol. 2, no. 24, pp. 3741–3744, 2014.
- [116] D. Kim and A. E. Herr, “Protein immobilization techniques for microfluidic assays,” *Biomicrofluidics*, vol. 7, no. 4, pp. 1–47, 2013.
- [117] L. S. Wong, F. Khan, and J. Micklefield, “Selective covalent protein immobilization: Strategies and applications,” *Chem. Rev.*, vol. 109, no. 9, pp. 4025–4053, 2009.
- [118] Y. Jung, J. Y. Jeong, and B. H. Chung, “Recent advances in immobilization methods of antibodies on solid supports,” *Analyst*, vol. 133, no. 6, pp. 697–701, 2008.
- [119] ThermoFisher, “NHS & Sulfo-NHS,” https://tools.thermofisher.com/content/sfs/manuals/MAN0011309_NHS_SulfoNHS_UG.pdf. Accessed: 2016-04-29.
- [120] S. K. Vashist, “Comparison of 1-Ethyl-3-(3-Dimethylaminopropyl) Carbodiimide Based Strategies to Crosslink Antibodies on Amine-Functionalized Platforms for Immunodiagnostic Applications,” *Diagnostics*, vol. 2, no. 3, pp. 23–33, 2012.
- [121] Y. Chen and Y. Zhang, “Fluorescent quantification of amino groups on silica nanoparticle surfaces,” *Anal. Bioanal. Chem.*, vol. 399, no. 7, pp. 2503–2509, 2011.
- [122] N. R. Glass, R. Tjeung, P. Chan, L. Y. Yeo, and J. R. Friend, “Organosilane deposition for microfluidic applications,” *Biomicrofluidics*, vol. 5, no. 3, pp. 1–7, 2011.

- [123] G. Vidarsson, G. Dekkers, and T. Rispens, "IgG subclasses and allotypes: From structure to effector functions," *Front. Immunol.*, vol. 5, no. 520, pp. 1–17, 2014.
- [124] R. Jefferis and D. S. Kumararatne, "Selective IgG subclass deficiency: quantification and clinical relevance.," *Clin. Exp. Immunol.*, vol. 81, no. 3, pp. 357–67, 1990.
- [125] T. W. Kuijpers, R. S. Weening, and T. A. Out, "IgG subclass deficiencies and recurrent pyogenic infections, unresponsiveness against bacterial polysaccharide antigen," *Allergol. Immunopathol. (Madr).*, vol. 20, no. 1, pp. 28–34, 1991.
- [126] A. Brecht and G. Gauglitz, "Optical probes and transducers.," *Biosens. Bioelectron.*, vol. 10, no. 9, pp. 923–36, 1995.
- [127] SCHOTT North America Inc., "SCHOTT Optical Glass: Data Sheets," <http://refractiveindex.info/download/data/2015/schott-optical-glass-collection-datasheets-july-2015-us.pdf>. Accessed: 2016-01-20.
- [128] M. N. Polyanskiy, "Refractive index database: Optical constants of SCHOTT - BK (Borosilicate crown)," <http://refractiveindex.info/?shelf=glass&book= SCHOTT-BK&page=N-BK7>. Accessed: 2016-01-20.
- [129] G. J. Triggs, M. Fischer, D. Stellinga, M. G. Scullion, G. J. O. Evans, and T. F. Krauss, "Spatial Resolution and Refractive Index Contrast of Resonant Photonic Crystal Surfaces for Biosensing," *IEEE Photonics J.*, vol. 7, no. 3, pp. 1–10, 2015.
- [130] N. Lue, G. Popescu, T. Ikeda, R. R. Dasari, K. Badizadegan, and M. S. Feld, "Live cell refractometry using microfluidic devices," *Opt. Lett.*, vol. 31, no. 18, pp. 2759–2761, 2006.
- [131] "Refractive index of sucrose solutions," <http://www.refractometer.pl/Refract>. Accessed 2016-03-04.
- [132] "Density and refractive indexes of sucrose," <http://homepages.gac.edu/~cellab/chpts/chpt3/table3-2.html>. Accessed: 2016-03-03.
- [133] C.-C. Yang and W.-C. Chen, "The structures and properties of hydrogen silsesquioxane (HSQ) films produced by thermal curing," *J. Mater. Chem.*, vol. 12, no. 4, pp. 1138–1141, 2002.
- [134] S. Choi, M. J. Word, V. Kumar, and I. Adesida, "Comparative study of thermally cured and electron-beam-exposed hydrogen silsesquioxane resists," *J. Vac. Sci. Technol. B Microelectron. Nanom. Struct.*, vol. 26, no. 5, p. 1654, 2008.
- [135] A. F. Oskooi, D. Roundy, M. Ibanescu, P. Bermel, J. D. Joannopoulos, and S. G. Johnson, "Meep : A flexible free-software package for electromagnetic simulations by the FDTD method," *Comput. Phys. Commun.*, vol. 181, no. 3, pp. 687–702, 2010.

- [136] Y. Zhuo, H. Hu, W. Chen, M. Lu, L. Tian, H. Yu, K. D. Long, E. Chow, W. P. King, S. Singamaneni, and B. T. Cunningham, "Single nanoparticle detection using photonic crystal enhanced microscopy," *Analyst*, vol. 139, pp. 1007–15, 2014.
- [137] D. Batista, A. P. Carvalho, R. Costa, R. Coutinho, S. Dobretsov, W. Verstraete, M. Burmølle, J. S. Webb, D. Rao, L. H. Hansen, S. J. Sørensen, S. Kjelleberg, R. M. Donlan, S. Huang, M. G. Hadfield, J. D. Parry, W. Verstraete, and E. B. Sherr, "The technological side of the microbiome," *npj Biofilms Microbiomes*, vol. 57, no. 6, pp. 10–13, 2002.
- [138] J. W. Costerton, G. G. Geesey, and K. J. Cheng, "How bacteria stick.," *Sci. Am.*, vol. 238, no. 1, pp. 86–95, 1978.
- [139] R. M. Donlan, "Biofilms: Microbial life on surfaces," *Emerg. Infect. Dis.*, vol. 8, no. 9, pp. 881–890, 2002.
- [140] H. C. Flemming, "Biofouling in water systems - Cases, causes and countermeasures," *Appl. Microbiol. Biotechnol.*, vol. 59, no. 6, pp. 629–640, 2002.
- [141] US National Institute of Health (NIH), "US National Institute of Health: Research on Microbial Biofilms," [https://grants.nih.gov/grants/ Guid](https://grants.nih.gov/grants/Guid). Accessed 2016-04-29.
- [142] R. M. Donlan, "Biofilms and device-associated infections," *Emerg Infect Dis*, vol. 7, no. 2, pp. 277–281, 2001.
- [143] P. S. Stewart and J. William Costerton, "Antibiotic resistance of bacteria in biofilms," *Lancet*, vol. 358, no. 9276, pp. 135–138, 2001.
- [144] N. Høiby, T. Bjarnsholt, M. Givskov, S. Molin, and O. Ciofu, "Antibiotic resistance of bacterial biofilms," *Int. J. Antimicrob. Agents*, vol. 35, no. 4, pp. 322–332, 2010.
- [145] T. J. Marrie, J. Nelligan, and J. W. Costerton, "A scanning and transmission electron microscopic study of an infected endocardial pacemaker lead," *Circulation*, vol. 66, no. 6, pp. 1339–1341, 1982.
- [146] R. D. Scott, *The direct medical costs of healthcare-associated infections in US hospitals and the benefits of prevention*. Division of Healthcare Quality Promotion National Center for Preparedness, Detection, and Control of Infectious Diseases, Centers for Disease Control and Prevention, 2009.
- [147] E. Denkhaus, S. Meisen, U. Telgheder, and J. Wingender, "Chemical and physical methods for characterisation of biofilms," *Microchim. Acta*, vol. 158, no. 1-2, pp. 1–27, 2007.

- [148] Sigma-Aldrich Co., “4,6-Diamidino-2-phenylindole dihydrochloride - PRODUCT INFORMATION SHEET,” <http://www.sigmaaldrich.com/etc/medialib/docs/Sigma/Prod.d8417pis.Par.0001.File.tmp/d8417pis.pdf>. Accessed 2016-04-01.
- [149] M. Fischer, M. Wahl, and G. Friedrichs, “Design and field application of a UV-LED based optical fiber biofilm sensor,” *Biosens. Bioelectron.*, vol. 33, no. 1, pp. 172–178, 2012.
- [150] Sigma and Cook, “The Cell Environment (including types of culture medium),” in *Fundam. Tech. Cell Cult. Lab. Handb.*, vol. 12, 2nd ed., 2010.
- [151] A. Curtis and C. Wilkinson, “Topographical control of cells,” *Biomaterials*, vol. 18, no. 24, pp. 1573–1583, 1997.
- [152] M. M. Stevens and J. H. George, “Exploring and engineering the cell surface interface,” *Science*, vol. 310, no. November, pp. 1135–1138, 2005.
- [153] B. Lin, P. Li, and B. T. Cunningham, “A label-free biosensor-based cell attachment assay for characterization of cell surface molecules,” *Sensors Actuators B Chem.*, vol. 114, no. 2, pp. 559–564, 2006.
- [154] J. E. Park and A. Barbul, “Understanding the role of immune regulation in wound healing,” *Am. J. Surg.*, vol. 187, no. 5 SUPPL. 1, pp. 2–7, 2004.
- [155] G. J. O. Evans, “Synaptic signalling in cerebellar plasticity,” *Biol. Cell*, vol. 99, no. 7, pp. 363–78, 2007.
- [156] G. Köhler and C. Milstein, “Continuous cultures of fused cells secreting antibody of predefined specificity,” *Nature*, vol. 256, pp. 495–497, 1975.
- [157] C. Zhang, *Antibody Methods and Protocols*, ch. Hybridoma, pp. 117–135. Totowa, NJ: Humana Press, 2012.
- [158] M. T. Madigan, J. M. Martinko, and J. Parker, *Brock Biology of Microorganisms*. Prentice-Hall, Inc., ninth ed., 2000.
- [159] P. F. Lawton, C. Saunter, and J. Girkin, “Combining optical trapping in a microfluidic channel with simultaneous micro-Raman spectroscopy and motion detection,” in *SPIE MOEMS-MEMS*, International Society for Optics and Photonics, 2014.
- [160] Y.-J. Rao, “In-fibre Bragg grating sensors,” *Meas. Sci. Technol.*, vol. 8, no. 4, p. 355, 1997.
- [161] K. Bremer and B. Roth, “Fibre optic surface plasmon resonance sensor system designed for smartphones,” *Opt. Express*, vol. 23, no. 13, pp. 17179–84, 2015.

- [162] D. Gallegos, K. D. Long, H. Yu, P. P. Clark, Y. Lin, S. George, P. Nath, and B. T. Cunningham, "Label-free biodetection using a smartphone.," *Lab Chip*, vol. 13, no. 11, pp. 2124–32, 2013.
- [163] P. Preechaburana, M. C. Gonzalez, A. Suska, and D. Filippini, "Surface plasmon resonance chemical sensing on cell phones," *Angew. Chemie - Int. Ed.*, vol. 51, no. 46, pp. 11585–11588, 2012.
- [164] K. D. Long, H. Yu, and B. T. Cunningham, "Smartphone instrument for portable enzyme-linked immunosorbent assays.," *Biomed. Opt. Express*, vol. 5, no. 11, pp. 3792–3806, 2014.
- [165] A. E. Cetin, A. F. Coskun, B. C. Galarreta, M. Huang, D. Herman, A. Ozcan, and H. Altug, "Handheld high-throughput plasmonic biosensor using computational on-chip imaging," *Light Sci. Appl.*, vol. 3, no. 1, p. e122, 2014.
- [166] S. Jahns, M. Bräu, B.-O. Meyer, T. Karrock, S. B. Gutekunst, L. Blohm, C. Selhuber-Unkel, R. Buhmann, Y. Nazirizadeh, and M. Gerken, "Handheld imaging photonic crystal biosensor for multiplexed, label-free protein detection," *Biomed. Opt. Express*, vol. 6, no. 10, p. 3724, 2015.
- [167] R. E. Kunz, J. Edlinger, P. Sixt, and M. T. Gale, "Replicated chirped waveguide gratings for optical sensing application.," *Sensors Actuators A Phys.*, vol. 47, pp. 482–486, 1995.
- [168] A. W. Martinez, S. T. Phillips, G. M. Whitesides, and E. Carrilho, "Diagnostics for the developing world: microfluidic paper-based analytical devices.," *Anal. Chem.*, vol. 82, no. 1, pp. 3–10, 2010.
- [169] A. K. Yetisen, M. S. Akram, and C. R. Lowe, "Paper-based microfluidic point-of-care diagnostic devices.," *Lab Chip*, vol. 13, no. 12, pp. 2210–51, 2013.
- [170] A. P. Alivisatos, A. M. Andrews, E. S. Boyden, M. Chun, G. M. Church, K. Deisseroth, J. P. Donoghue, S. E. Fraser, J. Lippincott-Schwartz, L. L. Looger, S. Maniatis, P. L. McEuen, A. V. Nurmikko, H. Park, D. S. Peterka, C. Reid, M. L. Roukes, A. Scherer, M. Schnitzer, T. J. Sejnowski, K. L. Shepard, D. Tsao, G. Turrigiano, P. S. Weiss, C. Xu, R. Yuste, and X. Zhuang, "Nanotools for neuroscience and brain activity mapping.," *ACS Nano*, vol. 7, no. 3, pp. 1850–66, 2013.
- [171] A. Mizutani, H. Kikuta, and K. Iwata, "Wave localization of double periodic guided-mode resonant grating filters," *Opt. Rev.*, vol. 10, no. 1, pp. 13–18, 2003.